Cosmological Constraints from Measurements of Type Ia Supernovae Discovered during the First 1.5 yr of the Pan-STARRS1 Survey

Citation

Published Version

Permanent link

Terms of Use

Share Your Story

arXiv:1310.3828v2 [astro-ph.CO] 31 Aug 2014

COSMOLOGICAL CONSTRAINTS FROM MEASUREMENTS OF TYPE IA SUPERNOVAE DISCOVERED DURING THE FIRST 1.5 YEARS OF THE PAN-STARRS1 SURVEY

A. Rest[1], D. Scolnic[2], R. J. Foley[3,4,5], M. E. Huber[6], R. Chornock[3], G. Narayan[7], J. L. Tonry[6], E. Berger[3],
A. M. Soderberg[3], C. W. Stubbs[7,3], A. Riess[2], R. P. Kirshner[3,7], S. J. Smartt[8], E. Schlafly[9], S. Rodney[2,10],
M. T. Botticella[11], D. Brout[2], P. Challis[3], I. Czekala[3], M. Drout[3], M. J. Hudson[12,13], R. Kotak[8], C. Leibler[14],
R. Lunnan[3], G. H. Marion[3], M. McCrum[8], D. Milisavljevic[3], A. Pastorello[15], N. E. Sanders[3], K. Smith[8],
E. Stafford[2], D. Thilker[2], S. Valenti[16,17], W. M. Wood-Vasey[18], Z. Zheng[2], W. S. Burgett[6], K. C. Chambers[6],
L. Denneau[6], P. W. Draper[19], H. Flewelling[6], K. W. Hodapp[6], N. Kaiser[6], R.-P. Kudritzki[6], E. A. Magnier[6],
N. Metcalfe[19], P. A. Price[20], W. Sweeney[6], R. Wainscoat[6], C. Waters[6].

September 2, 2014

ABSTRACT

We present $griz_{P1}$ light curves of 146 spectroscopically confirmed Type Ia Supernovae ($0.03 < z < 0.65$) discovered during the first 1.5 years of the Pan-STARRS1 Medium Deep Survey. The Pan-STARRS1 natural photometric system is determined by a combination of on-site measurements of the instrument response function and observations of spectrophotometric standard stars. We find that the systematic uncertainties in the photometric system are currently 1.2% without accounting for the uncertainty in the *HST* Calspec definition of the AB system. A Hubble diagram is constructed with a subset of 113 out of 146 SNe Ia that pass our light curve quality cuts. The cosmological fit to 310 SNe Ia (113 PS1 SNe Ia + 222 light curves from 197 low-z SNe Ia), using only SNe and assuming a constant dark energy equation of state and flatness, yields $w = -1.120^{+0.360}_{-0.206}(\text{Stat})^{+0.269}_{-0.291}(\text{Sys})$. When combined with BAO+CMB(*Planck*)+H_0, the analysis yields $\Omega_M = 0.280^{+0.013}_{-0.012}$ and $w = -1.166^{+0.072}_{-0.069}$ including all identified systematics (Scolnic et al. 2013). The value of w is inconsistent with the cosmological constant value of -1 at the 2.3σ level. Tension endures after removing either the BAO or the H_0 constraint, though it is strongest when including the H_0 constraint. If we include *WMAP9* CMB constraints instead of those from *Planck*, we find $w = -1.124^{+0.083}_{-0.065}$, which diminishes the discord to $< 2\sigma$. We cannot conclude whether the tension with flat ΛCDM is a feature of dark energy, new physics, or a combination of chance and systematic errors. The full Pan-STARRS1 supernova sample with ~3 times as many SNe should provide more conclusive results.

Subject headings: supernova:general—cosmology:observations—cosmological parameters—dark energy

[1] Space Telescope Science Institute, 3700 San Martin Drive, Baltimore, MD 21218, USA

[2] Department of Physics and Astronomy, Johns Hopkins University, 3400 North Charles Street, Baltimore, MD 21218, USA

[3] Harvard-Smithsonian Center for Astrophysics, 60 Garden Street, Cambridge, MA 02138, USA

[4] Astronomy Department, University of Illinois at Urbana-Champaign, 1002 West Green Street, Urbana, IL 61801, USA

[5] Department of Physics, University of Illinois Urbana-Champaign, 1110 W. Green Street, Urbana, IL 61801, USA

[6] Institute for Astronomy, University of Hawaii, 2680 Woodlawn Drive, Honolulu, HI 96822, USA

[7] Department of Physics, Harvard University, 17 Oxford Street, Cambridge MA 02138

[8] Astrophysics Research Centre, School of Mathematics and Physics, Queens University Belfast, Belfast, BT71NN, UK

[9] Max Planck Institute for Astronomy, K onigstuhl 17, D-69117 Heidelberg, Germany

[10] Hubble Postdoctoral Fellow

[11] INAF - Osservatorio Astronomico di Capodimonte, Salita Moiariello 16, 80131 Napoli, Italy

[12] University of Waterloo, 200 University Ave W Waterloo, ON N2L 3G1, Canada

[13] Perimeter Institute for Theoretical Physics, 31 Caroline St N, Waterloo, Ontario, N2L 2Y5, Canada

[14] Department of Astronomy & Astrophysics, University of California, Santa Cruz, CA 95060, USA

[20] Department of Astrophysical Sciences, Princeton University, Princeton, NJ 08544, USA

[15] INAF - Osservatorio Astronomico di Padova, Vicolo dell'Osservatorio 5, 35122 Padova, Italy

[16] Las Cumbres Observatory Global Telescope Network, Inc., Santa Barbara, CA 93117, USA

[17] Department of Physics, University of California Santa Barbara, Santa Barbara, CA 93106-9530, USA

[18] PITT PACC, Department of Physics and Astronomy, University of Pittsburgh, Pittsburgh, PA 15260, USA.

[19] Department of Physics, University of Durham Science Laboratories, South Road Durham DH1 3LE, UK

1. INTRODUCTION

We have used the Medium Deep Field (MDF) survey of the Pan-STARRS1 Science program as the source for detecting thousands of transient events. These include supernovae (SN) and other transients of unusual types (Gezari et al. 2010; Botticella et al. 2010; Chomiuk et al. 2011; Narayan et al. 2011; Lee et al. 2012; Gezari et al. 2012; Sanders et al. 2012; Berger et al. 2012; Lunnan et al. 2013; Chornock et al. 2013; Sanders et al. 2013; Berger et al. 2013). In parallel, we are also exploiting the Pan-STARRS1 3π survey for detection of brighter transients at lower redshifts (Pastorello et al. 2010; Valenti et al. 2012; Inserra et al. 2013). Here, we describe 146 Type Ia supernovae (SNe Ia) from the first year and a half of observations that we use to measure the history of cosmic expansion to help constrain the properties of dark energy. This report explains our observing strategy, photometric reductions, and cosmological analysis. The systematic errors in the photometry are discussed at length in this paper, while the companion paper by Scolnic et al. (2013) (hereafter S14) focuses on the systematic uncertainties in the cosmological analysis.

SN Ia have been proven to be reliable standard candles at cosmological distances. The Supernova Cosmology Project and the High-Z Supernova Team discovered SNe Ia at redshifts from 0.3 to 1 that provided the first evidence for cosmic acceleration (Riess et al. 1998; Perlmutter et al. 1999). This result in combination with measurements of the baryon acoustic peak in the large-scale correlation function of galaxies (e.g., Blake et al. 2011; Anderson et al. 2012) and the power spectrum of fluctuations in the cosmic microwave background (CMB) (e.g., Hinshaw et al. 2013; Planck Collaboration et al. 2013) indicates that we live in a flat, accelerating Universe composed of baryons, dark matter, and dark energy.

SN Ia are more-or-less homogeneous thermonuclear explosions of white dwarfs. The discovery by Phillips (1993) that the shape of the supernova light curve is related to the SN Ia luminosity, opened the door for their use as precise cosmic standard candles. In 1996, the Calán/Tololo group published light curves of 29 SN in 4 colors (Hamuy et al. 1996a). This data set was large enough to develop reliable ways to use the SN light curves to determine the intrinsic luminosity of SN Ia and to measure the luminosity distance with an precision of ~10% to each object (e.g., Δm_{15}, Hamuy et al. 1996c,b; Phillips et al. 1999, and MLCS, Riess et al. 1996). Since then, new approaches and new algorithms have improved light-curve fitting so that well-observed SN Ia have individual luminosity distances good to 5% (e.g., MLCS2K2, Jha et al. 2007; Stretch, Goldhaber et al. 2001; SALT, Guy et al. 2007; SiFTO, Conley et al. (2008); and BayeSN, Mandel et al. 2009, 2011).

With more accurate methods to determine distances of SN Ia, it is now possible to probe the nature of dark energy by constraining its equation of state, characterized by the parameter $w = P/(\rho c^2)$, where P is its pressure and ρ is its density. Evidence for cosmic acceleration and constraints on the dark energy are derived from the combination of low redshift samples and high redshift samples. In the last decade, many groups have worked on assembling large sets of low-redshift SNe (e.g., CfA1-CfA4, Riess et al. (1999); Jha et al. (2006); Hicken et al. (2009a,b, 2012); CSP, Contreras et al. (2010); Folatelli et al. (2010); Stritzinger et al. (2011); LOSS, Ganeshalingam et al. (2013)). In total, the currently published low-z SN sample comprises more than 500 SNe Ia. There have been three main surveys probing the higher redshift range, ESSENCE (Miknaitis et al. 2007; Wood-Vasey et al. 2007), SNLS (Conley et al. 2011; Sullivan et al. 2011), and SDSS (Frieman et al. 2008; Kessler et al. 2009a). These surveys have overlapping redshift ranges from $0.1 \lesssim z \lesssim 0.4$ for SDSS, $0.2 \lesssim z \lesssim 0.7$ for ESSENCE, and $0.3 \lesssim z \lesssim 1.1$ for SNLS. For a more complete review of SN Ia cosmology from these surveys, see Kirshner (2010).

Increasing the number of SN alone will not improve the limits on w unless we decrease the systematic errors as well. The photometric calibration is currently the most significant source of systematic bias (Sullivan et al. 2011), since different sets of SN with light curves from different telescope/detector systems are compared to each other. There are significant efforts underway to improve and homogenize the photometric calibration of previous (e.g., SNLS and SDSS, Betoule et al. 2012) and on-going wide-field transient surveys like PS1 (Kaiser et al. 2010), PTF (Rau et al. 2009), and the Dark Energy Survey (DES, Flaugher et al. 2012). Another technical issue is how the light curve fitters deal with the degeneracy between intrinsic luminosity, extinction, and intrinsic color. For example, Scolnic et al. (2014) show that the distance residuals can be decreased by assuming an intrinsic SN Ia color dispersion as a prior, which also is consistent with a Milky Way-like reddening law.

In the future, the full Pan-STARRS1 SN sample will be uniquely suited to better constrain the nature of dark energy by covering a very wide redshift range $(0.03 < z < 0.65)$ with a single instrument. Although the Pan-STARRS1 sample presented in this paper does not have enough low-redshift SN Ia for a stand-alone cosmological analysis, it is sufficient for us to investigate the best approach to combining data from separate photometric systems. In this paper, we use the 146 SN Ia from the first 1.5 years (2009 September to 2011 May) of Pan-STARRS1 to constrain the cosmological parameters along with a joint constraint by other cosmological probes. We emphasize the reduction of systematic uncertainties that affect the measurement of dark energy properties. The number of SN Ia that pass all light-curve quality cuts (113) is almost half of the largest published individual high-redshift sample (248, Conley et al. (2011); Sullivan et al. (2011)). Our sample allows us to identify where we have the largest systematic errors and to develop remedies for them. Future analysis of the full data set will build on our current analysis, and improve today's largest systematic uncertainties: the photometric calibration, and flaws in light-curve fitting techniques.

This paper is organized as follows. In §2, we introduce the technical aspects of the Pan-STARRS1 system. We describe the transient alert system and the spectroscopic follow-up in §3 and §4, respectively. The SN Ia light curves are presented in §5, and the photometric calibration is presented in §6. We discuss how we determine distances from the SN Ia light curves in §7. In §8, we determine the cosmological parameters by combining our sample of 113 high-quality SN Ia with the low-redshift sample and constraints from other cosmological probes.

2. Pan-STARRS1 SURVEY

The Pan-STARRS1 system is a high-etendue wide-field imaging system, designed for dedicated survey observations. The system is installed on the peak of Haleakala on the island of Maui in the Hawaiian island chain. We provide below a terse summary of the Pan-STARRS1 survey instrumentation. A more complete description of the Pan-STARRS1 system, both hardware and software, is provided by Kaiser et al. (2010).

The Pan-STARRS1 optical design (Hodapp et al. 2004) uses a 1.8 meter diameter $f/4.4$ primary mirror, and a 0.9 m secondary. The telescope delivers images with low distortion over a field diameter of 3.3 degrees. An individual CCD cell has 800x800 pixels, with 10 μm pixels that subtend 0.258 arcsec. 64 of these CCD cells are grouped into an 8x8 array. The focal plane consists of 60 of these independent arrays, for a total of 1.4 Gigapixel. The detectors are back-illuminated CCDs manufactured by Lincoln Laboratory, which are read out using a Star-Grasp CCD controller in 7 seconds for a full unbinned image. Initial performance assessments are presented in Onaka et al. (2008).

The Pan-STARRS1 observations are obtained through a set of 5 broadband filters, which we have designated as g_{P1}, r_{P1}, i_{P1}, z_{P1}, and y_{P1} ($grizy_{P1}$). These filters are similar to the ones used in SDSS, with the most significant difference in the g band. We use the instrumental response functions determined by Tonry et al. (2012b).

In addition to covering the entire sky at $\delta > -30$ deg in 5 bands (3π survey), the Pan-STARRS1 survey has obtained deeper, higher cadence images in the $grizy_{P1}$ bands of the MDF fields listed in Table 1. In this paper, we exclusively use SN Ia detected in the MDFs.

Table 1
Pan-STARRS1 MDFs

Field	RA J2000	Dec J2000	N_{SN}	FWHM in arcsec			
				g_{P1}	r_{P1}	i_{P1}	z_{P1}
MD01	035.875	−04.250	15	1.25	1.15	1.05	1.03
MD02	053.100	−27.800	16	1.31	1.20	1.11	1.06
MD03	130.592	+44.317	20	1.18	1.09	1.06	1.03
MD04	150.000	+02.200	22	1.17	1.09	1.07	1.03
MD05	161.917	+58.083	13	1.24	1.17	1.06	0.99
MD06	185.000	+47.117	15	1.25	1.18	1.14	1.05
MD07	213.704	+53.083	15	1.23	1.13	1.14	1.08
MD08	242.787	+54.950	24	1.27	1.14	1.07	1.09
MD09	334.188	+00.283	9	1.26	1.15	1.02	1.02
MD10	352.312	−00.433	7	1.26	1.18	1.01	1.03

The MD field exposure times in the 5 filters are listed in Table 2. Observations of 3-5 MD fields are taken each night and the filters are cycled through in the pattern: g_{P1} and r_{P1} in the same night (dark time), followed by i_{P1} and z_{P1} on the subsequent second and third night, respectively. Around full moon only y_{P1} data are taken. Any one epoch consists of 8 dithered exposures of 8×113 seconds for g_{P1} and r_{P1} or 8×240 seconds for the other three, giving nightly stacked images of 904 and 1920 seconds duration. For the current analysis, we do not use the y_{P1} band. However in the future, the y_{P1} band data may prove useful for cosmological analysis of SN Ia because measurements in this band are less affected by dust in the near infrared. Due to weather and the occasional

technical downtime, the effective cadence varies significantly from season to season. On average, our cadence is 6 detections in 10 days, with a 5 day gap during bright time when the MDFs are exclusively observed in y_{P1}.

Table 2
MDF cadence

Night	Filter	Exposure Time (seconds)	5σ Depth (AB mag)
1	g_{P1}, r_{P1}	8×113 each	23.1, 23.3
2	i_{P1}	8×240	23.2
3	z_{P1}	8×240	22.8
repeats FM$\pm$3	y_{P1}	8×240	21.9

3. TRANSIENT ALERT SYSTEM

The depth of the MDF survey is ideal for detecting SN Ia up to a redshift of $z \approx 0.7$, and the cadence provides well-sampled, multi-band light curves. In this section, we describe how the MDF data are reduced and the objects of interest are identified.

The Pan-STARRS1 IPP system (Magnier 2006) performs flat-fielding on each individual image, using white-light flat-field images of a dome screen, in combination with an illumination correction obtained by rastering sources across the field of view. After determining an initial astrometric solution (Magnier et al. 2008), the flat-fielded images were then warped onto the tangent plane of the sky, using a flux conserving algorithm.

For the MDFs, there are several (typically eight) dithered images per filter in a given night. This allows for the removal of defects like cosmic rays and satellite streaks before they are combined into a nightly stacked image using a variance-weighted scheme. The nightly MDF stacked images are processed through a frame-subtraction analysis using the *photpipe* pipeline that members of our team developed for the SuperMACHO and ESSENCE surveys (Rest et al. 2005; Garg et al. 2007; Miknaitis et al. 2007). This robust and well-tested system determines the appropriate spatially varying convolution kernel[21] needed to match an image with a template image, and then performs a subtraction of the two images. We then detect significant flux excursions in the difference images using a modified version of *DoPHOT* (Schechter et al. 1993).

The SNe Ia discussed in this work were discovered during the first ∼1.5 yr of the survey. At the beginning of the survey, we had not yet obtained sufficient observations to construct deep template images for the SN search. Instead, we typically obtained two epochs of observations in each filter with double the usual exposure time to use as templates. We subtracted these templates from later observations to search for transient objects. The use of two templates reduced false detections from imperfections in a single template. After this initial period, we generated deep reference images from a subset of images with good image quality and low sky background. These deep reference images were subsequently used as templates for the SN search. The template images used for the search with *photpipe* are different from the deeper ones used for

---

[21] http://www.astro.washington.edu/users/becker/hotpants.html

the final light curves created by *transphot*, as discussed in Section 5.1.

Once photometry is performed on the difference images, we apply a set of conditions before flagging an excursion in flux at a given position as a potential transient source. Typical conditions are:

- Positive detections with a signal-to-noise ratio, SNR, ≥ 4 in at least 3 $griz_{P1}$ images within a time window of 10 days.

- Detections in subtractions using at least two distinct templates.

- No previous alert at that position.

The SNR cut significantly reduces the number of false positives and artifacts. Similarly, requiring detections in subtractions versus two templates reduces spurious detections related to artifacts in a particular template. Our requirement of no previous alert at a particular position prevents variable sources from being continually flagged. The parameters related to the search were adjusted several times throughout the survey. There was a constant evolution of the parameters to optimize source detection as we gained experience with the data. But there were also cases where we would modify the parameters at a given time for testing purposes or for immediate goals such as increasing the number of young detected objects just prior to a spectroscopic follow-up observing run.

An important aspect of our reduction scheme is to perform PSF fitting photometry on all difference images at the location of any transient candidate, which we call "forced photometry." This is particularly helpful for discriminating between SN and AGN, since many AGN show low-level, long timescale variability in previous epochs that may not be above the detection limit in a single image, but clearly detectable over many epochs. It also can provide additional data when a SN is faint (particularly when it is rising) or if the image quality is poor (for instance when there are clouds).

Each transient candidate that passes our stated conditions is sorted into one of five categories: transient, possible transient, variable, asteroid, and artifact. Transients are identified as sources with no variability in previous epochs, a "smooth" light curve, and either previous "in-season" non-detections or a clear offset from a host galaxy. Both because of possible confusion with AGN and subtraction artifacts, transients that are visually offset from a galaxy nucleus are easier to identify than those that are coincident with a nucleus. In cases where the identification is ambiguous either due to low SNR or possible variability in previous epochs, the object is classified as a possible transient.

We attempt to err on the side of inclusion to maximize the number of transients discovered. We refrain from classifying objects as "non-transient" until there is significant evidence that they are not transients (such as past variability, clear indication of the source being an artifact, or spectroscopy from an exterior catalog). We re-evaluate and possibly re-classify each candidate object as we acquire more points on its light curve.

As shown by the upper panel of Figure 1, we discovered almost all of our spectroscopically confirmed SNe Ia at phases between -12 and $+4$ days.
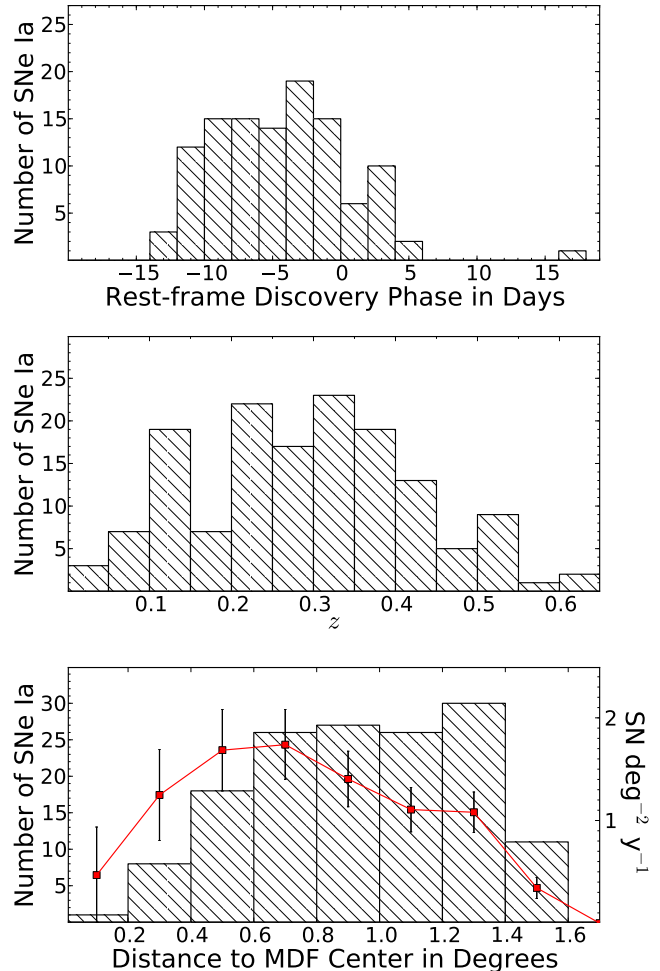

Figure 1. PS1 MDF survey characteristics for all spectroscopically confirmed PS1 SN Ia. *Upper panel:* Histogram of the number of SN Ia with respect to the phase of discovery in the rest-frame. *Middle panel:* Histogram of the redshift distribution. *Lower panel:* Histogram of SN Ia as a function of distance to the MDF center. The observed SN rate per constant area is shown with the red symbols and line. The rate is constant within the uncertainties to a distance of ~ 1.3 degrees from center.

A parallel, independent search for transients is done at Queen's University Belfast based on difference images which are generated in Hawaii through the IPP system and this is described in McCrum et al. (2013). The correlation between the discoveries in *photpipe* and the IPP based "Transient Science Server" is excellent, with virtually all high significance transients detected in both systems. Some of the SN in this sample were originally selected for spectroscopic classification from the IPP-based catalogs, but all were also detected through *photpipe* and all the photometry discussed in this paper is exclusively from the *photpipe* system.

4. SPECTROSCOPIC PRIORITIZATION & FOLLOW-UP SPECTROSCOPY

Several spectroscopic programs rely on targets generated from the PS1/*photpipe* data stream. The primary source of classification spectra is a multipurpose CfA program at the MMT to observe PS1 transients (PI Berger). Other spectra were obtained through Gemini programs

to observe exotic transients and superluminous SN (PIs Berger, Smartt, and Chornock), a Gemini program to observe transients with faint hosts (PI Tonry), a Magellan program to obtain high-SNR spectra of SN Ia (PI Foley), and Magellan and William Herschel programs to observe unusual transients and superluminous SN (PIs Berger, Chornock, and Smartt). Ongoing programs that will create a larger sample of well-observed SN Ia from Pan-STARRS1 include a program on Gemini (Foley, PI) and at Keck using NASA time (Kirshner, PI.) to select targets for further study in the rest frame IR with HST. The target selection for each program varies significantly, but all begin with identifying potential targets from the PS1/*photpipe* data stream. We only have sufficient spectroscopic resources to obtain spectra of ~10% of the PS1 transients, so potential targets must then pass several selection criteria, which again depend on the program. The most important criteria are position and brightness. Magellan and Gemini-South can only point to the five equatorial and southern MDFs. Observations at Magellan and the MMT are generally limited to targets with $r_{P1} < 22$ mag, the WHT is limited to $r_{P1} < 21.5$ mag, while fainter targets can be observed at Gemini. Generally, an effort was made to observe transients close to their peak brightness. Several programs specifically target transients with very faint host galaxies, while others attempt to observe transients with host galaxies that have a particular photo-z. Although many transients are targeted specifically as potential SN Ia, a significant number of SN Ia in our sample were originally targeted as possible non-SN Ia transients.

Spectroscopic observations of PS1 targets were obtained with a wide variety of instruments: the Blue Channel Spectrograph (Schmidt et al. 1989) and Hectospec (Fabricant et al. 2005) on the 6.5-m MMT, the Gemini Multi-Object Spectrographs (GMOS; Hook et al. 2004) on both Gemini North and South, the Low Dispersion Survey Spectrograph-3 (LDSS3[22]) and the Magellan Echellette (MagE; Marshall et al. 2008) on the 6.5-m Magellan Clay telescope, and the Inamori-Magellan Areal Camera and Spectrograph (IMACS; Dressler et al. 2011) on the 6.5-m Magellan Baade telescope, and the ISIS spectrograph on the WHT. Nod-and-shuffle techniques (Glazebrook & Bland-Hawthorn 2001) were used with some GMOS (North and South) observations to improve sky subtraction in the red portion of the spectrum.

Standard CCD processing and spectrum extraction were accomplished with IRAF[23]. The data were extracted using the optimal algorithm of Horne (1986). Low-order polynomial fits to calibration-lamp spectra were used to establish the wavelength scale. Small adjustments derived from night-sky lines in the object frames were applied. For the MagE spectra, the sky was subtracted from the images using the method described by Kelson (2003). We employed our own IDL routines to flux calibrate the data and remove telluric lines using the well-exposed continua of the spectrophotometric

standards (Wade & Horne 1988; Foley et al. 2003, 2009a; Silverman et al. 2012a).

With fully calibrated spectra, we classify the PS1 objects by physical origin. SNe, having broad (~10,000 km s^{-1}) spectral features, are very distinct from AGNs, galaxies, stars, and other astrophysical objects. However, it can occasionally be difficult to distinguish among SN types. High-redshift SN spectra typically have low signal-to-noise ratio (S/N) and considerable host-galaxy contamination, while spectra of the highest redshift SNe will lack the Si II $\lambda6355$ feature. We have implemented the SNID algorithm (Blondin & Tonry 2007) to aid in SN classification.

For SNID, as well as any SN spectral fitting routine, the output is dependent on the input parameters such as wavelength range. Because of the different approaches and the various input parameters, it is possible for different fitters to suggest different classifications. However, humans ultimately classify each object, and reasonable inputs to the fitters should yield similar results. Unless there is a confident classification, the SN is discarded.

In Table 10, we present a full list of our observations (date of observation, telescope/instrument, and exposure times) of all spectroscopically confirmed SNe Ia detected in the Pan-STARRS1 photometric data spanning from 2009 September to the end of 2011 May. We also include information about the nature of each object (redshift, phase, and light-curve shape) in Table 11. The middle panel of Figure 1 shows the redshift distribution of the spectroscopically confirmed SN Ia. Since this period includes the ramp-up of Pan-STARRS1 operations, our detection efficiency increased over time due to improved reductions, deeper templates, and longer history to identify and differentiate between the transients and variables. In addition, access to telescopes, weather, and Pan-STARRS1 downtime influenced our spectroscopic follow-up efficiency. In particular, the annual monsoon rainstorms at the MMT in July along with the August telescope shutdown resulted in poor follow up for the summer fields (primarily MDFs 9 and 10). Our spectroscopic follow-up rate for SN Ia is ~1.5 deg^{-2} yr^{-1} and constant within the uncertainties out to a radius of ~1.3 degrees in each field (see lower panel of Figure 1). In Figure 2, we show the peak magnitudes of spectroscopically confirmed SN Ia as well as events having a high likelihood of being SNe Ia based on light-curve only classification (Sako et al. 2011). Unsurprisingly, spectroscopic follow-up favored brighter transients. As Figure 2 indicates, our 5-sigma detection limit for identifying transients provides good light curves for SN Ia with $m < 24$, while our spectroscopic sample consists principally of objects with $m < 22$. The Malmquist bias introduced by this selection is discussed in §8.

5. LIGHT CURVES WITH THE TRANSIENT PHOTOMETRY PIPELINE

The goal of the transient alert system is to produce light curves of potential transients in a quick and robust way to distribute them for validation and follow-up spectroscopy. However, for measuring distance, the main focus is on minimizing the random and systematic uncertainties in the light curves. Therefore, we have set up a transient photometry pipeline (*transphot*), which is

---

[22] http://www.lco.cl/telescopes-information/magellan/instruments-1/ldss-3-1

[23] IRAF: the Image Reduction and Analysis Facility is distributed by the National Optical Astronomy Observatory, which is operated by the Association of Universities for Research in Astronomy, Inc. (AURA) under cooperative agreement with the National Science Foundation (NSF).
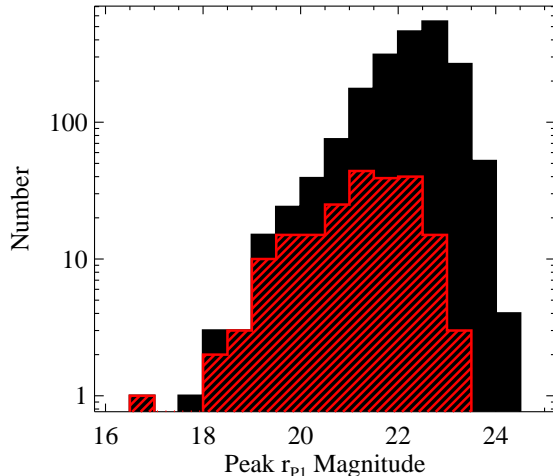
Figure 2. Histogram of r_{P1} peak magnitudes of spectroscopically confirmed SN Ia (red) and events classified as highly likely SN Ia (black) based on light-curve fitting with PSNID (Sako et al. 2011).

closely related to *photpipe* and uses most of its features, but differs in some significant ways, described below. The overall process can be summarized as such: Templates from stacking multiple images at a given sky position are constructed to allow for accurate WCS registration and image subtraction to measure photometry. From the subtracted images of supernovae, a SN centroid is determined and forced photometry is performed at that position on all images, using the PSF determined from neighboring stars for that epoch. Afterwards, the errors of the SN measurements and the baseline flux is adjusted so that the reduced chi-squared of the measurements of the supernova that do not have supernova light will be unity.

5.1. *Templates*

The templates are created through a custom calibration and stacking process. The 8 dithers from a single night are reduced and combined into a "nightly stack" by IPP with a variance-weighted scheme (see §3).

The "deep stack" is constructed by combining nightly stacks (typically ∼30), weighted by the product of the inverse variance and the inverse area of the PSF. This prescription is nearly optimal for point-source detection and photometry (Tonry et al. 2012a). The typical seeing values determined by *DoPHOT* for deep stacks that use all available epochs are shown in Table 1 (Tonry et al. 2012a). The typical 5σ detection limit in these deep stacks is ∼25.2,25.4,25.4,25.0 for $griz_{P1}$, respectively. To create the deep templates for a given SN, we only use epochs with no SN flux in the images. This ensures the

spatial consistency of the PSF, and also minimizes errors introduced by imperfect image subtraction kernels. In general, if there is no SN flux in the template, only the extended flux contribution from the galaxy is subtracted from the image. Such spatially extended sources are less susceptible to imperfections in the kernel than point sources, minimizing the difference image residuals at the position of the SN. The main disadvantage of templates that only use epochs that contain no SN flux is the template's lower SNR than templates that use all epochs. However, since even in these templates the SNR is still significantly higher than the SNR in the single epochs (nightly stacks), the SNR in the difference image is only marginally degraded.

5.2. *SN Centroids*

Determining the correct position of the SNe is important for two reasons. (1) For many epochs, the flux of the SN is below the detection limit. (2) Even if the flux of the SN is above the detection limit, its measurement is biased toward higher fluxes due to Poisson fluctuations in the sky background (see §5.3.2 for a detailed discussion).

In order to achieve good centroiding, an accurate world coordinate system (WCS) solution for each image is needed. Additionally, the uncertainties in the position vary significantly due to their strong dependence on the SNR of the flux and the seeing of the image. Therefore it is important to have an accurate understanding of the uncertainties in order to calculate an unbiased weighted average centroid. In Appendix A, we determine the accuracy of our WCS solution. The astrometric uncertainty σ_a of a given detection has a floor mostly due to pixelization (σ_{a1}), and in addition a random error σ_{a2}, which is scaled by the square of the ratio of the FWHM of the image and the SNR of the detection:

$$\sigma_a^2 = \sigma_{a1}^2 + \sigma_{a2}^2 \left(\frac{\text{FWHM}}{\text{SNR}}\right)^2 . \tag{1}$$

As described in Appendix A, for Pan-STARRS1 we conservatively use $\sigma_{a1} = 40$ mas and $\sigma_{a2} = 1.5$ to calculate the astrometric uncertainty of a single detection. The detections are grouped into transient objects, for which the 3σ clipped and weighted average centroids are calculated. The accuracy of the centroid has a small effect on the accuracy of the photometry (see Figure 5), and we discuss how we correct for this effect as described in §5.3.2 and Appendix D.

5.3. *Light Curves*

The modeling and fitting of the PSF is one of the main potential sources of systematic biases in the photometry. For the alert system, we use a customized version of *DoPHOT*, which is quick, robust, and produces adequate photometry for alerts. However, this *DoPHOT* version uses an analytic PSF that does not capture the non-Gaussian PSF tails in the Pan-STARRS1 images, which was especially important during the first year while the optical system was being perfected. This can introduce biases at the level of a few percent between faint and bright stars. For more precise photometry, we employ *DAOPHOT* (Stetson 1987) as implemented in IDL, which fits an empirical correction in addition to the Gaussian model.

5.3.1. *Linearity*

Figure 3 shows the magnitude difference between the deep and nightly stacks, $\Delta m = m_{\rm deep} - m_{\rm nightly}$, versus the deep stack magnitudes (black dots) for the various Pan-STARRS1 filters. For magnitudes fainter than 17.5, the agreement is excellent, and the average residual is on the order of 1 mmag and in general within the uncertainties (with the exception of the faintest magnitudes, where the expected Malmquist bias can be seen). A small systematic bias can be seen for the very brightest magnitude bins. In particular, for the $i_{\rm P1}$ filter, the average $\Delta m = 0.017 \pm 0.0013$ mag for the bin with $i_{\rm p1,deep} \approx 17$ mag is significantly above zero. This is most likely the result of imperfect stacking algorithms of stars close to or at the saturation limit, and we therefore exclude all stars brighter than $m = 17.5$ mag for determining the zero point of an image or the difference image kernel. No detections from our SN light curves fall into this magnitude range, therefore we set the systematic bias due to non-linearity of the photometry to 1 mmag (see Table 4).

We also tested the linearity of the PS1 detectors by comparing it to an outside catalog. We convert $r_{\rm SDSS}$ from stripe 82 into Pan-STARRS1 natural system magnitudes, and calculate the difference, shown in Figure 4. For $r_{SDSS} < 19$, the average differences are smaller than 1 mmag, which is an upper constraint on the linearity over this magnitude range. For larger magnitudes we are susceptible to a Malmquist bias in the SDSS magnitudes.

5.3.2. *Forced Photometry*

For each SN, we calculate the weighted average position and then perform forced photometry in every difference image at this position. Because we convolve the template, the PSF shape in each difference image is the same as the one in the original image and is kept unchanged. The only free parameter is the peak value of the PSF.

The success of this photometry method strongly depends on the accuracy of the WCS solution. If the WCS accuracy is poor, the forced position is off the true peak and the flux is underestimated. This effect is strongest for high-SNR measurements. In Figure 5, we show the magnitude difference Δm between the forced photometry and photometry where the centroid of the SN is determined in each individual image versus the SNR of the forced photometry. At high SNR, the average magnitude difference is an insignificant 0.5 mmag different from zero. Though there is some scatter in the magnitude differences, the scatter is small compared to the Poisson noise. This makes sense, because the same data are used with both methods. The important result is that, for high SNR, the scatter is small, symmetric, and shows no significant bias. If there are any problems with the astrometric calibration, centroiding, or differences between forced and unforced PSF fitting, systematic differences would occur. In Appendix D, we quantify the photometric bias introduced by centroiding uncertainties, and calculate the expectation value of this bias for each SN depending on its centroid uncertainty (see Figure D3). Since the uncertainty in the centroid is larger at higher redshift, there is a redshift dependence of this bias of
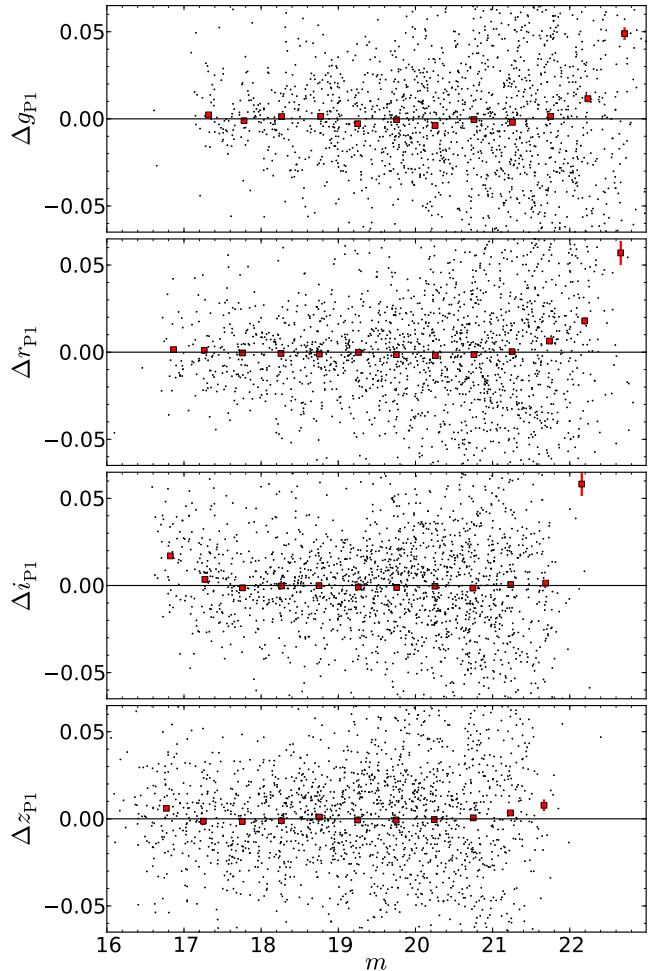
Figure 3. Comparison between deep and nightly stack photometry for stars in the MDFs. The red circles indicate the weighted average of the magnitude difference $\Delta m = m_{\rm deep} - m_{\rm nightly}$ from 100 randomly selected images for each of $griz_{\rm P1}$ from top to bottom, respectively. They are consistent with zero within the errors at all magnitudes except at the very brightest and faintest ends. In particular $i_{\rm P1}$ and $z_{\rm P1}$ show significant deviation from zero for $m < 17$ mag. Malmquist bias is likely the cause of the deviation at faint magnitudes. The black dots show a small subset of Δm values for illustration.

$\sim$2 mmag from low to high redshift. We correct the light curves for this photometric bias and estimate that the residual photometric bias is less than 1 mmag (see Table 4). Another advantage of forced photometry is that it does not suffer from a photometric Malmquist bias at low SNR. This effect can be seen in Figure 5. At SNR = 10 and 3, the regular photometry is on average brighter by 0.5% and 2.5%, respectively.

There is additional uncertainty since we perform forced photometry on the SNe, but "regular" photometry (i.e. free x,y positions) on our field stars from which we determine the zeropoint. We have chosen reference stars for our photometric calibration that have a SNR$\geq$20. For such stars, the difference between regular and forced photometry is smaller than 2 mmag (see Figure 5). This has been added to our systematic error table (see Table 4). A technique to mitigate this effect is to do forced photometry for both the field stars and SNe (e.g., Astier et al. 2006).

Figure 4. Comparison between r_{P1} and r_{SDSS}, where r_{SDSS} is the SDSS r band magnitude converted into Pan-STARRS1 natural system magnitudes using Equation 6 and Table 6 from T12b. The red circles indicate the average of the magnitude difference.
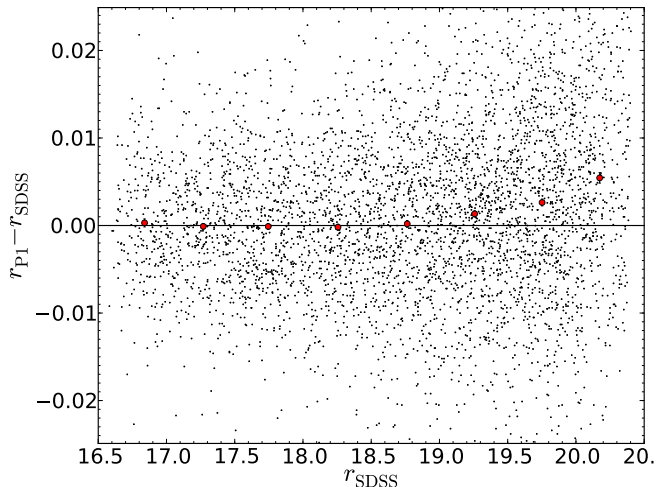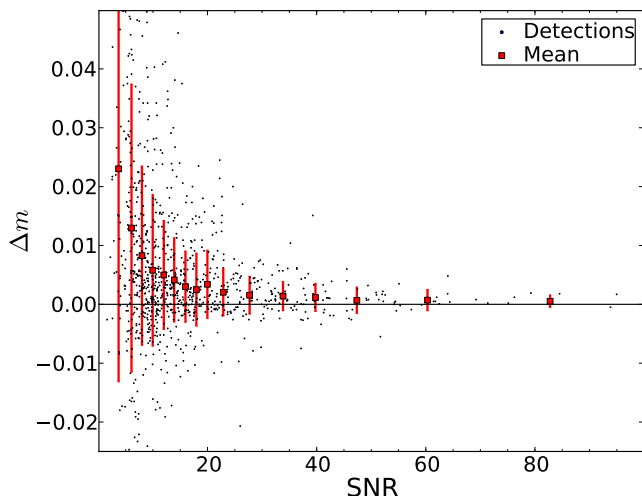

Figure 5. Comparison of forced and regular photometry for PS1 SN Ia as a function of SNR. The red circles indicate the weighted average of the magnitude difference $\Delta m = m_{\mathrm{forced}} - m_{\mathrm{regular}}$ of SN detections for different SNR bins. The error bars indicate the standard deviation. The black dots show a small subset of Δm values for illustration. At high SNR, the average magnitude difference is an insignificant 0.5 mmag different from zero, indicating that there are no issues with the astrometric calibration, centroiding, or differences between forced and unforced PSF fitting.

5.3.3. *Empirical Adjustment of Uncertainties*

In our pipeline, the variance terms are propagated through all of the image processing. However, this underestimates the true uncertainties in the measurements since the resampling process as well as kernel-matching one image to the other introduces covariance between the pixels. In order to empirically determine by how much the uncertainties are underestimated, we measure the flux f_r and its uncertainty σ_r at random positions in a given difference image in exactly the same way as we measure the SN flux. We calculate the weighted mean of the flux measurements $\bar{f}_r$, excluding outliers by a 3-sigma cut. This $\bar{f}_r$ is an empirical estimate of the systematic bias in the photometry at any position for that partic-

ular difference image, and we correct all photometry of that image with $\bar{f}_r$. This value is typically on the order of ~ 3 ADU. We then estimate the factor s_r by which the uncertainties are underestimated using the reduced chi-square $s_r = \sqrt{\chi_r^2}$, as described in more detail in Appendix C. Figure 6 shows the histograms of s_r for all difference images and filters used for the SN light curves. The histograms for $griz_{\mathrm{P1}}$ are nearly identical with a
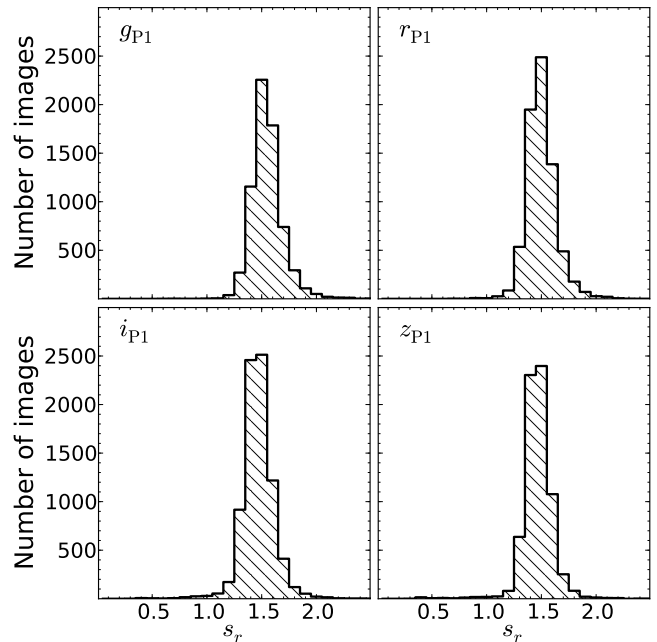
Figure 6. Histogram of the empirical multiplicative factor s_r which is used to correct the flux uncertainties of a given difference image.

peak at $s \sim 1.5$, with the bluer filters having slightly higher values since on average their larger PSF leads to larger convolution kernels and thus to more covariance. We empirically correct the difference image uncertainties by multiplying them with s_r. Note that this is a multiplicative correction since the ratio of covariance to variance is independent of the flux level in a given pixel. In §5.3.4 we show that the baseline (pre-SN) flux uncertainties are in general very good representations of the true uncertainties, since their reduced chi-square distribution has a peak at 1.0. A similar approach of empirically adjusting the uncertainties has been applied to the SNLS data (Astier et al. 2006). An alternative approach is to apply "scene modeling" (Holtzman et al. 2008), which fits a scene that includes the SN and a model of its environment to the data in the original, unwarped image, thus avoiding the complication of correlated pixels.

5.3.4. *Baseline Flux Adjustment*

We construct the templates on the assumption that there is no SN flux present. However, stacking images is not a perfect process and there may be some small biases in the template construction (e.g., SN flux included in some images, or artifacts from different PSF sizes). Since we always subtract the same template from each image, this single realization of noise creates the same systematic offset in every difference image measurement

of a given SN, and directly affects the peak magnitude of the SN. We therefore correct all the light curves by the average baseline flux calculated from the fluxes where there is known to be no SN flux, as described below. This correction is equivalent to creating a deep stack with all available images, but in addition, it corrects for any imperfection in the template stack creation and photometry.

We note that even after the baseline flux adjustement, there is still some small Poisson uncertainty left since a finite number of measurements were used. However, this uncertainty is very small compared to the uncertainty in a single epoch, and it does not bias the light curve fits in a significant way.

We calculate the weighted average of all forced photometry difference image measurements at epochs that are < -30 days or > 200 days from maximum for each SN, and subtract this baseline flux from all SN light curve measurements. We find that the calculated offsets are on average zero. However, the standard deviation of the distribution of these offsets is 24 ADUs for a zeropoint of 30.0. The significance of correcting with these offsets depends on the magnitude of the SNe. For example, 24 ADUs correspond to 3 and 41 mmag to SNe of magnitude 19 and 23, respectively. Thus, this correction is non-negligible for an individual SN, in particularly for faint ones. However, since the baseline flux correction distribution is symmetric and centered around zero, we find that any systematic bias possibly introduced to the peak magnitude can only be very small, and we assign an upper limit of 1 mmag to it (see Table 4).
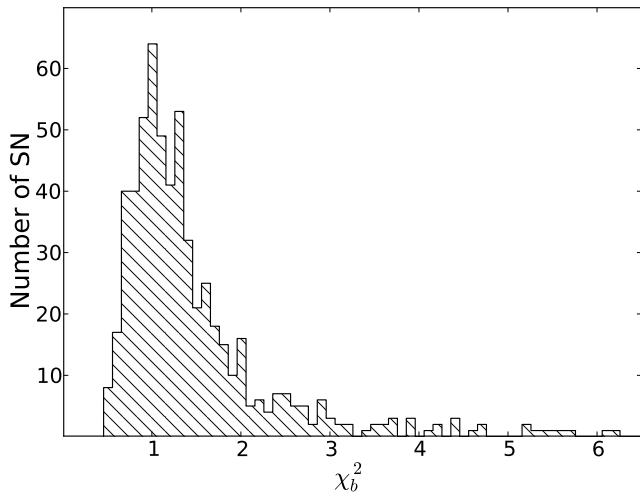

Figure 7. Histogram of the baseline flux reduced chi-square χ^2_b. Note that the peak of the distribution is very close to unity, indicating that the difference image uncertainties are a good representation of the true errors. The tail toward large χ^2_{norm} is most likely due to difference image artifacts due to bright host galaxies in close proximity to the SN.

The normalized χ^2_b from the baseline flux calculation is shown in Figure 7. The peak of the distribution is very close to one, indicating that our measured uncertainties are generally good estimates of the true uncertainties. There is a tail toward large χ^2_b, which we have determined is due to difference image artifacts introduced by bright extended sources near the position of the SN. This effect

is particularly strong at the center of bright sources, and the outliers in the χ^2_b are exclusively SNe Ia close to the nucleus of a bright galaxy.

Since these artifacts have a net flux of zero, they do not introduce a systematic bias into the photometry, but the large background variation near these artifacts artificially increases χ^2_b. This effect reduces the quality of the light curve fits for some supernovae, which do not pass our quality cuts for further analysis. Future analyses that seek the largest useful sample should address this problem.

Table 3
Light curve of PS1-10hu

Name	MJD	Filter	Flux f	Magnitude m
PS1-10hu	55230.60229	g	20.0 ± 21.5	$\cdots$
PS1-10hu	55233.53140	g	-5.8 ± 24.8	$\cdots$
PS1-10hu	55236.59489	g	-0.9 ± 15.4	$\cdots$
PS1-10hu	55248.52526	g	-1.4 ± 7.8	$\cdots$
PS1-10hu	55272.56808	g	1550.3 ± 25.6	19.52 ± 0.02
PS1-10hu	55275.51514	g	1387.7 ± 34.2	19.64 ± 0.02
PS1-10hu	55326.41381	g	119.6 ± 20.2	22.31 ± 0.17
PS1-10hu	55230.61622	r	7.2 ± 20.6	$\cdots$
PS1-10hu	55233.54702	r	-32.2 ± 28.7	$\cdots$
PS1-10hu	55236.60945	r	18.3 ± 13.7	$\cdots$
PS1-10hu	55248.53908	r	-3.9 ± 8.4	$\cdots$
PS1-10hu	55251.52352	r	34.9 ± 32.9	$\cdots$
PS1-10hu	55266.55484	r	1487.1 ± 36.2	19.57 ± 0.02
PS1-10hu	55272.58426	r	1652.1 ± 25.6	19.45 ± 0.02
PS1-10hu	55275.52937	r	1614.2 ± 98.5	19.48 ± 0.07
PS1-10hu	55305.35085	r	471.3 ± 20.1	20.82 ± 0.04
PS1-10hu	55326.42714	r	221.3 ± 31.0	21.64 ± 0.14
PS1-10hu	55332.32633	r	202.3 ± 10.8	21.73 ± 0.05
PS1-10hu	55231.58320	i	9.8 ± 13.7	$\cdots$
PS1-10hu	55234.55779	i	-16.7 ± 13.4	$\cdots$
PS1-10hu	55237.57200	i	-15.3 ± 12.1	$\cdots$
PS1-10hu	55240.53452	i	20.3 ± 11.1	$\cdots$
PS1-10hu	55243.53133	i	-5.7 ± 23.1	$\cdots$
PS1-10hu	55246.46399	i	18.1 ± 15.7	$\cdots$
PS1-10hu	55249.55923	i	-9.7 ± 11.0	$\cdots$
PS1-10hu	55252.55308	i	178.6 ± 32.6	21.87 ± 0.18
PS1-10hu	55288.44303	i	771.3 ± 25.1	20.28 ± 0.03
PS1-10hu	55297.34091	i	709.2 ± 20.4	20.37 ± 0.03
PS1-10hu	55303.48521	i	585.3 ± 17.4	20.58 ± 0.03
PS1-10hu	55327.42882	i	185.2 ± 28.8	21.83 ± 0.16
PS1-10hu	55330.30423	i	185.8 ± 12.9	21.83 ± 0.07
PS1-10hu	55339.28203	i	283.2 ± 56.7	21.37 ± 0.20
PS1-10hu	55348.34014	i	126.0 ± 19.1	22.25 ± 0.15
PS1-10hu	55235.58945	z	16.3 ± 21.6	$\cdots$
PS1-10hu	55238.56725	z	0.2 ± 16.4	$\cdots$
PS1-10hu	55241.49175	z	10.3 ± 25.7	$\cdots$
PS1-10hu	55247.53664	z	-24.9 ± 16.5	$\cdots$
PS1-10hu	55250.57895	z	0.7 ± 16.0	$\cdots$
PS1-10hu	55268.58466	z	865.0 ± 33.8	20.16 ± 0.04
PS1-10hu	55280.35431	z	548.8 ± 14.8	20.65 ± 0.03
PS1-10hu	55298.39193	z	572.0 ± 23.1	20.61 ± 0.04
PS1-10hu	55304.31987	z	548.5 ± 18.1	20.65 ± 0.03
PS1-10hu	55322.38723	z	254.3 ± 18.1	21.49 ± 0.07
PS1-10hu	55325.36617	z	171.4 ± 16.9	21.92 ± 0.10
PS1-10hu	55334.33428	z	186.9 ± 11.0	21.82 ± 0.06
PS1-10hu	55340.28431	z	203.3 ± 36.0	21.73 ± 0.18

Note. — An abbreviated example PS1 light curve - PS1-10hu. The light curves of all SNe in the cosmological sample are available in machine-readable format in the electronic edition. Only photometry within 40 days before and 100 days after maximum at MJD=55270 is presented here. All fluxes f are with respect to a zeropoint of 27.5, and the magnitudes are accordingly calculated as m=-2.5log10(f)+27.5. We only show magnitudes m for fluxes with at least 3σ significance.

In Figure 8 we show representative Pan-STARRS1 SNe Ia light curves: PS1-10hu, PS1-10caz, and PS1-10bzp with redshifts of 0.13, 0.33, and 0.64 from top

to bottom, respectively. The solid lines are their respective light curve fits as described in §7. The light curves are available in machine-readable format in the electronic edition. As an abbreviated example, we show the light curve of SN PS1-10hu in Table 3.
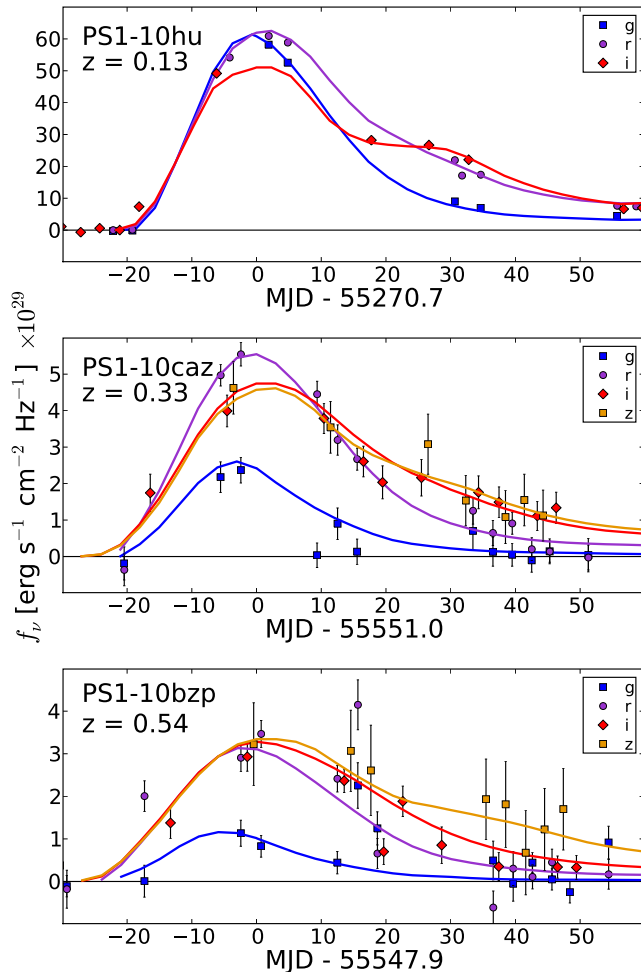

Figure 8. Example light curves for three Pan-STARRS1 SN Ia at different redshifts. MJD offset are applied so that zero is the time of maximum in rest-frame B. The SALT2 fits are shown with the solid lines.

6. PHOTOMETRIC CALIBRATION

As Sullivan et al. (2011) has pointed out, our ability to constrain the properties of dark energy from SN Ia observations is limited by systematic errors from the photometric calibration. The unique area and depth of our SN survey creates the opportunity to observe supernovae over a wide redshift range with the same telescope and filters. This improves the potential for minimizing calibration errors.

Tonry et al. (2012b) measures the system passbands, including both the instrumental sensitivity and atmospheric transmission functions. The PS1 photometric system is fundamentally based on HST Calspec spectrophotometric observations. For 7 Calspec standards, Tonry et al. (2012b) determines slight adjustments to the bandpasses so that the photometry of the standards

best agrees with the spectrophotometry of the standards with HST spectra. The fields with Calspec standards are passed to Schlafly et al. (2012), which performs the ubercal calibration that ties the observations of stars in these fields with stars across the entire 3pi survey. The zeropoints set by Tonry et al. (2012b) are mostly preserved in this stage, though may be slightly adjusted so that there is optimal relative calibration across the sky. The Medium Deep fields are calibrated in this process. S14 then checks this process by analyzing the photometry of all the Calspec standards observed in the full 3pi survey and comparing the photometry to the synthetic photometry of the positions. S14 finds the AB offsets so that the photometry and spectrophotometry agree. The offsets found here are applied to all of the Medium Deep field photometry and SN light curves.

The total systematic uncertainty in the PS1 calibration may be broken down into four parts: the instrumental response function, the propagation of zeropoints across the medium deep fields, the adherence of the PS1 zeropoints to the AB system, and spatial/temporal variation in the photometric calibration. The uncertainty of the instrumental response function is given in Tonry et al. (2012b) (T12b hereafter). This analysis also details the full systematic uncertainties in the Pan-STARRS1 implementation of the AB system, though we have redone a significant amount of the error accounting. The uncertainty in the propagation of zeropoints across the sky must be included as there are 10 Medium Deep Fields with large separations in distance. We use the results of Schlafly et al. (2012) to correct for this. The adherence of the PS1 calibration to a true AB system is analyzed in detail by the companion paper S14. Finally, the spatial and temporal variation of the instrumental response function is analyzed in this paper.

Our entire systematic error budget for calibration is summarized in Table 4. We find that after accounting for the full systematic error budget, the overall systematic uncertainty for each filter is ~ 0.012 mag without including the uncertainty in the *HST* Calspec definition of the AB system. We briefly review the uncertainties that are discussed in external work, and analyze the remaining uncertainties below.

Table 4
Photometric Calibration Error Budget

Source	Uncertainty [Millimag]	Section
Photometric Non-linearity	1	5.3.1
Centroid Accuracy	$\lesssim 1$	App. D
Forced photometry	2	5.3.2
Baseline Flux Correction	$\lesssim 1$	5.3.4
Instr. Response Function	3	6.1
Flux determination	5	6.1
Net offset wrt Calspec	8,5,6,3	3.2 in S14
Zeropoint propagation	3	6.1
Spatial variation	5,6,4,6	6.2
Temporal variation	3	6.2
Total Internal PS1	~ 12	
SED conformity to AB	5-15	3.2 in S14

Note. — The dominant systematic uncertainties in defining the Pan-STARRS1 photometric system. If four numbers are given, they refer to $griz_{P1}$, respectively. We assign a range of uncertainty to the SED conformity to the AB system, since the color dependence is not easily enumerated and is discussed in more detail in S14. The bandpass uncertainties is included into the instrumental response function and also discussed in S14.

6.1. *Absolute Calibration and All-Sky Photometry*

The system's response function naturally divides into the instrumental response function (mirrors, optics, filters, and detectors) and the atmospheric extinction. In principle it is possible to determine these two components independently without the reliance on standard stars: The atmospheric extinction can be determined with measurements and modeling, while the instrumental response function can be traced with a high-accuracy NIST-calibrated photodiode in combination with a tunable laser system (Stubbs & Tonry 2006; Stubbs et al. 2010). In practice, however, the calibration accuracy is improved by including observations of spectrophotometric standards, which provide the overall normalization of the photometric system and can verify the derived system and atmospheric response functions. T12b describes in detail how the Pan-STARRS1 photometric system has been determined with this recipe.

The Calspec standards, and thus also the Pan-STARRS1 photometry, are fundamentally based on models of hydrogen white dwarf atmospheres and the absolute flux for Vega in the V band (Bohlin 2007). Substantial work has been invested in improving the HST spectrophotometric standards (e.g. Colina & Bohlin 1994; Bohlin 1996; Bohlin et al. 2001), and they have the distinct advantage that the Calspec standard star observations are not marred by the atmosphere. However, even in space, complications like charge transfer efficiencies, non-linearity of detectors, and secular degradation of the optics and detectors contribute to systematic measurement biases (Bohlin 2007). Combining all this, we adopt a systematic error of 5-15 mmag from non-conformity of the HST Calspec standards to the AB system, depending on wavelength (Bohlin & Gilliland 2004). This wavelength dependence is further discussed in S14.

The Pan-STARRS1 survey observed 7 standard stars (1740346, KF01T5, KF06T2, KF08T3, LDS749B, P177D, and WD1657-343) on MJD 55744 (UT 02 July 2011) in photometric conditions at a wide range of airmasses in all filters. The stars were placed on the same CCD detector/amplifier, which we chose to be away from the center of the field, where spatial variation in the PSF adds additional uncertainty to photometric measurements as shown in §6.2. In theory, a common normalization to all filters should be sufficient to match the observations to the synthetic magnitudes. However, the synthetic colors of the standard stars deviate from the observed colors. T12b attempts to correct for these differences by correcting the instrument response function. For the filters $griz_{P1}$, they determine the corrections to be 0.012, 0.019, 0.009, and -0.009 mag, respectively. The correction is small because the agreement between the in-situ NIST-based response function and the manufacturer's benchmark measurements of the filters and the CCD is very good. The system response function (instrument response function and atmosphere) of the Pan-STARRS1 photometric system for $griz_{P1}$ is shown in Figure 9 at an airmass of 1.2.

The photometric normalization in the limited set of fields with the Calspec standards is then propagated across the sky, encompassing all of the Medium Deep
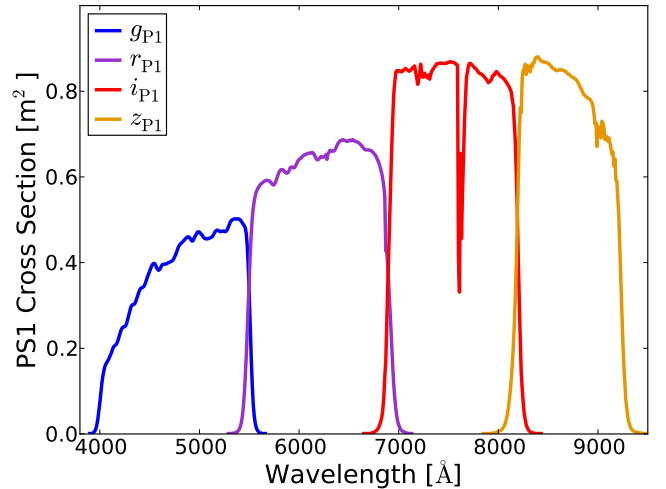
Figure 9. System response function for the four Pan-STARRS1 filters $griz_{P1}$ at an airmass of 1.2, assuming representative precipitable water vapour and aerosol exponent parameters of 0.65 cm and 0.7, respectively (T12b).

survey fields, using the same übercalibration method (Padmanabhan et al. 2008) that has been successfully used for the SDSS all-sky survey. The details of this übercalibration are described in Schlafly et al. (2012). Comparing the Pan-STARRS1 and SDSS photometry, they find that both surveys show similar photometric calibration errors. They estimate that the relative precision in g_{P1}, r_{P1}, and i_{P1} is < 10 mmag, and ~10 mmag in z_{P1}. Since we have 10 MDFs distributed over the full sky, we estimate that the uncertainty introduced by zeropoint variation is $10/\sqrt{10}$ mmag. S14 repeat the process outlined in T12b of adjusting the filter transmissions based on agreement between observed and synthetic photometry. They increase the number of Calspec standards used to 10. S14 determines that systematic uncertainties in the photometry of the standard stars are no larger than 5 mmag. They also find that small adjustments $\Delta griz_{P1}=[-0.008, -0.0095, -0.004, -0.007]$ should be added to the zeropoints defined by T12b and Schlafly et al. (2012). This improves the measurement of the offset for each filter, and reduces the systematic uncertainty due to the adjustments from 10 mmag to those given in Table 4 ("Net offset wrt Calspec").

To test the calibration, T12b finds an excellent agreement between the stellar locus constructed from observed Pan-STARRS1 photometry from a field with very low Galactic extinctions with its synthetic colors, with systematic differences of ~1%. They also transform SDSS stripe 82 magnitudes into the Pan-STARRS1 photometric system, compare them to the observed Pan-STARRS1 magnitudes, and find differences at the 1%-2% level. T12b also notes that there are differences at the same level between the different SDSS data releases. A more detailed exploration of the source of these differences is given in S14.

6.2. *Spatial and Time Variation of the Pan-STARRS1 Instrumental Response Function*

The system response function can vary with wavelength, position on the focal plane, and time. This section quantifies the systematic biases introduced by errors

in the determination of the instrument throughput.

For Pan-STARRS1, the spatial variation of the instrument response function is removed by flat-fielding and the on-sky illumination correction, which is constructed using dithered images of a dense stellar field (Magnier 2006). However, Stubbs et al. (2010) have suggested that after these corrections there may still be a residual spatial variation in the photometry that is band-dependent. To test this, we compared PS1 photometry of stars in 3 MDFs against SDSS photometry of the same stars - converted to the PS1 system of T12b (see S14 for further details). Figure 10 shows the results of this test, plotting the median difference between the Pan-STARRS1 and SDSS photometry. The most striking disagreement is in the first bin, which lies at the center of the focal plane where the optics of the telescope generate strong spatial variation of the PSF. Because the central region is so difficult to handle, we discard from our cosmological analysis the 3 SN Ia that fall in the central region (PS1-11ams, PS1-10f, and PS1-11yu) because we cannot be certain they meet our threshold for photometric fidelity.

Across the rest of the focal plane, the PS1 photometry in each filter exhibits a steady constant offset relative to SDSS, ranging from 0.5% in r_{P1} to 3% in z_{P1}. These overall differences between the synthetic and observed PS1 magnitudes are known and described in more detail in T12b and S14. They can be taken as conservative upper limits on the systematic biases in the PS1 photometry. After removing this offset, the remaining difference between SDSS and Pan-STARRS1 photometry is less than 1% in each filter - and that is further reduced to $\sim$5 mmag for all filters when systematic shifts between the MDFs are accounted for[24]. We therefore use 5 mmag as the limit for spatial consistency in our error budget (Table 4). The differences between PS1 and SDSS shown here are most likely due to flat-fielding issues, as the expected differences due to variations in the filter passbands across the focal plane are < 3 mmag for stars with colors around $0.4 < g - i < 1.4$. The photometry of SNe has a stronger dependence on these spatial variations in the filter passbands due to the broad absorption features in their spectra. As described in S14, we fit each SN light curve using the expected filter function at the position of the SN on the focal plane. Accounting for the variation of the filter functions may change the distances from their nominal values by $\sim$3 mmag. These differences are shown in S14 (Fig. 2) and are included in the distances presented in our Table 14.

Over time, the optical components may degrade or change. Color-dependent changes could introduce a systematic bias into the photometry. In Figure 11, we show the median variation Δg_{P1} in the average magnitude of stars at various epochs for different colors ($g_{P1} - r_{P1}$). Similar results are seen in each band. Typically, the median is not different than zero to within 3 mmag, and the standard deviation in a given bin is on the order of 5 mmag. No long-term trends can be discerned, and we set the upper limit on any long-term changes of the optical system to 3 mmag.

Figure 10. The median differences between the PS1 photometry and the synthetic PS1 photometry derived from SDSS using Equation 6 and Table 6 from T12b using stars in the color range $0.5 < (g-r)_{SDSS} < 0.8$ for gri_{P1} and $0.8 < (r-i)_{SDSS} < 1.1$ for z_{P1}. The median is calculated in bins of distance between the stars and the center of the MDFs. We exclude all SNe that are within 0.3 deg of the field center (red dashed lines), since in the photometric calibration in the field center is unreliable due to strong spatial variation in the PSF. The blue lines indicate the known offsets between SDSS DR8 and the Pan-STARRS1 calibration by T12b, as shown in Table 1 of S14.
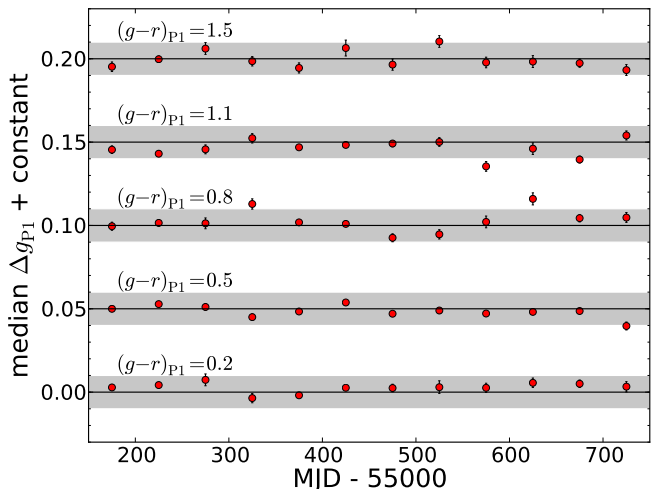
Figure 11. Median difference between the average magnitude of stars and their associated detections at different epochs for color bins of $(g - r)_{P1}$ in [0.2,0.5,0.8,1.1,1.5]. The size of the color bins is 0.1 magnitude, and only stars with $r_{P1} < 19$ were used. For clarity, offsets in steps of 0.05 are added to Δg_{P1}, and the gray shaded bars indicate a plus-or-minus 1% level deviation. No long term variation is apparent above $\pm$3 mmag, which we assign as the systematic uncertainty.

---

[24] We attribute the MDF-to-MDF variation to large scale spatial variations in the SDSS photometric system (Schlafly & Finkbeiner 2011; Schlafly et al. 2012)
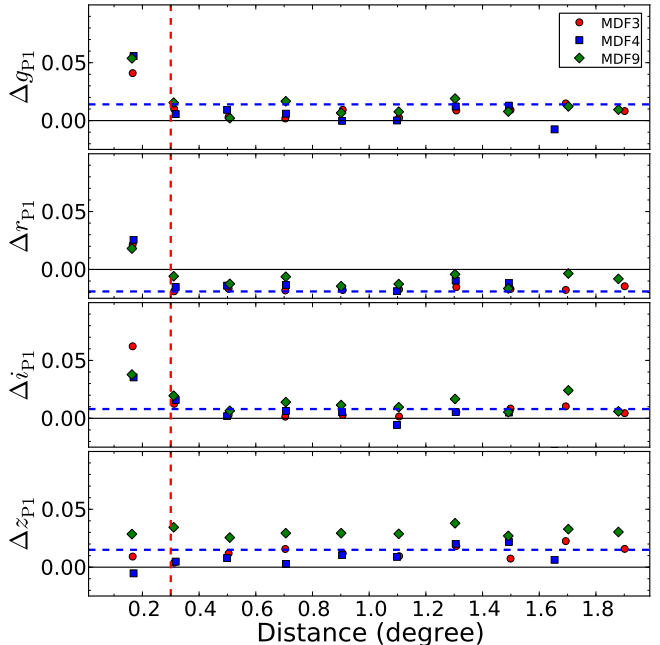
7. LIGHT CURVE FITS AND SAMPLE CUTS

7.1. *SALT2 Light Curve Fits*

Many light-curve fitters have been developed over the last decade (e.g., MLCS2K2, Jha et al. 2007; SALT, Guy et al. 2007; SiFTO, Conley et al. (2008); and BayeSN, Mandel et al. 2009, 2011). Each method makes corrections for the light-curve shape and observed color of the SN. However, there are two fundamentally different ways to apply the color correction. The first empirically determines the correlation between observed color and uncorrected distance residuals. The second uses the assumption that the observed color is the combination of intrinsic SN color, photometric errors, and reddening due to dust. The former is less model dependent, while the latter is more physically motivated.

Ultimately, these choices have small, but noticeable consequences for cosmological inferences. Kessler et al. (2009a) made an in-depth analysis of the different light curve fitters, and found that in general they agree reasonably well given the same assumptions. Currently the most widely used light curve fitter is SALT2 (Guy et al. 2007), and we use this fitter in our analysis. SALT2 explicitly matches the observations in the filters of any given survey to integrals of the warped model spectra for those passbands. It treats the color of SNe Ia entirely empirically, and is used to find an overall relation between luminosity and color. S14 explores whether the linear models used by SALT2 to describe the color and stretch-luminosity relation are adequate to fit the data.

We use the most up-to-date published version of SALT2 Guy et al. (2010) implemented in SNANA[25] (Kessler et al. 2009b). We transform our lightcurve fit parameter into distances using the Tripp formula (Tripp 1998)

$$\mu_B = m_B - M + \alpha x_1 - \beta c, \qquad (2)$$

where μ_B is the distance modulus, m_B is the peak B-band brightness, x_1 is a light-curve shape parameter, and c is a color parameter. The parameters α, β, and M are nuisance parameters. α is determined by the relation between luminosity and stretch while β is determined by the relation between luminosity and color. M is the absolute B-band magnitude of a fiducial SN Ia with $x_1 = 0$ and $c = 0$. Motivated by Schlafly & Finkbeiner (2011), we make one modification to SALT2 by replacing the "CCM" (Cardelli et al. 1989) Milky Way Galaxy (MWG) reddening law with that from Fitzpatrick (1999). Schlafly & Finkbeiner (2011) also finds that the MWG extinction values from Schlegel et al. (1998) are overestimated by 6-14%. We therefore correct our extinction values accordingly. These changes are explained further in Section 7 in S14.

We present in Table 13 and 14 the SALT2 parameters for the entire set of cosmologically useful SNe Ia from the PS1 plus low-z sample (PS1+lz). The cuts that are used to remove SNe Ia from the cosmological sample are described in the second part of this section. Distributions of the SALT2 fit parameter are shown in Figure 12.

Discrepancies in the x_1 and c distributions between the Pan-STARRS1 and low-z samples are likely due to selection effects. Most low-redshift SNe in our sample were discovered in surveys that target specific nearby galaxies (Li et al. 2011). These surveys are capable of detecting SNe Ia with more extinction than the untargeted sam-
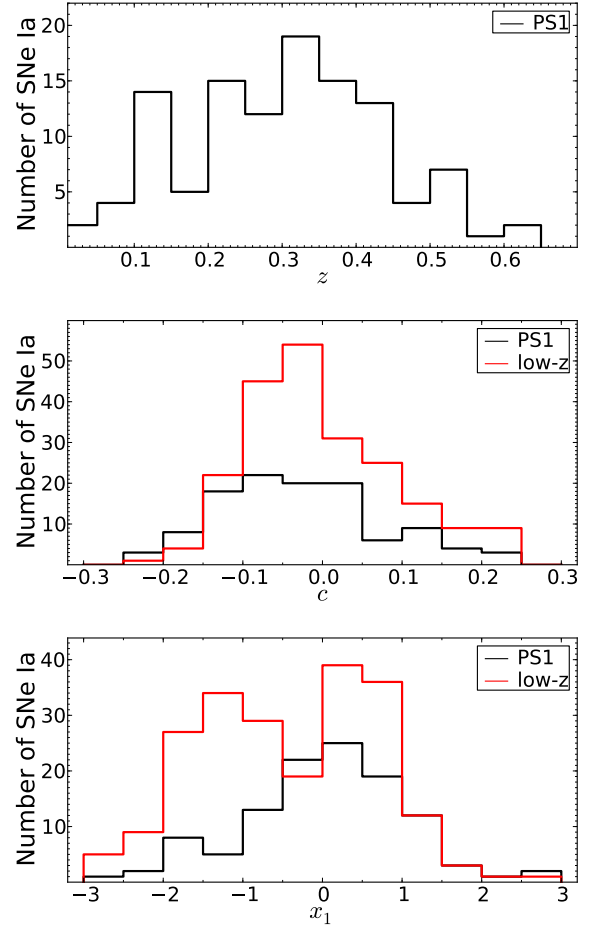
Figure 12. Histograms of redshift, color, and stretch for the Pan-STARRS1 (black solid) and low-redshift (red dashed) samples. The first bin of the low-redshift sample has 222 light curves from 197 SNe Ia. For the samples presented both color and stretch cuts were applied (see §7.2), but not the minimum redshift cut.

ple from Pan-STARRS1. We use stringent cuts on the light curve properties, as described below, that pass only about 1/2 of the low-z sample but 4/5 of the PS1 sample.

7.2. Sample Cuts

The Pan-STARRS1 survey spectroscopically confirmed 146 SNe Ia during the first 1.5 years in the MDFs. This was only a very small fraction of the ∼1700 transients with SN Ia-like light curves. While it would be ideal to use all spectroscopically confirmed Pan-STARRS1 SNe Ia to constrain cosmological parameters, we use sharp quality cuts to improve the analysis. We require that every SNe Ia has adequate light-curve coverage to properly measure a distance and that it has a light-curve fit, redshift, and Milky Way extinction that limits systematic bias in the distance. Applying these cuts, the cosmological analysis of §8 employs 113 SN Ia from the initial sample of 146 spectroscopically-confirmed Pan-STARRS1 objects.

For our low-z SN Ia, we use the following SNe Ia samples: we denote JRK07 as the compilation of SNe Ia collected by Calán/Tololo (Hamuy et al. 1996a, 29 SNe), CfA1 (Riess et al. 1999, 22 SNe), CfA2 (Jha et al. 2006, 44 SNe), and other sources (Jha et al. 2007, 28 SNe).

We also use the SN Ia compiled more recently by CfA3 (Hicken et al. 2009a, 185 SNe), CSP (Contreras et al. 2010, 85 SNe), and CfA4 (Hicken et al. 2012, 94 SNe). After applying our cuts, the low-z sample is trimmed from 497 to 222 light curves from 197 SNe Ia. Table 12 shows the effect of each cut on the different samples.

Below, we detail the cuts. We apply these criteria in three steps. Initial criteria do not require any light-curve fitting. Light curves that do not meet these standards are eliminated. First-pass criteria are determined from polynomial fits to the light curves. Light curves that pass these tests are subjected to our final criteria, which use the output of the full SALT2 light curve fit.

Initial:

1. Unambiguous spectroscopic classification as a SN Ia.

2. Not a Iax- or 91bg-like SN Ia.

3. Outside the central 0.3 deg of the MDF (Pan-STARRS1 only).

4. $z > 0.01$.

5. Galactic reddening along the line of sight of $E(B-V)_{\mathrm{MWG}} < 0.5$ mag.

6. Measurements in 2 or more filters with SNR ≥ 5.

First-pass:

7. At least 1 measurement with $-10 < t < +5$ days.

8. At least 1 measurement with $+5 < t < +20$ days.

9. 5 or more measurements with $-10 < t < +35$ days.

10. 2 or more filters with a measurement between $-8 < t < +10$ days.

Final:

11. Light curve fit converges.

12. $\mathcal{P}_{\mathrm{fit}} > 0.001$, where $\mathcal{P}_{\mathrm{fit}}$ is the SALT2 light-curve fit probability based on the χ^2 per degree of freedom.

13. $-0.25 < c < 0.25$ or $-3.0 < x_1 < 3.0$.

14. Outlier rejection (Chauvenet's criterion from Taylor (1997), 4σ)

7.2.1. *Initial Cuts*

We require spectroscopic confirmation of all SN Ia used in our cosmological analysis. We follow a method similar to that presented by Foley et al. (2009b) to determine the classification of each potential SN Ia. Briefly, we use *SNID* (Blondin & Tonry 2007) to match a SN spectrum with a library of high-SNR spectra. *SNID* provides a quantitative assessment that a particular SN is of a given class at a given redshift. Some redshifts come from host galaxy emission lines. Each supernova is ultimately classified by spectroscopists: co-authors RC and RJF. Supernovae with ambiguous classifications are eliminated. Although the classification is subjective, almost every SN in the Pan-STARRS1 cosmology sample has a

spectrum of high quality and it is unlikely that any non-SN Ia have leaked into this analysis. Similarly, there should be no catastrophic failures in the determination of the redshifts.

We specifically exclude SNe of the "Iax" subclass (Foley et al. 2013) from all samples. Although this mostly affects the low-redshift samples, SN 2009ku, a SN Iax discovered by Pan-STARRS1 (Narayan et al. 2011), is removed from our final sample. We also exclude PS1-11yj, a SN 1991bg-like object at $z = 0.107$. We decided not to include this peculiar SN because it has not yet been shown whether this subclass of SN Ia can be well represented by the training sample and has been excluded in some past surveys (e.g., Hicken et al. 2009b). The 3 SNe Ia (PS1-10f, PS1-11yu, PS1-11ams) that are within 0.3 deg of the field center are excluded, since the absolute photometric calibration is uncertain due to strong PSF variation (see §6.2).

We exclude all SNe with $z < 0.01$ to avoid objects affected by departures from Hubble's Law due to bulk flows or a regional Hubble bubble. We exclude SN with a Milky Way reddening $E(B-V)_{\mathrm{MWG}} > 0.5$ mag to avoid introducing any substantial error due to the extinction correction. These cuts affect only the low-redshift sample, and S14 provides a detailed explanation of the effects of these cuts.

7.2.2. *First-pass cuts*

We require high-quality light curves which when fit result in accurate distance measurements. One requirement is that the SNR is sufficiently large in a minimum number of observations. A large subset of requirements can be considered "coverage" cuts, where each light curve must have observations in certain phase ranges with certain filters. Finally, we require that the resulting light-curve fit parameters fall within ranges known to have low distance biases from simulations. We outline the cuts below.

For our sample, we require that there be measurements in at least two bands with SNR > 5. This requirement does not affect the low-redshift or Pan-STARRS1 spectroscopic sample; however, it does reflect our detection limits, and is a necessary requirement for simulating the survey.

The light-curve cuts applied to the PS1 sample are taken from Guy et al. (2010). Most requirements are expressed in terms of the rest-frame phase $t = (t_{\mathrm{obs}} - t_{\mathrm{max}})/(1 + z)$. While Kessler et al. (2009a) required at least one measurement with $t < 0$ days, Guy et al. (2010) found that a more flexible requirement of needing one measurement in the range of $-8 < t < 5$ days provided a similar constraint. Using simulations of the Pan-STARRS1 and low-z samples from S14, we find that SNe Ia that pass the Guy et al. (2010) cut, but not the Kessler et al. (2009a) cut only introduce a very small bias of 0.2% into the distance modulus. This bias increases to 0.4% for redshifts larger than 0.5. However, there are no high-redshift SNe Ia in our Pan-STARRS1 sample that pass the Guy et al. (2010) but not the Kessler et al. (2009a) cut.

7.2.3. *Final Cuts*

We require that the light curve fit converges and has a SALT2 light-curve fit probability $\mathcal{P}_{\mathrm{fit}} > 0.001$ based on

the χ^2 per degree of freedom. We remove all SNe Ia in our sample with $|c| > 0.25$ or $|x_1| > 3$. Colors or stretch values that deviate far from zero are not well represented in the training sample and such objects could bias the measurement of β. Where we have light curves of the same SNe from two different surveys, we take the average distance of the two so that the supernova is only treated as a single independent data point.

Finally, when fitting cosmological parameters, we apply Chauvenet's criterion (Taylor 1997) to reject outliers, removing SNe for which we could expect less than half of an event in our full sample (assuming a Gaussian distribution of intrinsic luminosities). For the PS1+lz sample, this is 4σ. This criterion does not depend significantly on our choice of cosmological parameters, and thus the same SNe are excluded for all cosmological choices. Chauvenet's criterion removes no SN Ia from the Pan-STARRS1 sample and two (SN 2004gc and SN 2008cm) from the low-z sample.

We make all data and tools used for this analysis publicly available at http://ps1sc.org/transients/

8. COSMOLOGICAL RESULTS

8.1. *Luminosity Distance Measurements*

The ultimate goal of this analysis is to put constraints on the cosmological parameters Ω_M, Ω_Λ, and w. We first transform the SALT2 fit parameters into distances using the SALT2mu program (Marriner et al. 2011), which finds the α and β parameters that minimize the distance modulus residuals for a given cosmology. While there is uncertainty in whether these parameters evolve with redshift (Kessler et al. 2009a; Conley et al. 2011), here we assume that α, β and M are all constant with redshift. In order for the χ^2_ν of the distance residuals to be unity, an intrinsic dispersion $\sigma_{\rm int}$ is added in quadrature to the error of each SN distance (which includes the distance error from redshift uncertainty)[26]. Both the intrinsic dispersion of the sample and the photometric errors of each SN distance include a dependence on the nuisance parameters and covariances between the fit parameters. The SALT2mu procedure propagates these errors and determines the values for α and β.

Table 5
Effects of Choices for Intrinsic Scatter

Intrinsic Scatter	α	β
$\sigma_{{\rm int},m_B} = 0.115$	0.147 ± 0.010	3.13 ± 0.12
$\sigma_{{\rm int},c} = 0.025$	0.141 ± 0.010	3.71 ± 0.15

Note. — Intrinsic scatter $\sigma_{{\rm int},m_B}$ and $\sigma_{{\rm int},c}$ in the PS1+lz sample, and how α and β vary for each method. The magnitudes of each scatter given above is such that the total reduced χ^2 of the sample is ~ 1.0.

There is ongoing debate about the source of the intrinsic scatter seen in SNe Ia distances. As shown in Kessler et al. (2013) and Scolnic et al. (2014), the determined values of α and β depend on assumptions about the source of the intrinsic scatter. For the PS1+lz sample, α and β are given in Table 5 after attributing the remaining intrinsic distance scatter to either luminosity

[26] $\sigma^2 = \sigma_N^2 + \sigma_{\rm int}^2 + \sigma_{\mu-z}^2$, where σ_N^2 is the photometric error of the SN distance, $\sigma_{\rm int}^2$ is the intrinsic scatter, and $\sigma_{\mu-z}^2$ is the distance error due to redshift uncertainty

variation or color variation. This is done after the SALT2 light curve fit includes a small amount of color variation in its model. We find that the intrinsic dispersion of the sample is 0.115 mag if we attribute intrinsic scatter to luminosity variation and 0.025 mag if we attribute intrinsic scatter to color variation. There is a large difference in the values of β found for these two different assumptions: $\beta = 3.13 \pm 0.12$ and $\beta = 3.71 \pm 0.15$ for the luminosity and color variation respectively. The value of β found for the color variation case is within 3σ of a MW-like reddening law. Interestingly, the low-z sample by itself pulls β to a higher value ($\beta \sim 3.9$) than the PS1 sample ($\beta \sim 3.0$) when we attribute scatter to color variation. This may be due to the different selection effects in the low-z and PS1 samples, or the incompleteness of the SALT2 training sample for blue colors (S14). Most likely related, the total intrinsic scatter of the PS1 distances is half as large ($\sigma_{\rm int} = 0.07$) as that for the low-z sample ($\sigma_{\rm int} = 0.123$). The scatter seen for the low-z sample is larger than that found in past studies (e.g., Kessler et al. 2009a) as the assumed peculiar velocity errors in this analysis are smaller. We fix different values of $\sigma_{\rm int}$ for our high and individual low-z subsamples. These values are given in S14.

The source of intrinsic scatter is explored in the companion paper S14. To summarize briefly, we create two simulations of the PS1+lz samples in which one has $\beta = 3.1$ and scatter is dominated by luminosity variation, and another in which β is consistent with a MW-like value ($\beta = 4.1$) and scatter is dominated by color variation. We then find the biases in distance over the entire redshift range from subtracting our recovered distances from the simulated distances. For both simulations, we assume the scatter comes from luminosity variation alone. Since we simulate the full sample, the discrepancies between recovered and simulated distances will also be composed of the Malmquist bias at the upper limits of our redshift ranges. The differences in distance modulus correction from the two simulations can be as high as 4%. To correct the distances, we take the average correction from these two simulations at each redshift. We do not choose one model or the other as there is insufficient empirical evidence to favor either model (S14). Understanding and correcting for the intrinsic variation of SN Ia is one of the largest systematic uncertainties in our analysis. In Figure 13, we show the bias in distances for both the low-z and PS1 sample. For any given redshift, we then interpolate the bias from this average correction vector. This bias is subtracted from all Pan-STARRS1 distance moduli.

The PS1+lz Hubble diagram with the corrected distances is shown in Figure 14. Three model universes are given: the ΛCDM universe, a universe with $\Omega_M = 1$, and a universe with $\Omega_M = 0.3$. The distance modulus $\mu(H_0, \Omega_M, \Omega_\Lambda, w, z)$ is found from the luminosity distance d_L such that $\mu = 5 \times \log(d_L) + 25$. The luminosity distance is commonly expressed as

$$d_L(z; w, \Omega_M, \Omega_\Lambda, H_0) =$$
$$(1 + z)|\Omega_k|^{-1/2} \, \mathcal{S}_k \left[c|\Omega_k|^{1/2} \int_0^z \frac{dz'}{H(z')} \right] , \quad (3)$$

where the curvature density $\Omega_k \equiv 1 - \Omega_M - \Omega_\Lambda$, and the function $\mathcal{S}_k(x) = \sin(x)$ for $\Omega_k < 0$, $\mathcal{S}_k(x) = \sinh(x)$ for $\Omega_k > 0$, and $\mathcal{S}_k(x) = x$ for a flat Universe with $\Omega_k = 0$.
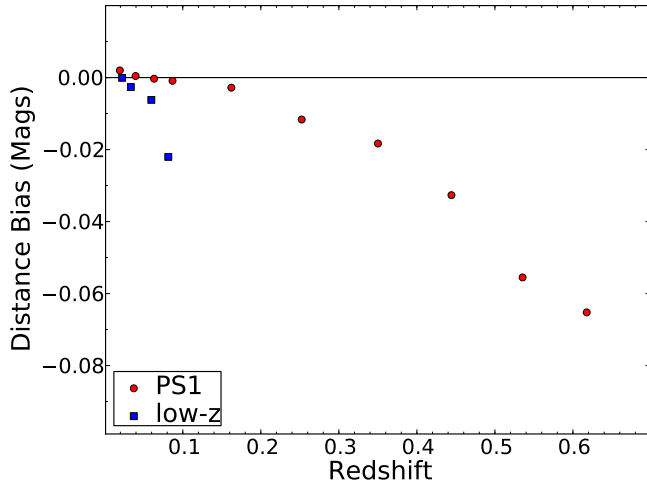
Figure 13. Distance corrections for the low-z and Pan-STARRS1 samples as a function of redshift.

Finally, the function $H(z)$ is defined as:

$$H(z) = H_0 \left[\Omega_M(1+z)^3 + \Omega_\Lambda(1+z)^{3(1+w)} + \Omega_k(1+z)^2 \right]^{1/2}$$
(4)

Cosmological constraints can be found from the SN sample with only statistical errors by measuring the χ^2 value for a grid of Ω_Λ versus Ω_M values with $w = -1$ and w versus Ω_Λ for a flat universe ($\Omega_\Lambda + \Omega_M = 1$). The Pan-STARRS1 sample does not probe high enough redshifts to provide much constraining power on evolving equations of state, and we thus assume a constant w and a flat universe when we determine the constraints for w and Ω_M.

8.2. Systematic Uncertainties

We briefly summarize the systematic uncertainty analysis detailed by S14. They derive a covariance matrix for the systematic uncertainties that may be included when determining the Pan-STARRS1 cosmological results. The most important systematic uncertainties are due to calibration uncertainties, assumptions in the light curve fitting and selection effects.

Uncertainties in the PS1 photometric system due to calibration are given in Table 4. When combining the PS1 sample with the low-z sample, we include calibration uncertainties from each of the low-z samples. These uncertainties are composed of uncertainties in bandpasses and zeropoints, as well as the uncertainty in the Landolt standards. The calibration uncertainties make up $> 50\%$ of the total systematic uncertainty of the sample. The other largest uncertainties are due to incomplete understanding of the intrinsic color of SNe Ia, selection effects and Milky Way extinction corrections. Further possible systematic uncertainties are due to dependencies of fitted distances on host galaxy properties and coherent flow effects. While we correct the redshifts of the low-z supernova for coherent flow effects (Neill et al. 2007), we currently do not correct for the dependence on host galaxy properties. This adjustment is not applied as the difference in Hubble residuals for low and high mass host

galaxies is only 0.037 ± 0.032 (S14). For the use of future studies, we present the host galaxy masses M_{host} in Table 14. The derivation of the masses is described in S14.

Following Conley et al. (2011), the uncertainties are propagated through a systematic error matrix. We define a total uncertainty matrix $\mathbf{C}$ such that $\mathbf{C} = \mathbf{D}_{\text{stat}} + \mathbf{C}_{\text{sys}}$. The statistical matrix $\mathbf{D}_{\text{stat}}$ has only a diagonal component that includes errors from the fit parameters and intrinsic scatter. While statistical covariances may arise from errors in the SALT2 template, Conley et al. (2011) finds these to be negligible. The systematic error matrix is determined by varying a given uncertainty parameter, and then finding the difference between the original distance and a newly determined distance. While the statistical covariance matrix includes components of the error budget that can in principle be reduced by adding more SNe Ia to the sample, the systematic uncertainties can be reduced with improved analysis or external data. Given a vector of distance residuals of the SN sample $\Delta\vec{\mu} = \vec{\mu_B} - \mu(H_0, \Omega_M, \Omega_\Lambda, w, z)$ then χ^2 may be expressed as

$$\chi^2 = \Delta\vec{\mu}^T \cdot \mathbf{C}^{-1} \cdot \Delta\vec{\mu}.$$
(5)

These constraints are shown Figure 15 and compared to the constraints from the statistical only sample. As the systematic uncertainties weight the errors of SNe differently, the best fit values of the recovered parameters will be shifted.

8.3. External Constraints

To better determine cosmological parameters, we include constraints from baryon acoustic oscillations (BAO; Blake et al. 2011), the CMB (Planck Collaboration et al. 2013), and the Hubble constant (Riess et al. 2011). In order to focus on the constraints from the PS1 sample and simplify the analysis, we do not include additional high-redshift SN Ia samples (e.g., SNLS and *HST*). A combination of all SN data will be left for a future study.

We follow Planck Collaboration et al. (2013) to include constraints from other surveys, as they have made the most precise measurements on the CMB, and gather data from all of the various BAO surveys to determine this constraint. The likelihood of cosmological parameters is found from the Markov chains given as an extension of Planck Collaboration et al. (2013). We note that there are still unresolved calibration discrepencies between *Planck* and *WMAP* (Hinshaw et al. 2013), and the constraints from these two surveys are compared in S14.

For *Planck*, we use their Markov chains for determining cosmological parameters. When we wish to explore a flat wCDM model, we use their $+w$ model. When we want to examine non-flat ΛCDM models, we use their $+k$ model. For all CMB constraints, we include data from the *Planck* temperature power spectrum data, *Planck* temperature data, *Planck* lensing, and *WMAP* polarization at low multipoles. For the BAO constraint, we take data from a multitude of surveys, as shown in Table 6.
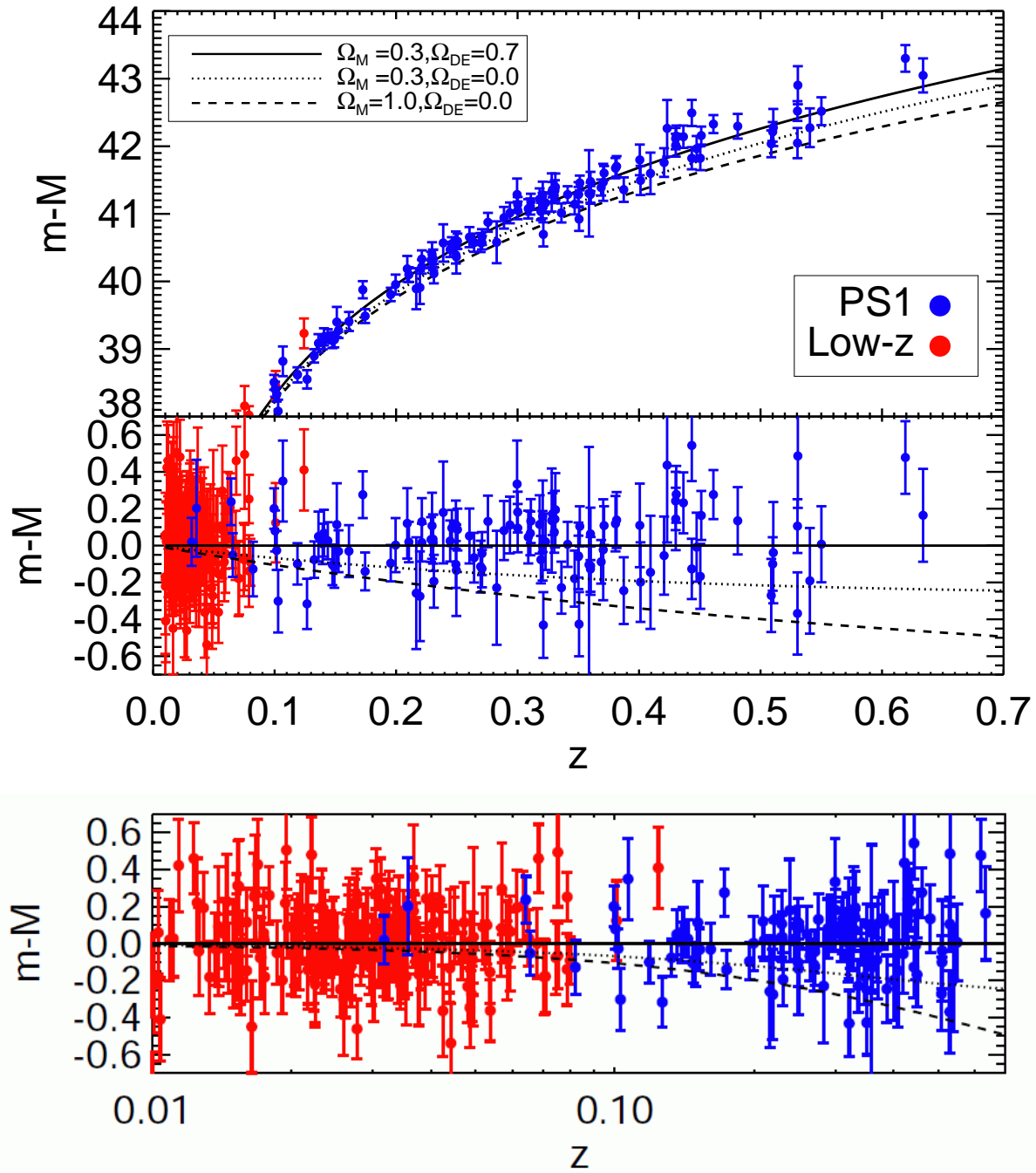
Figure 14. Hubble diagram for the combined PS1 and low-redshift sample. The bottom panel shows the difference modulus residuals versus the logarithmic redshift in order to visualize the the low-z SN Ia residuals.
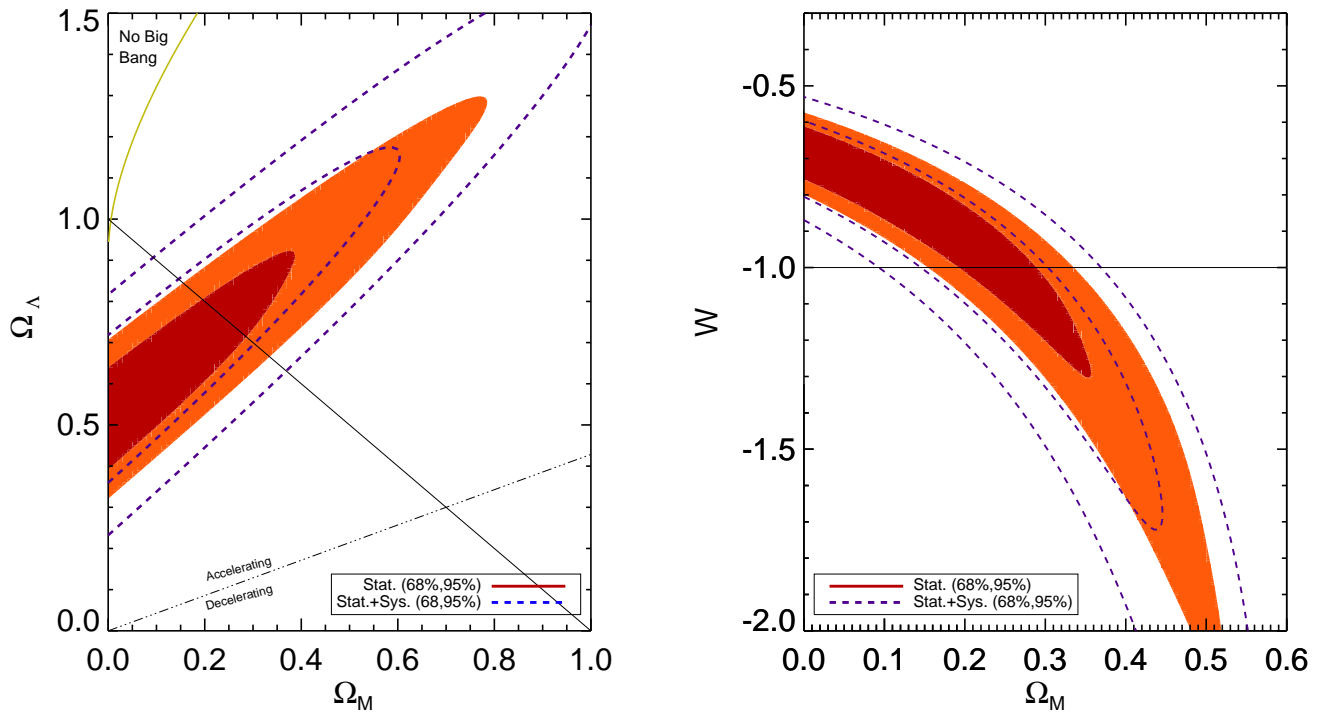
Figure 15. The 1σ and 2σ cosmological constraints using the PS1-lz SN sample only. The statistical constraints as well as when statistical and systematic uncertainties are combined are shown with the solid red and dashed blue lines, respectively. *Left:* Constraints on Ω_M and Ω_Λ assuming a cosmological constant ($w = -1$). *Right:* Constraints on Ω_M and w assuming a constant dark energy equation of state and flatness.

Table 6
BAO data vector

Parameter	Value	Survey	Source
$D_V(0.106)$	457 ± 27 Mpc	6dF	Beutler et al. (2011)
$r_s/D_V(0.20)$	0.1905 ± 0.0061	SDSS	Percival et al. (2010)
$A(0.44)$	0.474 ± 0.034	WiggleZ	Blake et al. (2011)
$A(0.60)$	0.442 ± 0.020	WiggleZ	Blake et al. (2011)
$A(0.73)$	0.424 ± 0.021	WiggleZ	Blake et al. (2011)
$D_V(0.35)/r_s$	8.88 ± 0.17	SDSS(R)	Padmanabhan (2012)
$D_V(0.57)/r_s$	13.67 ± 0.22	BOSS	Anderson et al. (2012)

Note. — BAO data vector from the different surveys used for the cosmological analysis. Markov chains for these constraints are taken from the Planck data release (Planck Collaboration et al. 2013).

For the Hubble constraint, we follow Riess et al. (2011) which uses *HST* observations of Cepheid variables in the host galaxies of eight SNe Ia to calibrate the supernova magnitude-redshift relation. Their best estimate of the Hubble constant is $H_0 = 73.8 \pm 2.4 \ \mathrm{km\,s^{-1}\,Mpc^{-1}}$.

8.4. *Cosmological Parameter Constraints*

Using the set of distances and redshifts for the PS1+lz sample, we are able to constrain possible cosmological models. First, we assume a ΛCDM model ($w = -1$) and measure constraints on Ω_M and Ω_Λ. Using only the PS1+lz sample and assuming flatness, we find $\Omega_M = 0.226^{+0.057}_{-0.061}$ and $\Omega_\Lambda = 0.774^{+0.057}_{-0.061}$ including systematic uncertainties. We present confidence contours for these parameters in the left panel of Figure 15. The evidence for dark energy when not assuming a flat universe, from the SN only sample, is 99.999% when including all systematic uncertainties. We also combine the SN constraints with BAO, CMB, and H_0 constraints to find values of $\Omega_M = 0.308^{+0.033}_{-0.030}$ and $\Omega_\Lambda = 0.693^{+0.024}_{-0.025}$ (See left panel of Figure 16). We summarize our constraints for Ω_M and Ω_Λ under these different assumptions in Table 7.

Table 7
Constraints on Ω_M and w

	Stat Only		Stat+Sys	
	Ω_M	Ω_Λ	Ω_M	Ω_Λ
PS1-lz only (flat Universe)	$0.242^{+0.039}_{-0.041}$	$0.758^{+0.039}_{-0.041}$	$0.226^{+0.057}_{-0.061}$	$0.774^{+0.057}_{-0.061}$
PS1-lz+PL+BAO+H_0	$0.274^{+0.018}_{-0.015}$	$0.722^{+0.014}_{-0.014}$	$0.308^{+0.033}_{-0.030}$	$0.693^{+0.024}_{-0.025}$

Note. — Constraints on Ω_M and Ω_Λ assuming a ΛCDM model ($w = -1$) with statistical only and systematic + statistical uncertainties. For the PS1-lz only sample, the constraints on Ω_M are not significant, we therefore present the constraints assuming flatness.

Table 8
Constraints on Ω_M and w

	Stat Only		Stat+Sys	
	Ω_M	w	Ω_M	w
PS1-lz only	$0.223^{+0.209}_{-0.221}$	$-1.010^{+0.360}_{-0.206}$	$0.256^{+0.201}_{-0.174}$	$-1.120^{+0.450}_{-0.357}$
PS1-lz+PL+BAO+H_0	$0.284^{+0.010}_{-0.010}$	$-1.131^{+0.049}_{-0.049}$	$0.280^{+0.013}_{-0.012}$	$-1.166^{+0.072}_{-0.069}$

Note. — Constraints on Ω_M and w assuming a flat universe with statistical only and systematic + statistical uncertainties.

Relaxing the assumption of a cosmological constant, we can attempt to measure w, the dark energy equation-of-state parameter. For these wCDM models, we assume a flat Universe ($\Omega_k = 0$). With only the PS1+lz SN sample, we measure $w = -1.120^{+0.360}_{-0.206}(\mathrm{Stat})^{+0.269}_{-0.291}(\mathrm{Sys})$ (see right panel of Figure 15). We also combine the SN constraints with CMB, BAO and H_0 constraints to determine $\Omega_M = 0.280^{+0.013}_{-0.012}$ and $w = -1.166^{+0.072}_{-0.069}$ (see right panel of Figure 16). The first number represents the mean, and the uncertainties represent the distance between the mean and the 1σ limits. This formalism is similar to what Planck Collaboration et al. (2013) uses in its Markov-Chain release.

In Table 8 and 9, we compare how the different cosmological probes impact the constraints on Ω_M and w. As shown in Figure 16, the constraints of PL+BAO+H_0 is within the 2σ of our SN-only constraints. Using the *Planck* measurements alone leads to a very low value of $w = -1.485$, albeit still within 2σ of -1 due to its uncertainties of 0.253. Planck Collaboration et al. (2013) claim that there is significant tension between their measurements and measurements of H_0 and/or SNe (SNLS3), but not with the BAO measurements. We show in Table 9 that BAO, H_0 and SN measurements all have a similar pull toward a cosmological constant when combined with *Planck*. When combining our PS1+lz measurements with *Planck*, BAO, and H_0, we find $w = -1.166^{+0.072}_{-0.069}$ inconsistent with -1 at the 2.3σ level. We note that this is very similar to the 2.6σ inconsistency found when substituting SNLS3 for PS1+lz (see Table 18.27[27] in Planck Collaboration et al. 2013). It is important to point out that a tension with a cosmological constant is greatest when H_0 and Planck constraints only are used. S14 analyzes the tension between SN and the CMB using *WMAP* (Hinshaw et al. 2013) instead of

[27] http:www.sciops.esa.int/SYS/WIKI/uploads/Planck_Public_PLA/9/9b/Grid_limit68.pdf
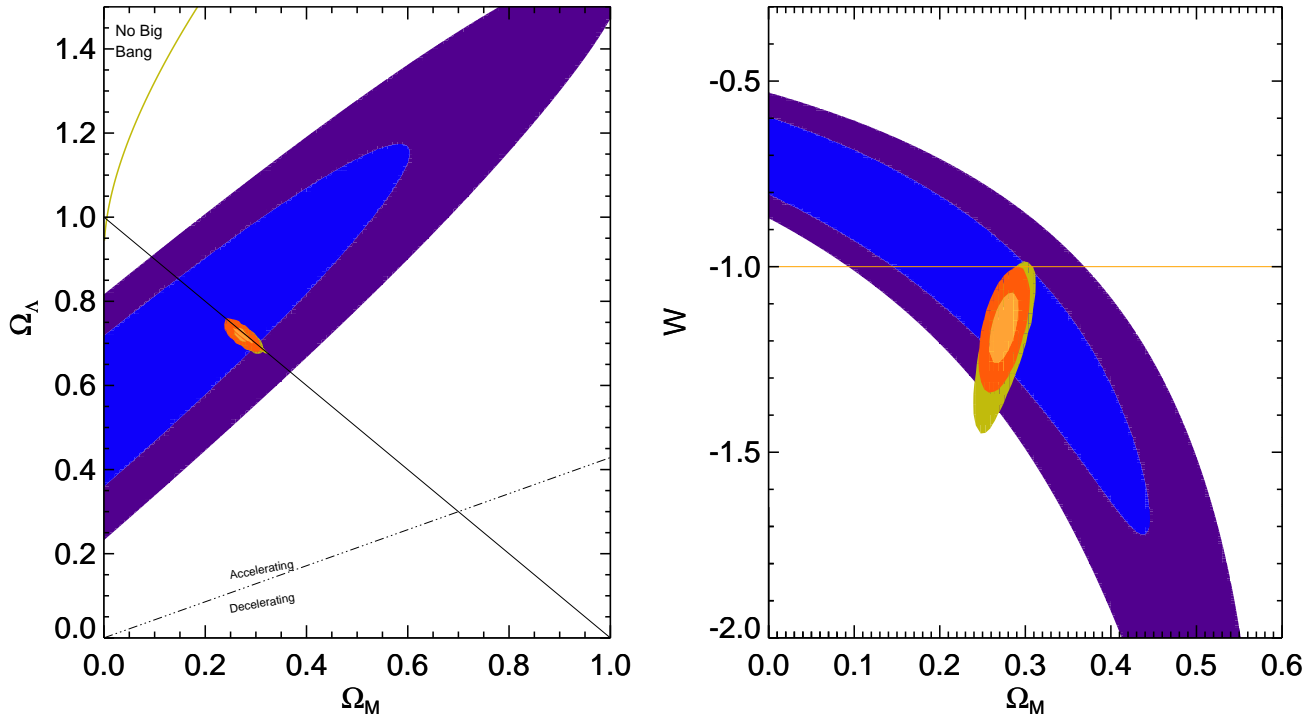
Figure 16. The 68% and 95% cosmological constraints using PS1-lz, *Planck*, BAO and H_0 measurements. Here the statistical and systematic uncertainties are propagated. *Left:* Constraints on Ω_M and Ω_Λ assuming a cosmological constant ($w = -1$). *Right:* Constraints on Ω_M and w assuming a constant dark energy equation of state and flatness.

Planck, and finds the tension to be smaller.

Table 9
Cosmological Parameter Constraints Using different Cosmological Probe
Combinations

Sample	Without PS1-lz		With PS1-lz (Stat. only)		With PS1-lz (Sys. & Stat.)	
	Ω_M	w	Ω_M	w	Ω_M	w
PL	$0.218^{+0.023}_{-0.079}$	$-1.485^{+0.253}_{-0.426}$	$0.289^{+0.015}_{-0.019}$	$-1.102^{+0.058}_{-0.061}$	$0.281^{+0.018}_{-0.022}$	$-1.136^{+0.077}_{-0.079}$
PL+BAO	$0.287^{+0.021}_{-0.020}$	$-1.133^{+0.138}_{-0.104}$	$0.291^{+0.010}_{-0.012}$	$-1.102^{+0.055}_{-0.058}$	$0.288^{+0.014}_{-0.014}$	$-1.124^{+0.077}_{-0.066}$
PL+H_0	$0.258^{+0.016}_{-0.021}$	$-1.240^{+0.095}_{-0.093}$	$0.277^{+0.011}_{-0.015}$	$-1.131^{+0.044}_{-0.052}$	$0.269^{+0.016}_{-0.015}$	$-1.174^{+0.064}_{-0.059}$
PL+BAO+H_0	$0.275^{+0.014}_{-0.014}$	$-1.205^{+0.102}_{-0.087}$	$0.284^{+0.010}_{-0.010}$	$-1.131^{+0.049}_{-0.049}$	$0.280^{+0.013}_{-0.012}$	$-1.166^{+0.072}_{-0.069}$

Note. — Comparison of the Ω_M and w constraints using different variations of external constraints *Planck* (Planck Collaboration et al. 2013), BAO, and H_0 (Riess et al. 2011).

SNe Ia. After correcting for biases related to detection and spectroscopic follow-up efficiency, we used these SNe to constrain cosmological parameters.

9. DISCUSSION

Using the first 1.5 years of the Pan-STARRS1 MDF survey, we have discovered thousands of transients, 146 of which we have spectroscopically confirmed to be SNe Ia. Combining novel calibration techniques with a well-tested photometric data reduction pipeline, we have obtained precise photometry for these SNe. We estimate that the photometric uncertainty is 1.2%, excluding the uncertainty in the *HST* Calspec definition of the AB system. Using the SALT2 light-curve fitter, we have measured distances to a carefully selected sample of 113

9.1. *Comparison to Previous Work*

For our cosmological analysis, we used very recent constraints coming from BAO and CMB experiments. Previous SN analyses did not have access to those data, and thus a direct comparison is more difficult. Similarly, our low-redshift sample is larger than previous compilations, again, complicating any comparison. Nonetheless, we report previous results in an attempt to place the current Pan-STARRS1 analysis in context.

The ESSENCE survey, using 60 high-redshift SNe Ia, 45 low-redshift SNe Ia, and the initial SDSS BAO re-

sults (Eisenstein et al. 2005), found $w = -1.05$ with statistical and systematic uncertainties on the order of 13% (Wood-Vasey et al. 2007). The SDSS-II SN survey, using 103 high-redshift SNe Ia, 33 low-redshift SNe Ia, WMAP5, and the initial SDSS BAO results, found $w = -0.92 \pm 0.13$ (stat) (Kessler et al. 2009a). From combinations with SNLS and *HST* SNe (resulting in 288 total SNe Ia), their constraints decreased to $w = -0.96 \pm 0.06(\text{stat}) \pm 0.12(\text{sys})$. The 3-year SNLS analysis used a combined sample of 242 high-redshift SNe Ia from SNLS, 93 SDSS, 14 *HST*, and 132 low-redshift SNe Ia (a total of 472 SNe), and when combined with the initial SDSS BAO results, WMAP5, and the H_0 constraint, they find $w = -1.061$ with both statistical and systematic uncertainties on the order of 5% (Conley et al. 2011; Sullivan et al. 2011). The Pan-STARRS1 cosmological constraints are derived using the most recent external constraints from *Planck*, the Wiggle-Z BAO results, and the H_0 constraint. Combining these external constraints with 113 high-redshift Pan-STARRS1 SNe Ia and 222 light curves from 197 low-redshift SNe Ia, we find $w = -1.166^{+0.072}_{-0.069}$, inconsistent with -1 at the 2.3σ level. It is currently still unclear whether the tension with flat ΛCDM is a feature of the model or a combination of chance and systematic errors.

All the other SN Ia surveys of the past decade constrain w to the cosmological constant value of -1 within 1σ. An outside observer might expect 1/3 of the results to lie outside this bound, and a confirmation bias could be in effect (Croft & Dailey 2011). Superficially these may appear to be independent tests, providing mounting evidence for a $w = -1$ universe. However, there is significant overlap in the low-redshift SN data used in all analyses, and we should thus expect some degree of correlation in the results. Furthermore, most SN surveys also share the same calibration sources.

9.2. *Future Improvements to Photometric Calibration*

Our systematic uncertainties are dominated by the photometric calibration. Although our calibration effort is sufficient for our current analysis and comparable to other SN surveys, there are additional areas in which significant improvements can be made. Here, we identify areas for future improvement.

Since photometric calibration is currently the largest component of the systematic error budget, it should be the primary focus for future efforts. In order to reduce the systematic uncertainty of the calibration to the level of other systematic uncertainties, photometric accuracy must be significantly better than 1%. For the current Pan-STARRS1 photometric system, all indications are that we have an accuracy of 1.2% before accounting for the *HST* Calspec uncertainty in the AB magnitude system. Over the coming years, we expect that the NIST-based tunable laser system will continue to improve, resulting in decreased ghosting and a more uniform illumination of the flat-field screen. The Pan-STARRS1 photometry is also still improving through changes in reduction software and the acquisition of new data (which will continue until early in 2014 for the MDF survey).

Recently, the SNLS and SDSS teams have undertaken an effort to precisely calibrate their photometric systems onto roughly a single system. They have reached a 0.5% consistency between their photometric

systems, using methods similar to those employed in the Pan-STARRS1 analysis. Specifically, they used observations of the *HST* Calspec standard stars in both systems to provide consistency. An attempt of this analysis is done by S14, which finds discrepencies of up to 2% between the Pan-STARRS1 and SDSS AB systems. The large overlap between the SDSS photometric footprint and the Pan-STARRS1 3π survey has already been used in an übercalibration of the Pan-STARRS1 system (Schlafly et al. 2012). This type of analysis can provide further improvement. In addition, the ongoing *HST* program GO-12967 measures fluxes of DA white dwarf stars, one of which resides within a Pan-STARRS1 MDF. This will allow an in situ direct comparision of white dwarf colors with models that incorporate $\log(g)$ and temperature from ground-based spectroscopy.

We believe that we can also improve our estimation of flux uncertainties. Specifically, we know that there is a tail to the reduced χ^2 distribution shown in Figure 7 to large χ^2. We have shown that these outliers are SNe close to bright objects (usually a host galaxy nucleus), resulting in an underestimate of the uncertainty. We have performed preliminary tests that indicate that modeling the uncertainties with an additional term proportional to the distance to the nearest bright static object will remove this tail and provide a better estimate of the uncertainty. Only a small fraction of SNe are significantly affected by this bias, so it does not affect our current results, but should become more important as we reduce other systematic uncertainties.

9.3. *Improvements to Cosmological Constraints*

The data presented here comprises the first 1.5 years of Pan-STARRS1. As is common with large projects, the data quality and cadence at the beginning of the survey were not as good as those achieved later in the survey. We expect that typical light curve coverage and SNR for the full Pan-STARRS1 sample will be better than in the current sample. At the end of the survey, the total exposure time for the MDF survey will exceed the exposure time of the current sample by nearly a factor of three. In addition, our spectroscopic follow-up efficiency has increased; we expect a final spectroscopic sample will consist of $\gtrsim 400$ SN Ia. Thus we can expect that our current statistical uncertainties will improve by a factor of ~ 2, comparable to the best statistical uncertainties currently reported.

Along with the large spectroscopic sample, we will observe several times as many SNe Ia without spectra. We can generate a large photometrically classified sample of SNe Ia with relatively small contamination from other SN classes (Sako et al. 2011). The SDSS-II supernova survey produced such a sample consisting of 752 photometrically classified SNe Ia and produced cosmological constraints with this sample (Campbell et al. 2013). Combining distance estimates of these SNe (and no other data sets, i.e., no low-redshift SNe) with constraints on H_0, data from *WMAP*, and large scale structure measurements, they find constraints on w with statistical uncertainties of 10%.

The advantage of this method is that the sample size is not limited by the availability of spectroscopic follow-up resources, which has not scaled with the number of SNe discovered. Pan-STARRS1 has discovered $\gtrsim 4500$ tran-

sients with SN-like light curves. This number will likely increase to $\gtrsim$6000 by the end of the Pan-STARRS1 survey. In magnitude-limited surveys like Pan-STARRS1, 79% of all SNe are SN Ia (Li et al. 2011), thus with a classification efficiency of 70%, we can expect $\sim$3300 photometrically classified SNe Ia from the Pan-STARRS1 survey.

The photometric classification of a transient is significantly improved with a host-galaxy spectroscopic redshift, which can be obtained after the SN has faded. Follow-up observations at the end of the survey with a large FOV multi-object spectrograph such as Hectospec on the MMT should provide redshifts for the vast majority of candidate SNe Ia (Jones et al. 2014).

With this large set of new SNe Ia, more work can be done to identify a "third parameter" that correlates with luminosity independent of light curve shape and color. This would be particularly important if there is some redshift-dependent evolution of the SN Ia properties. Candidates are, for example, ejecta velocity (Wang et al. 2009; Foley & Kasen 2011; Foley et al. 2011), other spectral features (Foley et al. 2008; Bailey et al. 2009; Blondin et al. 2011; Silverman et al. 2012b; Foley & Kirshner 2013), and host galaxy properties (Kelly et al. 2010; Lampeitl et al. 2010; Sullivan et al. 2010; Hayden et al. 2012).

We are also conducting a large (100-orbit) *HST* program, RAISIN (GO-13046; PI Kirshner) to obtain restframe NIR photometry of Pan-STARRS1 SNe Ia ($0.2 < z < 0.4$). Although calibration is currently the largest systematic uncertainty in our analysis, the largest astrophysical systematic uncertainty comes from the treatment of intrinsic SN colors and dust reddening, which directly affects distance measurements. When combining the *HST* and Pan-STARRS1 photometry, the large wavelength range (from UV to NIR) provides additional constraints on the reddening law, which should significantly improve our understanding of systematics related to dust extinction, reddening, and SN Ia colors. SN Ia are more nearly standard candles when observed in restframe near-infrared bands and extinction is significantly lower at these wavelengths (Krisciunas et al. 2004; Wood-Vasey et al. 2008; Mandel et al. 2009; Folatelli et al. 2010; Barone-Nugent et al. 2012; Kattner et al. 2012). The systematic errors that result from lightcurve shape corrections and inferences about extinction from color are distinctly smaller when using these bands (Mandel et al. 2011).

10. CONCLUSION

We have presented the light curves and analysis of 146 spectroscopically confirmed SNe Ia from the first 1.5 years of the Pan-STARRS1 Medium Deep Survey. We have described the SN discovery and spectroscopic follow-up of the survey. We analyze the relative and absolute photometric calibration in the Pan-STARRS1 natural system using on-site measurements of the instrument response function, spectro-photometric standard star observations, and übercalibration, with an emphasis on any systematic biases introduced. We find that the systematic uncertainties in the photometric calibration are currently 1.2% without accounting for the uncertainty in the *HST* Calspec definition of the AB system.

From the sample of 146 SNe Ia in the redshift range $0.03 < z < 0.65$, 113 passed the various quality cuts in our cosmological analysis. The spectral information and SALT2 light curve fit parameters of each SN are presented so that this sample can be used in joint analyses with other supernova samples. When combining the Pan-STARRS1 sample with low-z SNe Ia (113 PS1 SNe Ia + 222 light curves from 197 low-z SNe Ia), we find $w = -1.120^{+0.450}_{-0.357}$ assuming a flat Universe. A Universe devoid of Dark Energy is rejected at the at 99.999% level with the SN sample alone including all identified systematics. When combined with external constraints (BAO, CMB, and H_0), our cosmological analysis yields $\Omega_M = 0.280^{+0.013}_{-0.012}$ and $w = -1.166^{+0.072}_{-0.069}$ including all identified systematics, consistent with a cosmological constant. This is in agreement with the results from previous SN Ia surveys like SNLS and SDSS. We show the pull on the recovered cosmological parameters from the SN measurements. Compared to when CMB, BAO and H_0 measurements are used to constrain w, including the SN measurements reduces the total uncertainty in w by $\sim 40\%$.

Further analysis of the systematic errors of this sample is presented in the companion paper by S14. In the future analysis of the full 4-year Pan-STARRS1 sample, we can reduce the dominant systematic uncertainty in absolute photometric calibration with more Pan-STARRS1 observations, additional Calspec spectrophotometric standards, and improved reduction and analysis.

This paper and the companion paper by S14 represent the first in a series of cosmological analysis using the PS1 sample. It is necessary to accurately measure SN photometry and quantify systematic uncertainties with the spectroscopically confirmed sample before doing so for the much larger photometric sample. The photometric sample is currently $> 5\times$ bigger than any published spectroscopic sample of SN Ia and will represent a significant step forward for constraining the nature of dark energy.

Table 10
Pan-STARRS1 Spectroscopic Sample

PS1 name	Spectra MJD's	Telescopes	z_{hel}
PS1-0909006	55098	Gem-N	0.284(0.001)
PS1-0909010	55105	Gem-N	0.270(0.010)
PS1-0910012	55116,55118,55121,55142	Gem-S,NOT,Magellan,Gem-S	0.079(0.001)
PS1-0910016	55125	Gem-N	0.230(0.010)
PS1-0910017	55125	Gem-N	0.320(0.010)
PS1-0910018	55125	Gem-N	0.265(0.001)
PS1-0910020	55124	Gem-S	0.242(0.001)
PS1-0910021	55125	Gem-S	0.256(0.001)

Table 10 — *Continued*

PS1 name	Spectra MJD's	Telescopes	z_{hel}
PS1-10c	55213	Gem-N	0.152(0.001)
PS1-10d	55216	Magellan	0.231(0.001)
PS1-10e	55217	Magellan	0.245(0.001)
PS1-10f	55214	Gem-S	0.380(0.010)
PS1-10g	55217	Magellan	0.137(0.001)
PS1-10h	55215,55527	Magellan,MMT	0.250(0.010)
PS1-10i	55217	Magellan	0.150(0.001)
PS1-10j	55216,55249,55293	Gem-N,MMT,MMT	0.436(0.001)
PS1-10k	55216	Magellan	0.340(0.001)
PS1-10l	55216	Magellan	0.370(0.001)
PS1-10m	55216,55297	Gem-S,MMT	0.618(0.001)
PS1-10n	55217	Magellan	0.460(0.001)
PS1-10o	55216	Magellan	0.220(0.001)
PS1-10p	55217	Magellan	0.310(0.001)
PS1-10r	55251	MMT	0.118(0.001)
PS1-10s	55221	Gem-S	0.101(0.001)
PS1-10u	55217	NOT	0.183(0.001)
PS1-10v	55247	WHT	0.098(0.001)
PS1-10w	55244	FLWO	0.031(0.001)
PS1-10z	55250	WHT	0.140(0.001)
PS1-10af	55233,55268	NOT,Gem-N	0.244(0.001)
PS1-10ag	55263	NOT	0.081(0.001)
PS1-10aj	55233	Gem-N	0.195(0.001)
PS1-10ht	55290	MMT	0.260(0.010)
PS1-10hu	55288	WHT	0.126(0.001)
PS1-10ia	55295	Keck	0.409(0.001)
PS1-10if	55288,55297	WHT,MMT	0.150(0.001)
PS1-10ig	55290	MMT	0.260(0.001)
PS1-10ik	55293	MMT	0.230(0.001)
PS1-10im	55293	MMT	0.510(0.001)
PS1-10io	55319	WHT	0.220(0.001)
PS1-10ir	55355	WHT	0.250(0.001)
PS1-10iv	55330	Gem-N	0.369(0.001)
PS1-10iw	55331	Gem-N	0.447(0.001)
PS1-10ix	55330	Gem-N	0.381(0.001)
PS1-10iy	55331	Gem-N	0.443(0.001)
PS1-10ji	55363	MMT	0.231(0.001)
PS1-10jk	55363	MMT	0.430(0.001)
PS1-10jl	55363	MMT	0.530(0.001)
PS1-10jo	55364	MMT	0.241(0.001)
PS1-10jp	55364	MMT	0.387(0.001)
PS1-10jq	55364	MMT	0.459(0.001)
PS1-10jt	55364	MMT	0.336(0.001)
PS1-10ju	55364	MMT	0.323(0.001)
PS1-10jv	55364	MMT	0.360(0.001)
PS1-10jw	55364	MMT	0.360(0.001)
PS1-10jz	55365	MMT	0.550(0.001)
PS1-10kc	55365	MMT	0.347(0.001)
PS1-10kd	55365	MMT	0.331(0.001)
PS1-10kf	55365	MMT	0.450(0.001)
PS1-10kg	55365	MMT	0.420(0.010)
PS1-10ki	55365	MMT	0.379(0.001)
PS1-10kj	55365	MMT	0.350(0.010)
PS1-10kl	55365	MMT	0.443(0.001)
PS1-10kv	55384	Gem-N	0.530(0.001)
PS1-10nq	55351,55355	UH88,WHT	0.035(0.001)
PS1-10nu	55422	Magellan	0.065(0.001)
PS1-10acx	55288	MMT	0.350(0.001)
PS1-10aeq	55475	APO	0.066(0.001)
PS1-10afu	55473	MMT	0.338(0.001)
PS1-10agw	55471	MMT	0.330(0.010)
PS1-10ahk	55479	MMT	0.431(0.001)
PS1-10ahl	55471	MMT	0.635(0.001)
PS1-10axm	55485	Gem-N	0.510(0.010)
PS1-10axx	55487	MMT	0.027(0.001)
PS1-10ayb	55514	MMT	0.140(0.001)
PS1-10bhe	55487	MMT	0.145(0.001)
PS1-10bji	55514	MMT	0.148(0.001)
PS1-10bjn	55528	MMT	0.290(0.010)
PS1-10bjz	55540	MMT	0.310(0.010)
PS1-10bka	55507	Gem-N	0.247(0.001)
PS1-10bkf	55539	MMT	0.172(0.001)
PS1-10bki	55539	MMT	0.430(0.001)
PS1-10blh	55539	MMT	0.319(0.001)
PS1-10blp	55515,55540	MMT,MMT	0.217(0.001)

Table 10 — *Continued*

PS1 name	Spectra MJD's	Telescopes	z_{hel}
PS1-10bls	55540	MMT	0.276(0.001)
PS1-10bmb	55539	MMT	0.360(0.010)
PS1-10bmk	55539	MMT	0.103(0.001)
PS1-10byj	55547	Gem-N	0.511(0.001)
PS1-10byn	55540	MMT	0.179(0.001)
PS1-10byo	55558	MMT	0.290(0.001)
PS1-10byq	55539	MMT	0.210(0.010)
PS1-10byr	55540	MMT	0.240(0.010)
PS1-10bys	55540	MMT	0.203(0.001)
PS1-10bzo	55558	MMT	0.380(0.001)
PS1-10bzp	55559	MMT	0.540(0.001)
PS1-10bzt	55558	MMT	0.420(0.001)
PS1-10bzu	55558	MMT	0.350(0.001)
PS1-10bzy	55558	MMT	0.200(0.001)
PS1-10cad	55558	MMT	0.270(0.010)
PS1-10cay	55558	MMT	0.250(0.010)
PS1-10cbb	55559	MMT	0.220(0.010)
PS1-10cbu	55570	MMT	0.400(0.001)
PS1-11e	55570	MMT	0.320(0.001)
PS1-11p	55573	Magellan	0.480(0.001)
PS1-11s	55573	Magellan	0.400(0.001)
PS1-11t	55573	Magellan	0.450(0.001)
PS1-11w	55571	MMT	0.174(0.001)
PS1-11aj	55571	MMT	0.106(0.001)
PS1-11ao	55570	MMT	0.336(0.001)
PS1-11at	55570	MMT	0.320(0.001)
PS1-11bg	55590	Magellan	0.329(0.001)
PS1-11bh	55573	Magellan	0.350(0.001)
PS1-11bk	55592	Magellan	0.160(0.001)
PS1-11br	55586	Gem-S	0.300(0.010)
PS1-11cn	55592	Gem-N	0.250(0.010)
PS1-11co	55591	Gem-S	0.230(0.010)
PS1-11fi	55614	MMT	0.082(0.001)
PS1-11gh	55626	Magellan	0.220(0.010)
PS1-11gr	55617	APO	0.105(0.001)
PS1-11iv	55615	MMT	0.293(0.001)
PS1-11jo	55615	MMT	0.330(0.001)
PS1-11kk	55615	MMT	0.300(0.010)
PS1-11mq	55656,55687	MMT;MMT	0.210(0.001)
PS1-11mz	55651	APO	0.101(0.001)
PS1-11sk	55687	MMT	0.270(0.001)
PS1-11um	55687	MMT	0.064(0.001)
PS1-11uo	55687	MMT	0.310(0.001)
PS1-11uw	55687	MMT	0.300(0.001)
PS1-11vb	55687	MMT	0.230(0.010)
PS1-11wv	55684	APO	0.132(0.001)
PS1-11xc	55716	MMT	0.328(0.001)
PS1-11xw	55723	MMT	0.270(0.001)
PS1-11yj	55717	MMT	0.107(0.001)
PS1-11yr	55723	Gem-N	0.530(0.001)
PS1-11yu	55716	MMT	0.360(0.010)
PS1-11zd	55716	MMT	0.100(0.001)
PS1-11zg	55721	MMT	0.370(0.001)
PS1-11zu	55717	MMT	0.360(0.001)
PS1-11zv	55717	MMT	0.350(0.001)
PS1-11zw	55717	MMT	0.423(0.001)
PS1-11aaw	55717	MMT	0.510(0.010)
PS1-11abm	55745	Gem-N	0.320(0.001)
PS1-11aea	55744	Gem-N	0.300(0.001)
PS1-11aij	55769	Gem-N	0.510(0.001)
PS1-11ajs	55808	MMT	0.230(0.010)
PS1-11ala	55808	MMT	0.370(0.010)
PS1-11alv	55807	MMT	0.145(0.001)
PS1-11ams	55803	Magellan	0.140(0.001)

Note. — Spectroscopic information for all spectroscopically classified Pan-STARRS1 SN Ia from 2009 September to 2011 May.

Table 11
Properties of the Pan-STARRS1 Spectroscopic Sample

PS1 name	R.A. (J2000)	Dec. (J2000)	MDF	t_{disc}	Cut
PS1-0909006	22:15:48.000	01:11:05.39	09	55083	$\cdots$
PS1-0909010	02:28:28.368	-04:04:44.08	01	55089	$|x_1| > 3.0$
PS1-0910012	03:29:53.232	-28:05:12.12	02	55096	Iax
PS1-0910016	02:21:13.752	-03:54:35.82	01	55104	$|x_1| > 3.0$
PS1-0910017	02:21:06.600	-05:01:23.84	01	55104	$\cdots$
PS1-0910018	02:22:40.080	-04:01:38.32	01	55104	$\cdots$
PS1-0910020	03:38:23.400	-28:15:11.88	02	55104	LC incomplete
PS1-0910021	03:34:28.800	-27:54:30.24	02	55104	LC incomplete
PS1-10c	08:37:18.937	44:20:01.44	03	55207	$\cdots$
PS1-10d	03:33:27.948	-28:22:17.48	02	55207	$\cdots$
PS1-10e	09:58:59.758	03:09:27.11	04	55208	$\cdots$
PS1-10f	09:59:54.221	02:24:42.84	04	55208	Close To Center
PS1-10g	02:23:30.711	-04:38:10.76	01	55206	$\cdots$
PS1-10h	02:24:15.945	-03:11:11.53	01	55206	$\cdots$
PS1-10i	02:20:22.959	-04:40:21.03	01	55206	$\cdots$
PS1-10j	10:49:14.220	58:28:02.04	05	55212	$\cdots$
PS1-10k	10:00:27.616	02:41:38.52	04	55212	$\cdots$
PS1-10l	10:04:55.536	02:35:27.31	04	55212	$\cdots$
PS1-10m	10:02:09.393	01:53:57.01	04	55212	$\cdots$
PS1-10n	10:03:14.385	03:08:39.21	04	55212	$\cdots$
PS1-10o	10:02:08.822	02:43:06.83	04	55214	$\cdots$
PS1-10p	09:59:16.802	01:36:48.55	04	55216	$\cdots$
PS1-10r	10:44:38.225	57:48:40.04	05	55212	$\cdots$
PS1-10s	09:55:57.231	02:15:48.47	04	55212	LC incomplete
PS1-10u	02:19:46.554	-03:12:10.47	01	55215	fit not converged
PS1-10v	10:03:26.078	01:01:45.91	04	55240	$\cdots$
PS1-10w	10:42:41.887	58:50:37.77	05	55240	$\cdots$
PS1-10z	08:36:12.605	44:00:25.52	03	55240	$\cdots$
PS1-10af	10:48:07.061	56:51:00.54	05	55212	$\cdots$
PS1-10ag	10:57:41.331	57:36:48.36	05	55251	LC incomplete
PS1-10aj	08:46:19.241	44:04:22.97	03	55214	$\cdots$
PS1-10ht	08:46:50.687	45:29:31.33	03	55275	LC incomplete
PS1-10hu	12:25:20.676	46:00:54.75	06	55275	$\cdots$
PS1-10ia	14:11:31.058	53:34:46.48	07	55275	$\cdots$
PS1-10if	10:00:21.196	01:25:05.25	04	55275	$\cdots$
PS1-10ig	14:07:26.975	53:20:34.49	07	55275	$\cdots$
PS1-10ik	10:45:15.388	58:11:33.76	05	55275	$\cdots$
PS1-10im	10:50:05.881	58:46:38.71	05	55288	$\cdots$
PS1-10io	10:00:44.015	03:24:14.31	04	55298	$\cdots$
PS1-10ir	10:45:09.371	58:33:16.64	05	55326	$\cdots$
PS1-10iv	10:02:00.450	02:03:37.82	04	55320	LC incomplete
PS1-10iw	14:17:50.504	52:48:03.77	07	55326	$\cdots$
PS1-10ix	10:48:23.471	57:08:53.54	05	55326	$\cdots$
PS1-10iy	14:16:28.707	54:03:12.82	07	55326	$\cdots$
PS1-10ji	16:14:28.674	54:43:32.92	08	55347	$\cdots$
PS1-10jk	16:08:52.639	55:00:17.32	08	55348	$\cdots$
PS1-10jl	14:07:14.923	53:59:51.40	07	55348	$\cdots$
PS1-10jo	12:16:41.554	46:41:24.09	06	55353	LC incomplete
PS1-10jp	14:17:18.567	53:58:41.96	07	55353	$\cdots$
PS1-10jq	12:21:46.461	46:39:13.16	06	55363	LC incomplete
PS1-10jt	16:08:18.409	54:54:29.34	08	55347	$\cdots$
PS1-10ju	16:18:15.872	55:23:04.95	08	55353	$\cdots$
PS1-10jv	16:17:47.706	55:18:08.24	08	55353	$\cdots$
PS1-10jw	16:13:48.215	55:36:30.73	08	55353	$\cdots$
PS1-10jz	16:06:48.805	54:58:51.36	08	55353	$\cdots$
PS1-10kc	16:18:53.807	55:46:58.47	08	55353	$\cdots$
PS1-10kd	16:05:44.832	56:04:27.90	08	55353	$\cdots$
PS1-10kf	14:11:57.770	52:04:18.65	07	55362	$\cdots$
PS1-10kg	16:01:15.410	54:17:53.54	08	55362	LC incomplete
PS1-10ki	12:21:59.469	45:50:49.80	06	55362	LC incomplete
PS1-10kj	12:14:06.504	46:59:32.29	06	55362	LC incomplete
PS1-10kl	14:14:03.340	53:21:43.87	07	55362	$\cdots$
PS1-10kv	14:10:39.353	53:59:22.76	07	55353	$\cdots$
PS1-10nq	12:11:33.322	47:16:29.36	06	55344	$\cdots$
PS1-10nu	02:27:12.037	-04:32:04.87	01	55414	$\cdots$
PS1-10acx	16:05:54.089	55:11:52.30	08	55424	$\cdots$
PS1-10aeq	03:29:42.071	-27:52:38.11	02	55442	$\cdots$
PS1-10afu	16:10:40.664	55:55:42.48	08	55446	LC incomplete
PS1-10agw	22:18:29.334	00:56:29.35	09	55449	$\cdots$
PS1-10ahk	02:19:56.728	-03:57:38.18	01	55468	$\cdots$
PS1-10ahl	22:15:29.670	00:32:30.87	09	55468	$\cdots$
PS1-10axm	23:33:18.787	-00:57:02.56	10	55479	$\cdots$
PS1-10axx	08:44:15.659	43:18:28.86	03	55475	$P < 0.001$
PS1-10ayb	03:36:17.301	-28:03:05.44	02	55482	$\cdots$
PS1-10bhe	08:40:03.838	43:25:17.23	03	55475	LC incomplete

Rest, Scolnic et al.

Table 11 — *Continued*

PS1 name	R.A. (J2000)	Dec. (J2000)	MDF	t_{disc}	Cut
PS1-10bji	03:28:29.494	-26:49:42.58	02	55500	$\cdots$
PS1-10bjn	23:27:37.793	-01:45:44.83	10	55493	$\cdots$
PS1-10bjz	23:33:10.781	-01:14:07.02	10	55501	$\cdots$
PS1-10bka	08:46:43.279	44:00:12.56	03	55501	LC incomplete
PS1-10bkf	08:47:18.713	43:24:29.21	03	55502	$\cdots$
PS1-10bki	08:48:33.834	43:59:06.90	03	55502	$\cdots$
PS1-10blh	02:21:46.162	-05:09:05.76	01	55510	$\cdots$
PS1-10blp	03:30:04.362	-28:15:24.09	02	55507	$\cdots$
PS1-10bls	03:32:16.116	-27:11:39.51	02	55507	$\cdots$
PS1-10bmb	23:29:46.670	00:35:25.82	10	55507	$\cdots$
PS1-10bmk	03:34:30.852	-27:19:14.09	02	55524	$\cdots$
PS1-10byj	23:33:31.714	00:08:24.06	10	55536	LC incomplete
PS1-10byn	23:25:47.036	00:23:46.68	10	55536	LC incomplete
PS1-10byo	23:27:55.950	00:20:21.89	10	55536	LC incomplete
PS1-10byq	02:19:36.752	-03:31:45.28	01	55536	$\cdots$
PS1-10byr	22:17:50.801	01:02:33.80	09	55536	$\cdots$
PS1-10bys	22:17:31.025	01:15:19.48	09	55536	fit not converged
PS1-10bzo	08:48:02.754	44:26:57.43	03	55546	$\cdots$
PS1-10bzp	08:40:03.150	44:53:39.61	03	55546	$\cdots$
PS1-10bzt	08:48:59.894	44:51:56.45	03	55546	$\cdots$
PS1-10bzu	08:45:25.506	44:03:36.99	03	55546	$\cdots$
PS1-10bzy	03:35:22.742	-27:50:25.00	02	55546	$\cdots$
PS1-10cad	03:34:19.273	-27:34:08.05	02	55546	$\cdots$
PS1-10cay	03:37:19.804	-26:54:06.29	02	55546	$\cdots$
PS1-10cbb	03:30:51.155	-26:27:35.94	02	55546	$\cdots$
PS1-10cbu	08:44:16.542	45:20:39.13	03	55561	$\cdots$
PS1-11e	08:35:56.591	43:29:40.24	03	55561	$\cdots$
PS1-11p	09:55:10.067	01:43:48.89	04	55566	$\cdots$
PS1-11s	10:03:09.364	02:08:36.19	04	55566	$\cdots$
PS1-11t	10:02:06.281	02:05:16.06	04	55566	$\cdots$
PS1-11w	10:54:43.784	58:37:35.62	05	55566	$\cdots$
PS1-11aj	10:03:16.274	03:28:29.81	04	55567	$\cdots$
PS1-11ao	02:25:44.073	-03:11:46.36	01	55568	$|c| > 0.25$
PS1-11at	10:01:53.027	02:02:33.53	04	55566	$\cdots$
PS1-11bg	10:03:58.861	02:15:44.71	04	55572	$\cdots$
PS1-11bh	09:58:30.828	02:52:18.41	04	55572	$\cdots$
PS1-11bk	09:56:19.761	01:24:34.08	04	55572	$\cdots$
PS1-11br	03:26:43.681	-27:56:10.45	02	55576	$\cdots$
PS1-11cn	02:23:05.634	-03:36:37.25	01	55588	$\cdots$
PS1-11co	03:28:35.272	-27:20:27.48	02	55588	$\cdots$
PS1-11fi	14:12:57.070	52:44:37.19	07	55597	$\cdots$
PS1-11gh	03:38:00.402	-28:00:41.20	02	55597	LC incomplete
PS1-11gr	08:40:55.602	44:47:30.26	03	55597	LC incomplete
PS1-11iv	12:14:55.584	46:34:33.26	06	55597	$\cdots$
PS1-11jo	12:16:00.418	47:55:13.49	06	55597	$\cdots$
PS1-11kk	16:10:49.277	55:15:05.31	08	55602	Initial Cut
PS1-11mq	10:49:34.244	57:36:56.63	05	55633	$\cdots$
PS1-11mz	12:14:57.100	46:50:42.15	06	55633	$\cdots$
PS1-11sk	12:12:50.654	47:08:44.75	06	55666	$\cdots$
PS1-11um	16:14:45.674	56:09:35.89	08	55675	LC incomplete
PS1-11uo	10:45:24.781	57:13:04.41	05	55675	$\cdots$
PS1-11uw	16:04:56.287	54:52:41.30	08	55675	$\cdots$
PS1-11vb	10:05:28.755	01:51:22.09	04	55675	LC incomplete
PS1-11wv	12:20:33.010	46:39:58.14	06	55678	$\cdots$
PS1-11xc	16:15:51.680	54:26:35.56	08	55677	$\cdots$
PS1-11xw	12:19:54.009	48:08:25.00	06	55694	$\cdots$
PS1-11yj	16:08:30.469	53:41:07.17	08	55705	91bg
PS1-11yr	12:26:21.156	46:35:45.33	06	55705	$\cdots$
PS1-11yu	16:12:46.179	54:52:25.40	08	55705	Close To Center
PS1-11zd	14:18:40.107	54:10:59.00	07	55705	$\cdots$
PS1-11zg	10:53:08.049	57:12:04.55	05	55708	$\cdots$
PS1-11zu	16:06:28.184	53:52:18.49	08	55708	$\cdots$
PS1-11zv	16:11:37.152	53:58:12.96	08	55708	$\cdots$
PS1-11zw	16:10:25.814	54:08:58.48	08	55708	$\cdots$
PS1-11aaw	14:11:30.070	52:28:59.63	07	55712	$|x_1| > 3.0$
PS1-11abm	12:24:43.960	47:40:05.32	06	55714	$\cdots$
PS1-11aea	16:14:28.433	54:00:10.88	08	55740	$\cdots$
PS1-11aij	16:17:16.520	55:22:45.97	08	55762	$\cdots$
PS1-11ajs	22:17:50.984	01:28:06.39	09	55770	$\cdots$
PS1-11ala	22:12:19.673	01:02:09.41	09	55782	$\cdots$
PS1-11alv	22:15:52.038	-00:49:30.57	09	55795	$\cdots$
PS1-11ams	22:16:32.270	00:28:23.86	09	55801	Close To Center

Note. — Summary of the general properties of the Pan-STARRS1
SN Ia. The MDF fields are defined in Table 1. The discovery date
t_{disc} is given in MJD. The cuts are explained in §7.2 – Cut 7 − 10 in
§7.2 are referred to as "LC incomplete".

Table 12
Contributions and Cuts of the Different Samples

Set	Total	Final	Initial Cut	First Pass Cut	Fit not conv.	$P < 0.001$	$|x_1| > 3.0$ $|c| > 0.25$	Chauveneut
JRK07	133	49	30	34	1	12	7	0
CFA3	185	85	8	70	0	7	15	0
CFA4	94	43	8	26	3	8	5	1
CSP	85	45	5	13	0	14	7	1
PS1	147	112	10	18	2	1	4	0

Note. — Breakdown of the number of SNe Ia that were cut from the different sets. The different sets are defined in §7.2.

Table 13
Fit Parameters of low-z Sample

SN	Set	z_{cmb}	t_{peak}	P_{fit}	x_1	c	m_B	μ	$E(B-V)$
1990O	JRK07	0.031(0.001)	48076.88(0.59)	0.9960	0.476(0.231)	-0.054(0.036)	15.993(0.065)	35.587(0.166)	0.075(0.012)
1990af	JRK07	0.050(0.001)	48196.03(0.27)	1.0000	-2.114(0.235)	-0.038(0.048)	17.508(0.039)	36.689(0.190)	0.028(0.005)
1992P	JRK07	0.026(0.001)	48719.90(0.50)	0.4810	0.069(0.352)	-0.083(0.045)	15.811(0.036)	35.441(0.195)	0.017(0.003)
1992ae	JRK07	0.075(0.001)	48804.90(0.66)	0.7470	-0.708(0.186)	-0.029(0.055)	18.216(0.052)	37.565(0.199)	0.029(0.005)
1992aq	JRK07	0.101(0.001)	48834.37(0.69)	1.0000	-1.326(0.264)	-0.071(0.063)	19.065(0.053)	38.460(0.215)	0.010(0.002)
1992al	JRK07	0.014(0.001)	48838.84(0.17)	1.0000	-0.222(0.110)	-0.110(0.029)	14.204(0.036)	33.880(0.198)	0.027(0.004)
1992bc	JRK07	0.021(0.001)	48913.16(0.08)	0.3520	0.782(0.100)	-0.121(0.027)	14.847(0.032)	34.700(0.169)	0.018(0.003)
1992bh	JRK07	0.042(0.001)	48921.06(0.57)	0.9960	-0.053(0.182)	0.042(0.047)	17.363(0.038)	36.575(0.188)	0.018(0.003)
1992bl	JRK07	0.042(0.001)	48947.68(0.48)	0.9640	-1.631(0.138)	-0.045(0.051)	17.070(0.050)	36.342(0.196)	0.009(0.001)
1992bp	JRK07	0.079(0.001)	48980.87(0.33)	0.9480	-0.882(0.163)	-0.102(0.052)	18.075(0.049)	37.631(0.194)	0.056(0.009)
1992bs	JRK07	0.063(0.001)	48986.08(0.58)	0.9680	-0.230(0.166)	-0.034(0.049)	18.046(0.045)	37.478(0.185)	0.009(0.001)
1992bo	JRK07	0.019(0.001)	48986.62(0.10)	1.0000	-1.983(0.112)	-0.050(0.031)	15.501(0.036)	34.739(0.177)	0.022(0.003)
1993B	JRK07	0.071(0.001)	49006.04(0.74)	0.0621	-0.395(0.196)	0.069(0.057)	18.265(0.069)	37.345(0.197)	0.064(0.010)
1993H	JRK07	0.025(0.001)	49067.70(0.39)	0.9770	-1.972(0.096)	0.092(0.032)	16.417(0.052)	35.202(0.165)	0.049(0.008)
1993O	JRK07	0.052(0.001)	49134.68(0.16)	0.7920	-0.563(0.138)	-0.077(0.046)	17.383(0.045)	36.905(0.181)	0.043(0.007)
1993ag	JRK07	0.049(0.001)	49317.30(0.33)	0.8030	-0.784(0.154)	0.082(0.051)	17.635(0.067)	36.618(0.192)	0.083(0.013)
1994S	JRK07	0.016(0.001)	49518.66(0.31)	0.5680	0.287(0.229)	-0.082(0.030)	14.504(0.037)	34.160(0.188)	0.017(0.003)
1995ac	JRK07	0.049(0.001)	49993.54(0.17)	0.6400	0.724(0.119)	-0.048(0.028)	16.807(0.037)	36.417(0.149)	0.034(0.005)
1995ak	JRK07	0.022(0.001)	50022.45(0.51)	0.2310	-1.071(0.168)	0.070(0.036)	15.775(0.052)	34.757(0.172)	0.031(0.005)
1996C	JRK07	0.028(0.001)	50129.51(0.47)	0.9300	0.510(0.167)	0.049(0.030)	16.362(0.038)	35.631(0.164)	0.011(0.002)
1996ab	JRK07	0.124(0.001)	50223.37(1.36)	0.8210	0.074(0.436)	-0.179(0.057)	19.291(0.060)	39.231(0.220)	0.026(0.004)
1996bl	JRK07	0.035(0.001)	50377.10(0.24)	0.8580	-0.071(0.153)	-0.002(0.032)	16.472(0.061)	35.822(0.154)	0.074(0.012)
1997E	JRK07	0.013(0.001)	50468.54(0.20)	1.0000	-1.634(0.169)	0.028(0.034)	14.915(0.072)	33.953(0.204)	0.092(0.015)
1997Y	JRK07	0.017(0.001)	50488.76(1.03)	0.9920	-0.930(0.270)	0.001(0.032)	15.080(0.037)	34.302(0.190)	0.014(0.002)
1997dg	JRK07	0.030(0.001)	50721.01(0.44)	0.8980	-0.394(0.225)	-0.020(0.034)	16.618(0.057)	35.982(0.164)	0.063(0.010)
1997do	JRK07	0.011(0.001)	50766.87(0.16)	0.0903	0.244(0.221)	0.070(0.033)	14.103(0.055)	33.269(0.232)	0.051(0.008)
1998V	JRK07	0.017(0.001)	50892.86(0.35)	0.5220	-0.278(0.123)	0.029(0.040)	14.983(0.106)	34.205(0.185)	0.145(0.023)
1998ab	JRK07	0.028(0.001)	50914.77(0.11)	0.0078	0.258(0.127)	0.103(0.030)	15.896(0.036)	34.956(0.160)	0.014(0.002)
1998bp	JRK07	0.011(0.001)	50935.42(0.46)	0.2480	-2.471(0.185)	0.188(0.037)	15.044(0.061)	33.450(0.235)	0.061(0.010)
1998co	JRK07	0.017(0.001)	50987.72(1.81)	0.9980	-2.997(2.869)	0.029(0.060)	15.376(0.098)	34.218(0.410)	0.035(0.006)
1998dx	JRK07	0.054(0.001)	51072.60(0.65)	0.9760	-1.678(0.395)	-0.099(0.040)	17.305(0.054)	36.742(0.168)	0.033(0.005)
1998eg	JRK07	0.024(0.001)	51111.49(0.91)	0.9950	-0.561(0.416)	0.017(0.037)	15.935(0.072)	35.156(0.182)	0.091(0.015)
1998ef	JRK07	0.018(0.001)	51114.24(0.18)	0.9520	-1.048(0.240)	-0.095(0.034)	14.569(0.059)	34.081(0.183)	0.059(0.009)
1999aw	JRK07	0.039(0.001)	51255.11(0.33)	0.2000	2.246(0.179)	-0.084(0.029)	16.490(0.035)	36.427(0.156)	0.026(0.004)
1999cc	JRK07	0.032(0.001)	51315.96(0.28)	1.0000	-1.567(0.152)	-0.011(0.028)	16.520(0.032)	35.692(0.156)	0.019(0.003)
1999cp	JRK07	0.011(0.001)	51364.08(0.16)	0.6690	0.339(0.199)	-0.084(0.031)	13.688(0.037)	33.360(0.231)	0.019(0.003)
1999dq	JRK07	0.013(0.001)	51436.62(0.06)	1.0000	0.849(0.063)	0.059(0.030)	14.191(0.064)	33.475(0.198)	0.081(0.013)
1999ee	JRK07	0.011(0.001)	51470.18(0.04)	1.0000	0.797(0.044)	0.239(0.025)	14.611(0.029)	33.312(0.222)	0.016(0.003)
1999ek	JRK07	0.018(0.001)	51482.76(0.14)	1.0000	-0.677(0.106)	0.159(0.072)	15.703(0.242)	34.456(0.200)	0.415(0.066)
1999gp	JRK07	0.027(0.001)	51551.39(0.07)	1.0000	1.583(0.082)	0.014(0.028)	15.786(0.042)	35.319(0.158)	0.045(0.007)
2000ca	JRK07	0.023(0.001)	51666.66(0.24)	0.9450	0.479(0.127)	-0.102(0.029)	15.325(0.049)	35.073(0.165)	0.054(0.009)
2000cf	JRK07	0.037(0.001)	51673.41(0.39)	0.9330	-0.485(0.110)	-0.021(0.030)	16.815(0.041)	36.168(0.152)	0.026(0.004)
2000cn	JRK07	0.024(0.001)	51707.91(0.12)	0.9940	-2.376(0.256)	0.086(0.032)	16.299(0.047)	35.046(0.168)	0.046(0.007)
2000dk	JRK07	0.018(0.001)	51812.89(0.18)	0.9990	-1.906(0.171)	-0.020(0.033)	15.115(0.051)	34.269(0.183)	0.057(0.009)
2000fa	JRK07	0.022(0.001)	51893.07(0.12)	0.9620	0.496(0.147)	0.048(0.032)	15.652(0.053)	34.923(0.172)	0.056(0.009)
2001V	JRK07	0.017(0.001)	51974.28(0.06)	1.0000	0.854(0.101)	-0.020(0.027)	14.319(0.032)	33.858(0.257)	0.016(0.003)
2001ba	JRK07	0.030(0.001)	52034.83(0.20)	0.7880	0.111(0.121)	-0.181(0.041)	15.932(0.047)	35.883(0.179)	0.052(0.008)
2001cn	JRK07	0.015(0.001)	52073.56(0.30)	1.0000	-0.584(0.080)	0.131(0.029)	15.036(0.047)	33.890(0.186)	0.048(0.008)
2001cz	JRK07	0.015(0.001)	52104.51(0.15)	0.9980	0.085(0.112)	0.048(0.031)	14.807(0.061)	34.019(0.188)	0.086(0.014)
2001G	CFA3	0.018(0.001)	51931.25(1.43)	0.9120	0.163(0.480)	-0.042(0.044)	14.710(0.052)	34.223(0.198)	0.013(0.002)
2001V	CFA3	0.016(0.001)	51973.81(0.08)	0.9990	0.855(0.125)	-0.008(0.028)	14.312(0.034)	33.811(0.249)	0.016(0.003)
2001ah	CFA3	0.059(0.001)	52006.90(0.97)	0.8110	1.134(0.731)	-0.033(0.033)	17.385(0.073)	37.004(0.214)	0.011(0.002)
2001ay	CFA3	0.031(0.001)	52025.61(0.64)	0.0821	2.971(0.310)	0.088(0.035)	16.487(0.044)	35.977(0.166)	0.015(0.002)
2001az	CFA3	0.040(0.001)	52030.96(1.33)	1.0000	1.173(0.709)	-0.082(0.035)	16.672(0.060)	36.454(0.162)	0.048(0.008)
2001bf	CFA3	0.015(0.001)	52046.87(0.47)	0.2710	0.583(0.157)	0.001(0.033)	14.504(0.067)	33.938(0.185)	0.079(0.013)
2001eh	CFA3	0.037(0.001)	52170.11(0.62)	0.6380	1.614(0.232)	-0.028(0.032)	16.383(0.048)	36.054(0.154)	0.050(0.008)

Table 13 — *Continued*

SN	Set	z_{cmb}	t_{peak}	P_{fit}	x_1	c	m_B	μ	$E(B-V)$
2001ep	CFA3	0.013(0.001)	52200.24(0.18)	0.9270	-0.908(0.105)	0.081(0.029)	14.650(0.042)	33.619(0.195)	0.039(0.006)
2001fe	CFA3	0.015(0.001)	52229.24(0.46)	0.9980	0.561(0.155)	-0.022(0.029)	14.422(0.035)	33.927(0.189)	0.018(0.003)
2002G	CFA3	0.035(0.001)	52300.13(0.60)	0.5760	-1.401(0.524)	0.203(0.050)	17.312(0.081)	35.822(0.181)	0.010(0.002)
2002cr	CFA3	0.010(0.001)	52408.90(0.08)	0.9750	-0.463(0.120)	-0.020(0.029)	13.944(0.038)	33.300(0.227)	0.019(0.003)
2002de	CFA3	0.028(0.001)	52433.96(0.33)	0.9990	0.548(0.644)	0.111(0.033)	16.415(0.038)	35.492(0.165)	0.015(0.002)
2002dp	CFA3	0.011(0.001)	52451.16(0.24)	0.9830	-0.086(0.323)	0.093(0.033)	14.340(0.046)	33.385(0.220)	0.040(0.006)
2002dj	CFA3	0.010(0.001)	52451.46(0.16)	0.9760	0.120(0.204)	0.074(0.031)	13.716(0.063)	32.852(0.224)	0.078(0.012)
2002ha	CFA3	0.014(0.001)	52581.41(0.20)	1.0000	-1.334(0.137)	-0.062(0.035)	14.469(0.065)	33.836(0.195)	0.079(0.013)
2002he	CFA3	0.025(0.001)	52586.17(0.16)	1.0000	-1.677(0.267)	-0.044(0.041)	15.992(0.061)	35.254(0.162)	0.032(0.005)
2002hu	CFA3	0.038(0.001)	52592.48(0.19)	0.9940	0.409(0.178)	-0.073(0.029)	16.379(0.040)	36.024(0.144)	0.036(0.006)
2002jy	CFA3	0.022(0.001)	52634.50(0.52)	0.9950	0.787(0.193)	-0.034(0.031)	15.486(0.047)	35.059(0.166)	0.044(0.007)
2002kf	CFA3	0.020(0.001)	52640.23(0.43)	0.9630	-1.124(0.117)	-0.013(0.034)	15.501(0.070)	34.741(0.168)	0.086(0.014)
2003U	CFA3	0.028(0.001)	52677.57(0.22)	0.9960	-1.985(0.549)	-0.035(0.047)	16.213(0.061)	35.401(0.171)	0.024(0.004)
2003ch	CFA3	0.030(0.001)	52726.30(0.42)	0.9340	-1.264(0.215)	-0.031(0.034)	16.438(0.054)	35.717(0.159)	0.057(0.009)
2003cq	CFA3	0.034(0.001)	52739.77(0.22)	0.1830	-0.713(0.203)	0.091(0.059)	16.904(0.069)	35.869(0.184)	0.016(0.003)
2003fa	CFA3	0.039(0.001)	52807.40(0.11)	0.9600	1.408(0.172)	-0.031(0.029)	16.466(0.040)	36.116(0.143)	0.032(0.005)
2003ic	CFA3	0.054(0.001)	52907.08(1.17)	0.9870	-1.796(0.332)	-0.018(0.045)	17.378(0.068)	36.538(0.166)	0.031(0.005)
2003iv	CFA3	0.035(0.001)	52934.29(0.54)	0.9980	-2.023(0.316)	-0.054(0.042)	16.812(0.077)	36.057(0.165)	0.098(0.016)
2003it	CFA3	0.024(0.001)	52935.27(0.53)	0.7290	-1.524(0.244)	0.043(0.037)	16.127(0.054)	35.132(0.170)	0.055(0.009)
2003kc	CFA3	0.035(0.001)	52979.25(0.68)	0.0011	-0.708(0.225)	0.111(0.045)	16.901(0.065)	35.803(0.160)	0.017(0.003)
2004as	CFA3	0.033(0.001)	53086.26(0.22)	0.8210	0.358(0.195)	0.023(0.032)	16.682(0.036)	36.013(0.152)	0.012(0.002)
2004bg	CFA3	0.022(0.001)	53110.07(0.70)	0.1120	0.462(0.168)	-0.024(0.032)	15.391(0.054)	34.887(0.160)	0.018(0.003)
2004ef	CFA3	0.030(0.001)	53265.04(0.80)	0.9980	-1.671(0.307)	0.088(0.043)	16.654(0.053)	35.492(0.246)	0.044(0.007)
2005M	CFA3	0.026(0.001)	53402.76(1.77)	0.0748	1.893(0.707)	0.170(0.066)	15.894(0.083)	34.970(0.308)	0.026(0.004)
2005am	CFA3	0.010(0.001)	53436.51(0.29)	0.9970	-1.741(0.069)	0.046(0.030)	13.394(0.046)	32.357(0.231)	0.044(0.007)
2005el	CFA3	0.015(0.001)	53646.66(0.11)	0.9370	-1.242(0.060)	-0.070(0.031)	14.671(0.066)	34.076(0.287)	0.084(0.013)
2005eq	CFA3	0.029(0.001)	53654.70(0.16)	1.0000	1.208(0.130)	-0.017(0.030)	16.032(0.051)	35.611(0.213)	0.058(0.009)
2005eu	CFA3	0.035(0.001)	53660.70(0.14)	0.1520	0.903(0.126)	-0.068(0.036)	16.258(0.076)	35.955(0.147)	0.100(0.016)
2005hc	CFA3	0.045(0.001)	53668.36(0.19)	0.9450	0.409(0.143)	-0.024(0.029)	17.114(0.034)	36.604(0.202)	0.026(0.004)
2005hj	CFA3	0.057(0.001)	53673.28(1.07)	0.7920	2.303(0.495)	-0.060(0.040)	17.454(0.054)	37.326(0.247)	0.032(0.005)
2005ir	CFA3	0.075(0.001)	53683.45(1.05)	0.6880	2.994(0.788)	-0.043(0.046)	18.247(0.055)	38.157(0.295)	0.025(0.004)
2005iq	CFA3	0.034(0.001)	53687.83(0.19)	1.0000	-1.147(0.152)	-0.087(0.029)	16.558(0.033)	36.031(0.209)	0.017(0.003)
2005kc	CFA3	0.015(0.001)	53697.83(0.11)	0.0018	-0.328(0.098)	0.242(0.034)	15.441(0.075)	33.976(0.260)	0.097(0.016)
2005ki	CFA3	0.020(0.001)	53705.44(0.13)	0.9910	-1.636(0.112)	-0.075(0.034)	15.327(0.041)	34.694(0.239)	0.026(0.004)
2005mc	CFA3	0.026(0.001)	53733.95(0.31)	0.6290	-2.469(0.179)	0.238(0.036)	17.013(0.045)	35.261(0.231)	0.036(0.006)
2005lz	CFA3	0.041(0.001)	53736.06(0.21)	0.0874	-1.018(0.164)	0.064(0.035)	17.384(0.060)	36.392(0.151)	0.085(0.014)
2005na	CFA3	0.027(0.001)	53741.67(0.54)	0.7100	-0.310(0.127)	-0.018(0.035)	15.859(0.062)	35.228(0.219)	0.062(0.010)
2005ms	CFA3	0.027(0.001)	53744.16(0.11)	0.9620	0.334(0.125)	-0.050(0.029)	15.876(0.038)	35.437(0.153)	0.027(0.004)
2006D	CFA3	0.010(0.001)	53757.48(0.14)	1.0000	-1.496(0.100)	-0.002(0.029)	13.854(0.042)	33.006(0.231)	0.037(0.006)
2006N	CFA3	0.014(0.001)	53761.04(0.29)	0.7650	-2.008(0.117)	-0.022(0.033)	14.869(0.064)	34.013(0.189)	0.078(0.012)
2006S	CFA3	0.033(0.001)	53770.16(0.17)	0.1660	0.856(0.110)	0.049(0.028)	16.596(0.031)	35.915(0.147)	0.014(0.002)
2006ac	CFA3	0.024(0.001)	53781.88(0.14)	0.9170	-0.994(0.099)	0.039(0.029)	15.897(0.033)	34.988(0.155)	0.013(0.002)
2006an	CFA3	0.065(0.001)	53790.55(0.04)	0.0011	0.338(0.230)	-0.044(0.033)	17.818(0.049)	37.361(0.153)	0.022(0.003)
2006az	CFA3	0.032(0.001)	53826.97(0.13)	0.5090	-1.423(0.070)	-0.074(0.028)	16.227(0.030)	35.619(0.147)	0.012(0.002)
2006ax	CFA3	0.017(0.001)	53827.49(0.06)	0.9990	0.270(0.066)	-0.081(0.028)	14.796(0.041)	34.449(0.241)	0.041(0.007)
2006bt	CFA3	0.032(0.001)	53858.36(0.20)	0.1530	0.127(0.107)	0.097(0.028)	16.678(0.040)	35.742(0.146)	0.041(0.007)
2006cf	CFA3	0.042(0.001)	53875.05(0.86)	0.2870	-0.609(0.331)	-0.097(0.042)	16.820(0.055)	36.400(0.164)	0.013(0.002)
2006cj	CFA3	0.068(0.001)	53875.92(1.40)	1.0000	2.546(0.919)	-0.099(0.034)	17.876(0.042)	37.904(0.185)	0.010(0.002)
2006cq	CFA3	0.049(0.001)	53889.95(0.51)	0.9460	0.196(0.541)	0.005(0.033)	17.325(0.035)	36.693(0.157)	0.013(0.002)
2006cp	CFA3	0.023(0.001)	53897.70(0.09)	0.9700	0.290(0.111)	0.056(0.030)	15.711(0.037)	34.927(0.160)	0.023(0.004)
2006cz	CFA3	0.043(0.001)	53907.02(1.58)	0.0429	1.613(0.710)	0.103(0.056)	16.755(0.070)	36.007(0.245)	0.081(0.013)
2006et	CFA3	0.022(0.001)	53994.52(0.33)	0.9880	0.693(0.192)	0.130(0.032)	15.704(0.040)	34.740(0.232)	0.015(0.002)
2006gr	CFA3	0.034(0.001)	54013.36(0.10)	0.8150	0.814(0.108)	0.060(0.030)	16.716(0.056)	35.992(0.146)	0.069(0.011)
2006kf	CFA3	0.021(0.001)	54041.32(0.31)	0.9740	-2.181(0.135)	-0.052(0.046)	15.724(0.123)	34.941(0.237)	0.180(0.029)
2006mo	CFA3	0.037(0.001)	54047.86(0.41)	0.9700	-2.110(0.172)	0.037(0.038)	17.181(0.053)	36.123(0.158)	0.036(0.006)
2006le	CFA3	0.017(0.001)	54048.46(0.06)	1.0000	0.839(0.077)	-0.058(0.057)	14.766(0.189)	34.423(0.168)	0.305(0.049)
2006mp	CFA3	0.023(0.001)	54054.31(0.18)	0.9890	0.921(0.253)	0.005(0.031)	15.729(0.038)	35.198(0.163)	0.029(0.005)
2006ob	CFA3	0.059(0.001)	54063.04(0.23)	0.8430	-2.215(0.214)	-0.019(0.035)	17.975(0.038)	37.081(0.214)	0.026(0.004)
2006on	CFA3	0.068(0.001)	54064.14(0.84)	0.9450	0.829(0.798)	0.101(0.056)	18.280(0.090)	37.428(0.188)	0.104(0.017)
2006oa	CFA3	0.059(0.001)	54067.05(0.19)	0.8930	1.152(0.315)	-0.008(0.032)	17.633(0.040)	37.173(0.145)	0.032(0.005)
2006qo	CFA3	0.029(0.001)	54083.00(0.09)	0.9450	0.337(0.093)	0.173(0.029)	16.581(0.039)	35.430(0.149)	0.032(0.005)
2006sr	CFA3	0.024(0.001)	54092.89(0.20)	0.9760	-1.311(0.162)	-0.009(0.033)	15.895(0.061)	35.095(0.159)	0.075(0.012)
2006te	CFA3	0.032(0.001)	54097.37(0.51)	0.8750	-0.159(0.130)	-0.078(0.034)	16.288(0.051)	35.871(0.153)	0.037(0.006)
2006td	CFA3	0.016(0.001)	54098.92(0.47)	1.0000	-1.335(0.181)	0.101(0.033)	15.477(0.062)	34.322(0.181)	0.071(0.011)
2007F	CFA3	0.025(0.001)	54123.97(0.08)	1.0000	0.549(0.073)	-0.050(0.027)	15.631(0.030)	35.222(0.154)	0.013(0.002)
2007R	CFA3	0.031(0.001)	54129.49(0.51)	0.0978	-1.247(0.132)	-0.083(0.035)	16.453(0.059)	35.898(0.159)	0.038(0.006)
2007ai	CFA3	0.032(0.001)	54173.83(0.55)	0.2080	1.261(0.297)	0.208(0.054)	16.841(0.159)	35.706(0.241)	0.246(0.039)
2007au	CFA3	0.020(0.001)	54184.23(0.16)	0.4100	-2.818(0.176)	0.188(0.035)	16.311(0.054)	34.670(0.168)	0.055(0.009)
2007bc	CFA3	0.022(0.001)	54200.56(0.20)	0.1130	-1.315(0.107)	0.016(0.030)	15.660(0.035)	34.781(0.230)	0.018(0.003)
2007bd	CFA3	0.032(0.001)	54206.64(0.10)	1.0000	-1.356(0.104)	-0.048(0.030)	16.315(0.036)	35.635(0.212)	0.027(0.004)
2007ca	CFA3	0.015(0.001)	54227.85(0.12)	0.3870	0.553(0.115)	0.217(0.030)	15.691(0.049)	34.429(0.256)	0.054(0.009)
2007ci	CFA3	0.019(0.001)	54246.73(0.10)	0.6890	-2.753(0.188)	0.030(0.035)	15.615(0.042)	34.488(0.172)	0.021(0.003)
2007co	CFA3	0.027(0.001)	54265.13(0.11)	1.0000	-0.162(0.095)	0.079(0.030)	16.266(0.063)	35.347(0.149)	0.081(0.013)
2007cp	CFA3	0.038(0.001)	54269.75(0.45)	0.0345	-2.905(1.078)	-0.026(0.059)	16.905(0.062)	35.936(0.276)	0.036(0.006)
2007cq	CFA3	0.025(0.001)	54281.04(0.12)	0.5920	-0.642(0.163)	-0.037(0.030)	15.605(0.062)	34.988(0.152)	0.079(0.013)

Table 13 — *Continued*

SN	Set	z_{cmb}	t_{peak}	P_{fit}	x_1	c	m_B	μ	$E(B-V)$
2007qe	CFA3	0.024(0.001)	54429.80(0.06)	0.9870	0.689(0.076)	0.048(0.027)	15.803(0.036)	35.102(0.155)	0.031(0.005)
2008L	CFA3	0.019(0.001)	54493.39(0.42)	0.7630	-1.550(0.155)	-0.089(0.042)	14.977(0.091)	34.399(0.180)	0.118(0.019)
2008bf	CFA3	0.022(0.001)	54555.01(0.15)	0.9610	0.319(0.103)	-0.023(0.028)	15.464(0.035)	34.939(0.158)	0.027(0.004)
2007A	CFA4	0.017(0.001)	54113.33(0.21)	0.9540	0.427(0.272)	0.068(0.037)	15.379(0.059)	34.575(0.314)	0.059(0.010)
2007fb	CFA4	0.017(0.001)	54288.69(0.87)	0.9940	-1.748(0.474)	-0.118(0.047)	15.267(0.069)	34.754(0.243)	0.045(0.007)
2007hu	CFA4	0.036(0.001)	54353.23(2.11)	0.5630	-1.257(0.526)	0.210(0.076)	17.458(0.153)	35.965(0.262)	0.037(0.006)
2007kh	CFA4	0.050(0.001)	54365.04(0.15)	0.6680	0.978(0.977)	0.087(0.112)	17.536(0.264)	36.748(0.482)	0.147(0.023)
2007jg	CFA4	0.037(0.001)	54366.42(0.52)	0.9570	-0.714(0.154)	-0.056(0.039)	16.968(0.071)	36.403(0.280)	0.079(0.013)
2007is	CFA4	0.030(0.001)	54366.93(0.73)	0.6780	-0.462(0.213)	0.031(0.037)	16.198(0.046)	35.388(0.207)	0.016(0.003)
2007kk	CFA4	0.041(0.001)	54383.80(0.38)	1.0000	0.847(0.172)	-0.022(0.041)	16.710(0.113)	36.255(0.194)	0.169(0.027)
2007nq	CFA4	0.044(0.001)	54398.31(0.56)	1.0000	-1.599(0.198)	-0.066(0.038)	17.118(0.058)	36.462(0.280)	0.029(0.005)
2007su	CFA4	0.027(0.001)	54460.46(0.89)	0.9990	0.311(0.387)	0.172(0.041)	16.634(0.078)	35.481(0.208)	0.067(0.011)
2007ux	CFA4	0.032(0.001)	54465.77(0.52)	0.4970	-2.420(0.138)	0.154(0.045)	17.136(0.068)	35.660(0.214)	0.036(0.006)
2008C	CFA4	0.017(0.001)	54467.32(0.45)	1.0000	-0.694(0.167)	0.096(0.035)	15.339(0.067)	34.290(0.217)	0.068(0.011)
2007sw	CFA4	0.026(0.001)	54468.52(0.34)	0.1920	0.121(0.144)	0.098(0.033)	16.035(0.041)	35.095(0.201)	0.015(0.002)
2008Y	CFA4	0.070(0.001)	54503.69(1.02)	0.6160	-0.565(0.277)	0.065(0.042)	18.260(0.064)	37.327(0.204)	0.010(0.002)
2008Z	CFA4	0.022(0.001)	54515.48(0.09)	0.5980	1.010(0.128)	0.081(0.028)	16.159(0.033)	35.398(0.202)	0.009(0.001)
2008at	CFA4	0.035(0.001)	54526.39(1.28)	0.9710	-1.501(0.249)	0.212(0.064)	17.319(0.109)	35.785(0.263)	0.074(0.012)
2008ar	CFA4	0.027(0.001)	54534.69(0.11)	1.0000	0.003(0.096)	-0.047(0.028)	15.978(0.036)	35.484(0.196)	0.030(0.005)
2008bz	CFA4	0.061(0.001)	54578.11(0.93)	0.8500	-0.119(0.365)	-0.129(0.040)	17.641(0.059)	37.393(0.204)	0.025(0.004)
2008cf	CFA4	0.047(0.001)	54594.73(1.11)	1.0000	1.475(0.570)	-0.135(0.038)	16.728(0.054)	36.720(0.217)	0.054(0.009)
2008051	CFA4	0.040(0.001)	54616.65(0.46)	0.6820	0.823(0.172)	-0.135(0.032)	16.364(0.045)	36.265(0.195)	0.035(0.006)
2008050	CFA4	0.049(0.001)	54621.12(0.99)	0.7890	1.038(0.556)	0.024(0.038)	16.901(0.046)	36.325(0.215)	0.021(0.003)
2008fr	CFA4	0.048(0.001)	54732.41(0.55)	1.0000	0.733(0.155)	-0.135(0.032)	16.525(0.046)	36.416(0.193)	0.036(0.006)
2008gb	CFA4	0.036(0.001)	54747.06(0.71)	1.0000	0.067(0.299)	-0.016(0.042)	16.823(0.103)	36.239(0.204)	0.147(0.023)
2008gl	CFA4	0.033(0.001)	54768.47(0.16)	1.0000	-1.348(0.135)	-0.032(0.032)	16.541(0.036)	35.809(0.197)	0.023(0.004)
2008hj	CFA4	0.037(0.001)	54803.84(0.79)	0.0250	-0.536(0.376)	-0.104(0.040)	16.505(0.046)	36.116(0.208)	0.029(0.005)
2008hm	CFA4	0.019(0.001)	54805.18(0.21)	0.9370	0.175(0.127)	-0.003(0.062)	15.461(0.205)	34.850(0.222)	0.327(0.052)
2008hv	CFA4	0.014(0.001)	54817.10(0.11)	1.0000	-1.401(0.129)	-0.122(0.032)	14.439(0.041)	33.990(0.324)	0.026(0.004)
2009D	CFA4	0.025(0.001)	54842.06(0.43)	0.9990	0.419(0.150)	-0.054(0.032)	15.474(0.049)	35.059(0.201)	0.043(0.007)
2009Y	CFA4	0.010(0.001)	54876.23(0.27)	0.9000	0.376(0.101)	0.034(0.029)	13.677(0.059)	32.976(0.261)	0.075(0.012)
2009ad	CFA4	0.029(0.001)	54886.60(0.18)	1.0000	0.180(0.106)	-0.062(0.032)	15.928(0.065)	35.508(0.196)	0.083(0.013)
2009al	CFA4	0.024(0.001)	54897.31(0.14)	0.0082	-0.447(0.121)	0.069(0.029)	15.951(0.035)	35.025(0.202)	0.020(0.003)
2009ds	CFA4	0.021(0.001)	54961.10(0.31)	0.9580	0.498(0.166)	-0.052(0.034)	15.227(0.045)	34.820(0.211)	0.031(0.005)
2009kk	CFA4	0.013(0.001)	55126.85(0.37)	1.0000	-1.216(0.113)	-0.080(0.037)	14.446(0.082)	33.886(0.240)	0.118(0.019)
2009lf	CFA4	0.044(0.001)	55150.41(0.48)	0.3280	-1.677(0.110)	-0.040(0.037)	16.672(0.054)	35.920(0.214)	0.045(0.007)
2009kq	CFA4	0.013(0.001)	55155.14(0.29)	1.0000	-0.040(0.176)	-0.013(0.034)	14.249(0.046)	33.641(0.239)	0.035(0.006)
2009le	CFA4	0.017(0.001)	55166.08(0.10)	0.9850	-0.000(0.207)	0.037(0.039)	15.041(0.046)	34.277(0.221)	0.014(0.002)
2009na	CFA4	0.022(0.001)	55201.98(0.14)	0.8080	-0.738(0.137)	-0.011(0.031)	15.543(0.036)	34.830(0.204)	0.027(0.004)
2009nq	CFA4	0.015(0.001)	55203.73(0.86)	1.0000	-0.243(0.830)	0.049(0.049)	15.053(0.091)	34.217(0.255)	0.125(0.020)
2010A	CFA4	0.020(0.001)	55212.45(0.16)	0.9460	0.461(0.169)	0.116(0.037)	15.589(0.043)	34.639(0.219)	0.025(0.004)
2010Y	CFA4	0.011(0.001)	55247.93(0.13)	0.9900	-2.430(0.139)	-0.040(0.036)	14.743(0.042)	33.885(0.250)	0.012(0.002)
2010ag	CFA4	0.034(0.001)	55269.46(0.68)	0.0109	1.332(0.256)	0.067(0.034)	16.427(0.043)	35.754(0.204)	0.027(0.004)
2010ai	CFA4	0.019(0.001)	55277.23(0.09)	1.0000	-1.563(0.130)	-0.075(0.034)	15.772(0.039)	35.147(0.210)	0.008(0.001)
2010dw	CFA4	0.039(0.001)	55358.30(0.39)	0.3610	0.317(0.182)	0.089(0.034)	16.900(0.061)	36.014(0.197)	0.080(0.013)
2010dt	CFA4	0.053(0.001)	55361.66(0.25)	0.2690	-0.007(0.607)	-0.071(0.054)	17.379(0.079)	36.962(0.207)	0.029(0.005)
2004ef	CSP	0.030(0.001)	53264.17(0.05)	1.0000	-1.274(0.043)	0.076(0.021)	16.595(0.036)	35.530(0.189)	0.044(0.007)
2004eo	CSP	0.015(0.001)	53278.34(0.04)	0.9970	-1.151(0.040)	0.002(0.024)	14.791(0.059)	33.979(0.171)	0.081(0.013)
2004ey	CSP	0.016(0.001)	53304.48(0.06)	1.0000	0.051(0.042)	-0.103(0.025)	14.468(0.071)	34.159(0.170)	0.103(0.016)
2004gs	CSP	0.027(0.001)	53355.60(0.14)	0.5630	-1.682(0.056)	0.126(0.022)	16.886(0.027)	35.603(0.138)	0.025(0.004)
2004gu	CSP	0.047(0.001)	53362.46(0.23)	1.0000	1.320(0.116)	0.059(0.021)	17.162(0.025)	36.512(0.128)	0.021(0.003)
2005M	CSP	0.023(0.001)	53406.15(0.06)	1.0000	1.170(0.063)	-0.021(0.020)	15.645(0.025)	35.233(0.202)	0.025(0.004)
2005ag	CSP	0.080(0.001)	53415.11(0.17)	1.0000	0.134(0.080)	-0.043(0.025)	18.201(0.030)	37.713(0.127)	0.033(0.005)
2005al	CSP	0.012(0.001)	53430.65(0.18)	1.0000	-1.183(0.056)	-0.090(0.022)	14.611(0.037)	34.089(0.193)	0.044(0.007)
2005bg	CSP	0.025(0.001)	53470.15(0.27)	0.7460	0.288(0.120)	-0.051(0.021)	15.595(0.028)	35.155(0.141)	0.026(0.004)
2005bo	CSP	0.014(0.001)	53478.56(0.30)	1.0000	-0.940(0.169)	0.200(0.023)	15.372(0.036)	33.956(0.179)	0.037(0.006)
2005el	CSP	0.015(0.001)	53646.64(0.09)	0.9960	-1.212(0.077)	-0.141(0.025)	14.589(0.062)	34.224(0.245)	0.084(0.013)
2005eq	CSP	0.029(0.001)	53654.93(0.21)	1.0000	1.232(0.107)	-0.023(0.023)	16.002(0.046)	35.602(0.194)	0.060(0.010)
2005hc	CSP	0.045(0.001)	53667.75(0.13)	1.0000	0.691(0.088)	-0.023(0.021)	17.046(0.025)	36.570(0.179)	0.024(0.004)
2005hj	CSP	0.057(0.001)	53674.46(0.38)	0.3750	1.419(0.187)	-0.029(0.023)	17.466(0.027)	37.114(0.186)	0.025(0.004)
2005ir	CSP	0.075(0.001)	53685.50(0.22)	0.6950	0.399(0.170)	-0.005(0.022)	18.171(0.026)	37.598(0.177)	0.025(0.004)
2005iq	CSP	0.034(0.001)	53687.65(0.09)	1.0000	-1.001(0.074)	-0.108(0.021)	16.498(0.023)	36.058(0.186)	0.018(0.003)
2005kc	CSP	0.015(0.001)	53697.70(0.06)	0.9990	-0.696(0.072)	0.148(0.026)	15.268(0.070)	34.053(0.247)	0.098(0.016)
2005ki	CSP	0.020(0.001)	53705.32(0.09)	0.9300	-1.349(0.056)	-0.101(0.022)	15.275(0.028)	34.765(0.214)	0.026(0.004)
2005mc	CSP	0.026(0.001)	53731.24(0.34)	0.9020	-1.802(0.073)	0.192(0.025)	16.766(0.043)	35.256(0.203)	0.036(0.006)
2005na	CSP	0.027(0.001)	53741.13(0.14)	0.2010	-0.584(0.062)	-0.096(0.023)	15.684(0.048)	35.265(0.197)	0.063(0.010)
2006ax	CSP	0.017(0.001)	53827.53(0.04)	1.0000	0.122(0.049)	-0.097(0.020)	14.744(0.034)	34.425(0.225)	0.040(0.006)
2006bh	CSP	0.011(0.001)	53833.42(0.10)	1.0000	-1.545(0.058)	-0.064(0.021)	14.089(0.025)	33.431(0.207)	0.021(0.003)
2006ej	CSP	0.020(0.001)	53976.06(0.32)	1.0000	-1.421(0.081)	-0.030(0.024)	15.438(0.035)	34.689(0.154)	0.028(0.005)
2006ev	CSP	0.028(0.001)	53989.44(0.31)	1.0000	-1.261(0.079)	0.097(0.027)	16.811(0.060)	35.681(0.140)	0.073(0.012)
2006et	CSP	0.022(0.001)	53994.20(0.07)	1.0000	0.676(0.070)	0.130(0.020)	15.702(0.023)	34.737(0.205)	0.015(0.002)
2006kf	CSP	0.021(0.001)	54040.91(0.14)	0.9980	-1.827(0.090)	-0.049(0.037)	15.662(0.120)	34.918(0.225)	0.182(0.029)
2006ob	CSP	0.059(0.001)	54063.10(0.25)	0.9990	-1.884(0.145)	-0.052(0.027)	17.930(0.032)	37.189(0.192)	0.027(0.004)
2006ot	CSP	0.052(0.001)	54063.66(0.47)	0.0458	0.695(0.138)	0.101(0.023)	17.703(0.031)	36.832(0.129)	0.018(0.003)
2006py	CSP	0.057(0.001)	54070.95(0.44)	0.9740	0.076(0.348)	-0.001(0.025)	17.608(0.042)	36.976(0.132)	0.053(0.008)

Table 13 — *Continued*

SN	Set	z_{cmb}	t_{peak}	P_{fit}	x_1	c	m_B	μ	$E(B-V)$
2007A	CSP	0.017(0.001)	54113.18(0.16)	0.9920	0.561(0.214)	0.090(0.025)	15.397(0.048)	34.541(0.236)	0.059(0.010)
2007ai	CSP	0.032(0.001)	54173.80(0.37)	1.0000	0.976(0.156)	0.156(0.044)	16.901(0.143)	35.895(0.216)	0.215(0.034)
2007as	CSP	0.018(0.001)	54181.66(0.22)	0.0177	-0.890(0.082)	-0.094(0.027)	15.183(0.082)	34.714(0.153)	0.124(0.020)
2007bc	CSP	0.022(0.001)	54200.46(0.22)	1.0000	-1.109(0.092)	0.036(0.023)	15.651(0.025)	34.736(0.212)	0.018(0.003)
2007bd	CSP	0.032(0.001)	54206.84(0.07)	0.8540	-0.953(0.072)	-0.067(0.022)	16.273(0.029)	35.708(0.190)	0.027(0.004)
2007ca	CSP	0.015(0.001)	54227.80(0.08)	0.9970	0.573(0.076)	0.200(0.023)	15.628(0.042)	34.422(0.242)	0.053(0.008)
2007hx	CSP	0.079(0.001)	54354.56(0.43)	0.6350	0.139(0.174)	0.116(0.025)	19.018(0.029)	38.022(0.131)	0.022(0.004)
2007jh	CSP	0.041(0.001)	54366.71(0.16)	0.4850	-0.517(0.098)	-0.018(0.028)	17.031(0.057)	36.370(0.133)	0.077(0.012)
2007jg	CSP	0.037(0.001)	54366.77(0.16)	0.1420	-0.616(0.098)	0.043(0.023)	17.086(0.055)	36.219(0.182)	0.079(0.013)
2007nq	CSP	0.044(0.001)	54398.17(0.25)	1.0000	-1.784(0.090)	-0.019(0.024)	17.149(0.030)	36.316(0.185)	0.022(0.004)
2008R	CSP	0.013(0.001)	54493.00(0.26)	0.4100	-2.000(0.084)	0.036(0.025)	14.968(0.045)	33.927(0.190)	0.053(0.008)
2008bc	CSP	0.016(0.001)	54550.14(0.05)	0.9220	0.430(0.058)	-0.146(0.044)	14.178(0.166)	34.060(0.163)	0.292(0.047)
2008bq	CSP	0.034(0.001)	54563.89(0.22)	1.0000	0.245(0.082)	0.061(0.024)	16.479(0.055)	35.674(0.131)	0.075(0.012)
2008gp	CSP	0.033(0.001)	54779.20(0.06)	0.9990	-0.178(0.054)	-0.073(0.025)	16.175(0.063)	35.741(0.132)	0.090(0.014)
2008ia	CSP	0.023(0.001)	54813.07(0.14)	0.9840	-1.308(0.081)	-0.029(0.032)	15.702(0.103)	34.967(0.146)	0.159(0.025)
2008hv	CSP	0.014(0.001)	54817.02(0.06)	0.9910	-1.260(0.064)	-0.072(0.021)	14.460(0.028)	33.870(0.254)	0.026(0.004)

Note. — Fit parameters of all low-z SNe Ia that passed all cuts. The redshift is corrected for coherent flow effects. t_{peak} is the fitted time of B-band maximum m_B. P_{fit} is the SALT2 Fit Probability. x_1, c, m_B, and μ are the parameters as defined in Equation 2. The Milky Way Galaxy Reddening is given in the direction of the SN by Schlegel et al. (1998), and corrected by 6-14% as described in S14.

Table 14
Fit Parameters of the Pan-STARRS1 Spectroscopic Sample

PS1 name	z_{cmb}	t_{peak}	P_{fit}	x_1	c	m_B	μ	$E(B-V)$	Host Mass
PS1-0909006	0.283(0.001)	55075.41(2.59)	0.745	-0.726(1.428)	0.008(0.073)	21.352(0.094)	40.579(0.309)	0.035(0.006)	9.1620
PS1-0910017	0.319(0.005)	55109.65(0.57)	0.902	-0.704(0.473)	-0.115(0.037)	21.412(0.045)	41.035(0.129)	0.018(0.003)	· · ·
PS1-0910018	0.264(0.001)	55109.23(0.59)	0.246	-2.253(0.625)	-0.174(0.050)	20.975(0.055)	40.573(0.135)	0.020(0.003)	· · ·
PS1-10c	0.153(0.001)	55210.25(0.22)	0.930	-2.147(0.169)	0.020(0.033)	20.284(0.038)	39.276(0.114)	0.022(0.003)	8.3920
PS1-10d	0.230(0.001)	55204.10(0.51)	0.742	-0.222(0.482)	0.124(0.041)	21.408(0.049)	40.336(0.133)	0.007(0.001)	10.5900
PS1-10e	0.246(0.001)	55215.72(0.30)	0.084	0.730(0.274)	0.020(0.028)	21.164(0.037)	40.557(0.097)	0.018(0.003)	11.0200
PS1-10g	0.136(0.001)	55201.05(0.63)	0.992	0.634(0.744)	-0.077(0.040)	19.394(0.052)	39.085(0.135)	0.021(0.003)	10.4100
PS1-10h	0.249(0.005)	55207.44(0.42)	0.720	-0.099(0.499)	-0.107(0.032)	20.710(0.040)	40.392(0.127)	0.022(0.004)	· · ·
PS1-10i	0.149(0.001)	55203.68(0.26)	0.601	-0.121(0.291)	-0.058(0.036)	19.614(0.044)	39.137(0.113)	0.023(0.004)	· · ·
PS1-10j	0.436(0.001)	55213.59(0.60)	0.931	-0.510(0.579)	-0.001(0.046)	22.853(0.047)	42.141(0.165)	0.007(0.001)	11.3200
PS1-10k	0.341(0.001)	55216.36(0.27)	0.965	0.273(0.255)	-0.030(0.027)	21.797(0.032)	41.286(0.122)	0.015(0.002)	9.6370
PS1-10l	0.371(0.001)	55214.50(0.39)	0.997	1.335(0.308)	-0.083(0.028)	21.793(0.033)	41.602(0.105)	0.024(0.004)	8.5220
PS1-10m	0.619(0.001)	55215.12(0.81)	0.650	1.536(0.706)	-0.166(0.050)	23.197(0.048)	43.300(0.197)	0.015(0.002)	9.0170
PS1-10n	0.461(0.001)	55222.82(0.39)	0.792	1.196(0.397)	-0.103(0.033)	22.477(0.039)	42.328(0.133)	0.016(0.003)	8.8120
PS1-10o	0.221(0.001)	55227.64(0.15)	0.119	-0.771(0.191)	-0.114(0.030)	20.605(0.036)	40.218(0.103)	0.016(0.003)	11.3100
PS1-10p	0.311(0.001)	55223.21(0.20)	0.899	-1.124(0.242)	-0.115(0.034)	21.611(0.039)	41.178(0.119)	0.017(0.003)	9.1670
PS1-10r	0.119(0.001)	55213.12(0.18)	0.808	-0.122(0.207)	0.111(0.035)	19.634(0.040)	38.617(0.112)	0.006(0.001)	11.0000
PS1-10v	0.100(0.001)	55238.92(0.30)	0.992	1.035(0.286)	0.039(0.032)	19.132(0.041)	38.507(0.110)	0.019(0.003)	9.9770
PS1-10w	0.032(0.001)	55248.01(0.11)	0.775	-0.504(0.128)	-0.005(0.038)	16.436(0.045)	35.736(0.130)	0.006(0.001)	10.2000
PS1-10z	0.141(0.001)	55235.96(0.30)	0.898	-2.375(0.396)	0.045(0.043)	20.303(0.052)	39.180(0.127)	0.024(0.004)	7.4570
PS1-10af	0.244(0.001)	55216.97(0.24)	0.756	-0.466(0.279)	0.073(0.033)	21.417(0.040)	40.472(0.111)	0.006(0.001)	10.4800
PS1-10aj	0.196(0.001)	55210.94(0.20)	0.399	-0.220(0.166)	-0.045(0.027)	20.337(0.035)	39.807(0.099)	0.025(0.004)	10.7100
PS1-10hu	0.127(0.001)	55270.80(0.64)	0.947	0.155(0.298)	0.062(0.037)	19.372(0.040)	38.551(0.136)	0.011(0.002)	· · ·
PS1-10ia	0.409(0.001)	55272.94(1.28)	0.006	-0.434(1.223)	0.028(0.068)	22.395(0.072)	41.599(0.307)	0.010(0.002)	11.5900
PS1-10if	0.151(0.001)	55277.31(0.52)	0.283	-1.987(0.565)	0.127(0.061)	20.730(0.062)	39.399(0.224)	0.016(0.003)	10.6300
PS1-10ig	0.260(0.001)	55270.32(0.65)	0.996	0.771(0.502)	-0.077(0.033)	20.946(0.038)	40.655(0.149)	0.007(0.001)	8.4220
PS1-10ik	0.231(0.001)	55281.52(0.37)	0.988	-0.442(0.324)	-0.113(0.044)	20.664(0.046)	40.318(0.153)	0.008(0.001)	8.9120
PS1-10im	0.510(0.001)	55288.90(1.03)	0.911	0.391(1.235)	-0.114(0.082)	22.503(0.145)	42.277(0.275)	0.007(0.001)	9.5470
PS1-10io	0.221(0.001)	55300.14(0.65)	0.888	1.358(0.482)	-0.126(0.043)	20.384(0.055)	40.331(0.128)	0.020(0.003)	8.9120
PS1-10ir	0.251(0.001)	55337.37(0.25)	0.987	-0.126(0.379)	-0.034(0.036)	21.147(0.050)	40.594(0.113)	0.006(0.001)	9.4770
PS1-10iw	0.447(0.001)	55326.57(1.16)	0.015	0.378(0.557)	-0.021(0.054)	22.489(0.064)	41.964(0.187)	0.009(0.001)	9.2070
PS1-10ix	0.382(0.001)	55338.24(0.47)	0.988	-0.162(0.761)	-0.055(0.059)	22.194(0.077)	41.702(0.152)	0.006(0.001)	7.7620
PS1-10iy	0.443(0.001)	55327.75(2.35)	0.127	0.289(0.718)	-0.183(0.047)	22.511(0.066)	42.493(0.194)	0.009(0.002)	9.9070
PS1-10ji	0.231(0.001)	55358.81(0.39)	0.681	-0.962(0.538)	0.239(0.046)	21.661(0.052)	40.115(0.143)	0.009(0.001)	9.8820
PS1-10jk	0.430(0.001)	55356.45(0.84)	0.037	1.602(0.846)	-0.034(0.044)	22.425(0.065)	42.113(0.158)	0.005(0.001)	8.1620
PS1-10jl	0.530(0.001)	55353.71(1.06)	0.993	0.891(0.865)	0.026(0.051)	22.649(0.059)	42.047(0.223)	0.010(0.002)	9.0020
PS1-10jp	0.387(0.001)	55367.83(0.74)	0.680	-0.679(0.666)	0.031(0.056)	22.199(0.060)	41.358(0.181)	0.008(0.001)	11.3700
PS1-10jt	0.336(0.001)	55352.24(0.65)	0.151	-0.575(0.544)	0.144(0.045)	22.200(0.059)	41.013(0.141)	0.006(0.001)	9.8320
PS1-10ju	0.323(0.001)	55348.77(0.55)	0.853	0.233(0.480)	0.045(0.054)	21.919(0.065)	41.162(0.153)	0.009(0.001)	9.8020
PS1-10jv	0.360(0.001)	55355.73(0.45)	0.294	0.539(0.468)	-0.002(0.034)	21.850(0.041)	41.288(0.123)	0.008(0.001)	8.4520
PS1-10jw	0.360(0.001)	55358.98(0.57)	0.195	1.023(0.585)	-0.067(0.040)	21.765(0.052)	41.479(0.142)	0.006(0.001)	10.1400
PS1-10jz	0.550(0.001)	55354.50(0.99)	0.486	0.518(0.819)	-0.070(0.051)	22.868(0.066)	42.518(0.206)	0.006(0.001)	10.4500
PS1-10kc	0.347(0.001)	55358.40(0.49)	0.424	0.447(0.597)	0.104(0.044)	22.058(0.052)	41.143(0.152)	0.006(0.001)	10.4400

Table 14 — *Continued*

PS1 name	z_{cmb}	t_{peak}	P_{fit}	x_1	c	m_B	μ	$E(B-V)$	Host Mass
PS1-10kd	0.331(0.001)	55355.20(1.08)	0.401	1.632(0.883)	0.188(0.055)	22.415(0.067)	41.398(0.199)	0.007(0.001)	11.0800
PS1-10kf	0.450(0.001)	55370.40(0.89)	0.845	0.759(0.978)	0.016(0.046)	22.411(0.062)	41.823(0.176)	0.013(0.002)	9.4470
PS1-10kl	0.443(0.001)	55367.55(0.67)	0.337	0.163(0.605)	0.046(0.047)	22.592(0.051)	41.823(0.164)	0.008(0.001)	9.3070
PS1-10kv	0.530(0.001)	55364.55(0.54)	0.003	0.441(0.455)	-0.168(0.040)	22.566(0.041)	42.521(0.146)	0.011(0.002)	9.5170
PS1-10nq	0.036(0.001)	55351.19(1.90)	0.997	2.259(1.798)	0.147(0.070)	16.983(0.079)	36.183(0.263)	0.017(0.003)	8.5020
PS1-10nu	0.064(0.001)	55427.35(0.16)	0.979	-1.115(0.126)	-0.115(0.039)	17.969(0.043)	37.537(0.127)	0.022(0.004)	7.1120
PS1-10acx	0.350(0.001)	55438.28(0.41)	0.898	1.407(0.421)	-0.025(0.032)	21.654(0.039)	41.285(0.114)	0.006(0.001)	9.6420
PS1-10aeq	0.066(0.001)	55444.20(0.51)	0.981	-0.162(0.124)	0.230(0.037)	18.699(0.047)	37.297(0.118)	0.006(0.001)	$\cdots$
PS1-10agw	0.329(0.005)	55462.21(0.27)	0.994	-0.833(0.315)	-0.156(0.037)	21.620(0.057)	41.357(0.114)	0.058(0.009)	10.6600
PS1-10ahk	0.430(0.001)	55473.49(0.67)	0.742	-0.115(0.529)	-0.162(0.055)	22.160(0.072)	42.016(0.169)	0.017(0.003)	9.4120
PS1-10ahl	0.634(0.001)	55466.70(0.86)	0.888	-0.105(0.834)	-0.214(0.066)	23.023(0.085)	43.048(0.252)	0.087(0.014)	9.8020
PS1-10axm	0.509(0.005)	55484.75(0.78)	0.937	0.413(0.715)	-0.040(0.054)	22.494(0.065)	42.036(0.198)	0.023(0.004)	9.7720
PS1-10ayb	0.140(0.001)	55494.51(0.18)	0.998	-0.894(0.254)	-0.022(0.037)	19.805(0.049)	39.105(0.109)	0.009(0.001)	10.8800
PS1-10bji	0.148(0.001)	55507.46(0.25)	0.940	0.591(0.299)	0.007(0.033)	19.706(0.041)	39.123(0.110)	0.009(0.001)	9.1820
PS1-10bjn	0.289(0.005)	55495.77(0.41)	0.903	1.492(0.495)	-0.038(0.042)	21.255(0.055)	40.942(0.160)	0.045(0.007)	10.8600
PS1-10bjz	0.309(0.005)	55514.01(0.47)	0.024	0.338(0.618)	-0.132(0.066)	21.250(0.094)	41.074(0.143)	0.029(0.005)	12.2600
PS1-10bkf	0.173(0.001)	55506.74(0.54)	0.946	-0.917(0.456)	0.058(0.036)	20.836(0.046)	39.877(0.127)	0.020(0.003)	9.8470
PS1-10bki	0.431(0.001)	55518.45(0.64)	0.051	-0.549(0.502)	-0.108(0.045)	22.528(0.054)	42.152(0.154)	0.023(0.004)	11.6400
PS1-10blh	0.318(0.001)	55522.88(0.50)	0.991	0.319(0.586)	-0.089(0.058)	21.534(0.100)	41.218(0.158)	0.018(0.003)	9.4570
PS1-10blp	0.217(0.001)	55521.14(1.75)	0.832	-0.568(1.090)	-0.092(0.087)	20.324(0.096)	39.892(0.303)	0.006(0.001)	11.1300
PS1-10bls	0.276(0.001)	55521.40(0.43)	0.951	0.830(0.428)	0.016(0.043)	21.455(0.059)	40.875(0.140)	0.006(0.001)	9.4320
PS1-10bmb	0.359(0.005)	55517.95(1.09)	0.994	-1.387(1.125)	-0.215(0.224)	21.453(0.228)	41.303(0.639)	0.060(0.010)	9.5770
PS1-10bmk	0.103(0.001)	55535.72(0.49)	0.841	-0.123(0.612)	0.215(0.061)	19.432(0.110)	38.080(0.170)	0.009(0.001)	10.9200
PS1-10byq	0.209(0.005)	55543.88(0.51)	0.896	1.539(0.638)	-0.123(0.066)	20.224(0.116)	40.186(0.191)	0.017(0.003)	9.9120
PS1-10byr	0.239(0.005)	55534.67(1.45)	0.802	-1.647(1.979)	-0.099(0.075)	21.129(0.083)	40.569(0.276)	0.063(0.011)	$\cdots$
PS1-10bzo	0.381(0.001)	55555.25(0.47)	0.087	-0.198(0.506)	-0.044(0.041)	22.208(0.056)	41.676(0.150)	0.022(0.003)	9.3870
PS1-10bzp	0.541(0.001)	55547.91(1.38)	0.531	0.034(0.881)	0.013(0.077)	22.956(0.076)	42.274(0.287)	0.020(0.003)	10.7000
PS1-10bzt	0.421(0.001)	55553.35(0.70)	0.163	-0.462(0.664)	0.015(0.058)	22.517(0.063)	41.759(0.212)	0.022(0.004)	9.5270
PS1-10bzu	0.351(0.001)	55552.03(0.74)	0.940	-1.348(0.590)	0.241(0.061)	22.527(0.079)	40.922(0.174)	0.027(0.004)	11.3700
PS1-10bzy	0.200(0.001)	55560.56(0.37)	0.955	-0.232(0.290)	0.035(0.044)	20.745(0.054)	39.954(0.147)	0.009(0.001)	9.3070
PS1-10cad	0.270(0.005)	55555.32(0.43)	0.508	0.532(0.352)	-0.029(0.036)	21.051(0.049)	40.575(0.140)	0.006(0.001)	9.5020
PS1-10cay	0.250(0.005)	55557.62(0.88)	0.995	2.013(0.680)	0.178(0.078)	21.297(0.105)	40.364(0.248)	0.009(0.001)	10.3800
PS1-10cbb	0.220(0.005)	55551.35(0.95)	0.545	-1.554(0.721)	0.156(0.082)	21.270(0.098)	39.909(0.243)	0.008(0.001)	11.3000
PS1-10cbu	0.401(0.001)	55569.62(0.96)	0.648	1.281(1.057)	-0.051(0.061)	22.099(0.090)	41.798(0.227)	0.020(0.003)	11.4100
PS1-11e	0.321(0.001)	55565.32(0.85)	0.002	-1.634(0.554)	0.067(0.064)	22.207(0.076)	41.121(0.189)	0.020(0.003)	10.3000
PS1-11p	0.481(0.001)	55570.58(0.79)	0.483	0.677(0.641)	-0.074(0.053)	22.608(0.058)	42.296(0.183)	0.019(0.003)	8.9970
PS1-11s	0.401(0.001)	55561.99(0.70)	0.765	0.584(0.588)	0.110(0.052)	22.409(0.056)	41.494(0.216)	0.015(0.002)	11.2000
PS1-11t	0.451(0.001)	55570.93(0.49)	0.488	0.539(0.422)	-0.171(0.038)	22.179(0.045)	42.158(0.133)	0.014(0.002)	10.4100
PS1-11w	0.174(0.001)	55568.03(0.30)	0.995	-0.484(0.213)	-0.060(0.031)	20.009(0.038)	39.487(0.103)	0.007(0.001)	8.9020
PS1-11aj	0.107(0.001)	55548.56(1.28)	0.850	-1.576(0.390)	-0.047(0.076)	19.532(0.074)	38.818(0.220)	0.016(0.003)	11.2300
PS1-11at	0.321(0.001)	55571.24(0.51)	0.665	-2.217(0.523)	0.068(0.064)	21.868(0.077)	40.696(0.178)	0.014(0.002)	10.6200
PS1-11bg	0.330(0.001)	55583.99(0.37)	0.428	-0.200(0.398)	-0.068(0.035)	21.725(0.049)	41.270(0.112)	0.019(0.003)	10.7200
PS1-11bh	0.351(0.001)	55580.52(0.34)	0.171	0.175(0.441)	-0.090(0.041)	21.791(0.060)	41.457(0.109)	0.016(0.003)	10.8000
PS1-11bk	0.161(0.001)	55584.81(0.31)	0.061	-0.432(0.245)	0.045(0.046)	20.258(0.045)	39.407(0.141)	0.019(0.003)	12.7200
PS1-11br	0.300(0.005)	55577.12(3.02)	0.994	-0.453(1.387)	-0.240(0.020)	21.226(0.073)	41.286(0.236)	0.009(0.001)	$\cdots$
PS1-11cn	0.249(0.005)	55583.37(0.52)	0.680	0.442(0.470)	-0.163(0.035)	20.669(0.053)	40.608(0.130)	0.022(0.003)	10.2500
PS1-11co	0.230(0.005)	55590.64(1.04)	0.801	-0.321(1.190)	-0.068(0.065)	20.871(0.087)	40.400(0.179)	0.007(0.001)	9.2370
PS1-11fi	0.082(0.001)	55596.22(0.03)	0.664	-1.185(0.272)	0.141(0.042)	18.998(0.060)	37.736(0.148)	0.008(0.001)	$\cdots$
PS1-11iv	0.294(0.001)	55595.98(1.44)	0.889	0.158(0.468)	-0.086(0.041)	21.361(0.048)	41.014(0.154)	0.011(0.002)	9.4320
PS1-11jo	0.331(0.001)	55607.51(0.43)	0.242	0.622(0.445)	-0.071(0.038)	21.674(0.055)	41.344(0.153)	0.014(0.002)	$\cdots$
PS1-11mq	0.210(0.001)	55639.09(0.25)	0.926	1.405(0.234)	-0.101(0.029)	20.225(0.037)	40.100(0.110)	0.007(0.001)	8.4520
PS1-11mz	0.102(0.001)	55642.57(0.14)	0.971	0.685(0.174)	0.023(0.029)	18.951(0.041)	38.328(0.106)	0.013(0.002)	10.1800
PS1-11sk	0.271(0.001)	55678.26(0.26)	0.577	0.026(0.200)	0.115(0.029)	21.582(0.036)	40.574(0.101)	0.016(0.003)	9.2420
PS1-11uo	0.310(0.001)	55686.17(0.32)	0.892	0.608(0.358)	-0.089(0.034)	21.384(0.045)	41.108(0.118)	0.006(0.001)	11.3700
PS1-11uw	0.300(0.001)	55681.60(0.44)	0.617	0.527(0.415)	-0.156(0.032)	21.124(0.049)	41.051(0.131)	0.008(0.001)	10.7500
PS1-11wv	0.133(0.001)	55686.57(0.10)	0.823	0.257(0.140)	-0.124(0.028)	19.109(0.037)	38.898(0.099)	0.012(0.002)	11.3000
PS1-11xc	0.328(0.001)	55691.25(0.60)	0.638	2.481(1.102)	0.161(0.066)	22.130(0.132)	41.316(0.283)	0.008(0.001)	12.8200
PS1-11xw	0.271(0.001)	55700.27(0.33)	0.410	-1.072(0.311)	-0.077(0.033)	21.205(0.041)	40.656(0.117)	0.010(0.002)	11.8500
PS1-11yr	0.531(0.001)	55714.70(0.07)	0.965	1.341(1.597)	-0.128(0.063)	22.950(0.072)	42.903(0.282)	0.010(0.002)	8.5420
PS1-11zd	0.100(0.001)	55701.26(0.75)	0.979	0.596(0.211)	-0.018(0.030)	18.907(0.051)	38.404(0.111)	0.010(0.002)	10.1700
PS1-11zg	0.370(0.001)	55712.81(1.15)	0.368	-0.136(1.828)	-0.068(0.057)	21.913(0.062)	41.466(0.274)	0.007(0.001)	10.6400
PS1-11zu	0.360(0.001)	55711.46(0.72)	0.970	-0.639(0.379)	-0.002(0.046)	22.035(0.048)	41.306(0.157)	0.008(0.001)	10.2400
PS1-11zv	0.350(0.001)	55718.21(0.45)	0.831	0.103(0.356)	-0.060(0.056)	21.727(0.075)	41.289(0.180)	0.008(0.001)	10.4400
PS1-11zw	0.423(0.001)	55711.38(1.70)	0.890	-0.471(0.977)	-0.060(0.118)	22.784(0.090)	42.265(0.419)	0.009(0.001)	11.4700
PS1-11abm	0.321(0.001)	55727.76(0.96)	0.872	-1.739(0.897)	-0.123(0.058)	21.777(0.075)	41.282(0.194)	0.010(0.002)	9.8970
PS1-11aea	0.300(0.001)	55738.26(0.55)	0.846	-0.873(0.249)	-0.036(0.032)	21.788(0.046)	41.138(0.111)	0.007(0.001)	9.4370
PS1-11aij	0.510(0.001)	55774.44(0.51)	0.779	0.861(0.444)	-0.020(0.040)	22.672(0.040)	42.213(0.145)	0.006(0.001)	8.7770
PS1-11ajs	0.229(0.005)	55784.21(0.18)	0.704	-0.128(0.220)	0.113(0.034)	21.340(0.047)	40.317(0.121)	0.039(0.006)	8.8470
PS1-11ala	0.369(0.005)	55795.13(0.30)	0.168	0.285(0.262)	-0.103(0.031)	21.666(0.038)	41.389(0.118)	0.032(0.005)	11.5000
PS1-11alv	0.144(0.001)	55810.78(0.14)	0.990	0.981(0.160)	-0.004(0.030)	19.686(0.047)	39.192(0.101)	0.054(0.009)	10.7300

Note. — Fit parameters of all SNe Ia in the Pan-STARRS1 spectroscopic sample that passed all cuts. The redshift is corrected for coherent flow effects. t_{peak} is the fitted time of B-band maximum m_B. P_{fit} is the SALT2 Fit Probability. x_1, c, m_B, and μ are the parameters as defined in Equation 2. The Milky Way Galaxy Reddening is given in the direction of the SN by Schlegel et al. (1998), and corrected by 6-14% as described in S14. The host galaxy mass given as $\log_{10} M_{host}$.

REFERENCES

Anderson, L., et al. 2012, MNRAS, 427, 3435
Astier, P., et al. 2006, A&A, 447, 31
Bailey, S., et al. 2009, A&A, 500, L17
Barone-Nugent, R. L., et al. 2012, MNRAS, 425, 1007
Berger, E., et al. 2012, ApJ, 755, L29
——. 2013, ApJ, 779, 18
Betoule, M., et al. 2012, ArXiv e-prints, 1212.4864
Beutler, F., et al. 2011, MNRAS, 416, 3017
Blake, C., et al. 2011, MNRAS, 418, 1707
Blondin, S., Mandel, K. S., & Kirshner, R. P. 2011, A&A, 526, A81
Blondin, S., & Tonry, J. L. 2007, ApJ, 666, 1024
Bohlin, R. C. 1996, AJ, 111, 1743
Bohlin, R. C. 2007, in Astronomical Society of the Pacific Conference Series, Vol. 364, The Future of Photometric, Spectrophotometric and Polarimetric Standardization, ed. C. Sterken, 315
Bohlin, R. C., Dickinson, M. E., & Calzetti, D. 2001, AJ, 122, 2118
Bohlin, R. C., & Gilliland, R. L. 2004, AJ, 128, 3053
Botticella, M. T., et al. 2010, ApJ, 717, L52
Campbell, H., et al. 2013, ApJ, 763, 88
Cardelli, J. A., Clayton, G. C., & Mathis, J. S. 1989, ApJ, 345, 245
Chomiuk, L., et al. 2011, ApJ, 743, 114
Chornock, R., et al. 2013, ApJ, 767, 162
Colina, L., & Bohlin, R. C. 1994, AJ, 108, 1931
Conley, A., et al. 2011, ApJS, 192, 1
——. 2008, ApJ, 681, 482
Contreras, C., et al. 2010, AJ, 139, 519
Croft, R. A. C., & Dailey, M. 2011, ArXiv e-prints, 1112.3108
Dressler, A., et al. 2011, PASP, 123, 288
Eisenstein, D. J., et al. 2005, ApJ, 633, 560
Fabricant, D., et al. 2005, PASP, 117, 1411
Fitzpatrick, E. L. 1999, PASP, 111, 63
Flaugher, B. L., et al. 2012, in Society of Photo-Optical Instrumentation Engineers (SPIE) Conference Series, Vol. 8446, Society of Photo-Optical Instrumentation Engineers (SPIE) Conference Series
Folatelli, G., et al. 2010, AJ, 139, 120
Foley, R. J., et al. 2013, ApJ, 767, 57
——. 2009a, AJ, 138, 376
Foley, R. J., Filippenko, A. V., & Jha, S. W. 2008, ApJ, 686, 117
Foley, R. J., & Kasen, D. 2011, ApJ, 729, 55
Foley, R. J., & Kirshner, R. P. 2013, ApJ, 769, L1
Foley, R. J., et al. 2009b, AJ, 137, 3731
——. 2003, PASP, 115, 1220
Foley, R. J., Sanders, N. E., & Kirshner, R. P. 2011, ApJ, 742, 89
Frieman, J. A., et al. 2008, AJ, 135, 338
Ganeshalingam, M., Li, W., & Filippenko, A. V. 2013, MNRAS
Garg, A., et al. 2007, AJ, 133, 403
Gezari, S., et al. 2012, Nature, 485, 217
——. 2010, ApJ, 720, L77
Glazebrook, K., & Bland-Hawthorn, J. 2001, PASP, 113, 197
Goldhaber, G., et al. 2001, ApJ, 558, 359
Guy, J., et al. 2007, A&A, 466, 11
——. 2010, A&A, 523, A7+
Hamuy, M., et al 1996a, AJ, 112, 2408
Hamuy, M., Phillips, M. M., Suntzeff, N. B., Schommer, R. A., Maza, J., & Aviles, R. 1996b, AJ, 112, 2391
Hamuy, M., Phillips, M. M., Suntzeff, N. B., Schommer, R. A., Maza, J., Smith, R. C., Lira, P., & Aviles, R. 1996c, AJ, 112, 2438
Hayden, B. T., Gupta, R. R., Garnavich, P. M., Mannucci, F., Nichol, R. C., & Sako, M. 2012, ArXiv e-prints, 1212.4848
Hicken, M., et al. 2009a, ApJ, 700, 331
——. 2012, ApJS, 200, 12
Hicken, M., Wood-Vasey, W. M., Blondin, S., Challis, P., Jha, S., Kelly, P. L., Rest, A., & Kirshner, R. P. 2009b, ApJ, 700, 1097
Hinshaw, G., et al. 2013, ApJS, 208, 19
Hodapp, K. W., et al. 2004, Astronomische Nachrichten, 325, 636
Holtzman, J. A., et al. 2008, AJ, 136, 2306
Hook, I. M., Jørgensen, I., Allington-Smith, J. R., Davies, R. L., Metcalfe, N., Murowinski, R. G., & Crampton, D. 2004, PASP, 116, 425
Horne, K. 1986, PASP, 98, 609
Inserra, C., et al. 2013, ApJ, 770, 128
Jha, S., et al. 2006, AJ, 131, 527
Jha, S., Riess, A. G., & Kirshner, R. P. 2007, ApJ, 659, 122
Jones, D., et al. 2014, in preparation
Kaiser, N., et al. 2010, in Presented at the Society of Photo-Optical Instrumentation Engineers (SPIE) Conference, Vol. 7733, Society of Photo-Optical Instrumentation Engineers (SPIE) Conference Series
Kattner, S., et al. 2012, PASP, 124, 114

Kelly, P. L., Hicken, M., Burke, D. L., Mandel, K. S., & Kirshner, R. P. 2010, ApJ, 715, 743
Kelson, D. D. 2003, PASP, 115, 688
Kessler, R., et al. 2009a, ApJS, 185, 32
——. 2009b, PASP, 121, 1028
——. 2013, ApJ, 764, 48
Kirshner, R. P. 2010, Foundations of supernova cosmology, ed. P. Ruiz-Lapuente, 151
Krisciunas, K., Phillips, M. M., & Suntzeff, N. B. 2004, ApJ, 602, L81
Lampeitl, H., et al. 2010, ApJ, 722, 566
Lee, C.-H., et al. 2012, AJ, 143, 89
Li, W., et al. 2011, MNRAS, 412, 1441
Lunnan, R., et al. 2013, ApJ, 771, 97
Magnier, E. 2006, in The Advanced Maui Optical and Space Surveillance Technologies Conference
Magnier, E. A., Liu, M., Monet, D. G., & Chambers, K. C. 2008, in IAU Symposium, Vol. 248, IAU Symposium, ed. W. J. Jin, I. Platais, & M. A. C. Perryman, 553–559
Mandel, K. S., Narayan, G., & Kirshner, R. P. 2011, ApJ, 731, 120
Mandel, K. S., Wood-Vasey, W. M., Friedman, A. S., & Kirshner, R. P. 2009, ApJ, 704, 629
Marriner, J., et al. 2011, ApJ, 740, 72
Marshall, J. L., et al. 2008, in Society of Photo-Optical Instrumentation Engineers (SPIE) Conference Series, Vol. 7014, Society of Photo-Optical Instrumentation Engineers (SPIE) Conference Series, 169
McCrum, M., et al. 2013, MNRAS, submitted
Miknaitis, G., et al. 2007, ApJ, 666, 674
Narayan, G., et al. 2011, ApJ, 731, L11
Neill, J. D., Hudson, M. J., & Conley, A. 2007, ApJ, 661, L123
Onaka, P., Tonry, J. L., Isani, S., Lee, A., Uyeshiro, R., Rae, C., Robertson, L., & Ching, G. 2008, in SPIE Conference Series, Vol. 7014, Society of Photo-Optical Instrumentation Engineers (SPIE) Conference Series
Padmanabhan, N., et al. 2008, ApJ, 674, 1217
Padmanabhan, N., Xu, X., Eisenstein, D. J., Scalzo, R., Cuesta, A. J., Mehta, K. T., & Kazin, E. 2012, MNRAS, 427, 2132
Pastorello, A., et al. 2010, ApJ, 724, L16
Percival, W. J., et al. 2010, MNRAS, 401, 2148
Perlmutter, S., et al. 1999, ApJ, 517, 565
Phillips, M. M. 1993, ApJ, 413, L105
Phillips, M. M., Lira, P., Suntzeff, N. B., Schommer, R. A., Hamuy, M., & Maza, J. 1999, AJ, 118, 1766
Planck Collaboration, et al. 2013, ArXiv e-prints, 1303.5076
Rau, A., et al. 2009, PASP, 121, 1334
Rest, A., et al. 2005, ApJ, 634, 1103
Riess, A. G., et al. 1998, AJ, 116, 1009
——. 1999, AJ, 117, 707
——. 2011, ApJ, 730, 119
Riess, A. G., Press, W. H., & Kirshner, R. P. 1996, ApJ, 473, 88
Sako, M., et al. 2011, ApJ, 738, 162
Sanders, N. E., et al. 2013, ApJ, 769, 39
——. 2012, ApJ, 756, 184
Schechter, P. L., Mateo, M., & Saha, A. 1993, PASP, 105, 1342
Schlafly, E. F., & Finkbeiner, D. P. 2011, ApJ, 737, 103
Schlafly, E. F., et al. 2012, ApJ, 756, 158
Schlegel, D. J., Finkbeiner, D. P., & Davis, M. 1998, ApJ, 500, 525
Schmidt, G. D., Weymann, R. J., & Foltz, C. B. 1989, PASP, 101, 713
Scolnic, D. M., et al. 2013, ArXiv e-prints, 1310.3824
Scolnic, D. M., Riess, A. G., Foley, R. J., Rest, A., Rodney, S. A., Brout, D. J., & Jones, D. O. 2014, ApJ, 780, 37
Silverman, J. M., et al. 2012a, MNRAS, 425, 1789
Silverman, J. M., Ganeshalingam, M., Li, W., & Filippenko, A. V. 2012b, MNRAS, 425, 1889
Stetson, P. B. 1987, PASP, 99, 191
Stritzinger, M. D., et al. 2011, AJ, 142, 156
Stubbs, C. W., Doherty, P., Cramer, C., Narayan, G., Brown, Y. J., Lykke, K. R., Woodward, J. T., & Tonry, J. L. 2010, ApJS, 191, 376
Stubbs, C. W., & Tonry, J. L. 2006, ApJ, 646, 1436
Sullivan, M., et al. 2010, MNRAS, 406, 782
——. 2011, ApJ, 737, 102
Taylor, J. 1997, Introduction to Error Analysis, the Study of Uncertainties in Physical Measurements, 2nd Edition (University Science Books)
Tonry, J. L., et al. 2012a, ApJ, 745, 42
——. 2012b, ApJ, 750, 99
Tripp, R. 1998, A&A, 331, 815
Valenti, S., et al. 2012, ApJ, 749, L28
Wade, R. A., & Horne, K. 1988, ApJ, 324, 411
Wang, X., et al. 2009, ApJ, 699, L139
Wood-Vasey, W. M., et al. 2008, ApJ, 689, 377
——. 2007, ApJ, 666, 694

APPENDIX

A. ASTROMETRIC ACCURACY

Accurate astrometry is critical for the discovery and classification of supernovae from a sequence of observations. In addition, forced photometry requires accurate positions as input (see §5.3.2), therefore it is crucial that the astrometry not exhibit any systematic biases. In this appendix, we assses the accuracy of our PS1 astrometry, and quantify it's impact on our overall systematic error budget.

Starting with the reported WCS from the PS1 IPP, we fine-tune the linear terms that define the translation and rotation in 10'x10' cutouts centered on the SN. The astrometric uncertainty σ_a can be described by a systematic floor σ_{a1} and a poissonian term σ_{a2} that scales with the FWHM and SNR:

$$\sigma_a^2 = \sigma_{a1}^2 + \sigma_{a2}^2 \left(\frac{\text{FWHM}}{\text{SNR}} \right)^2 \tag{A1}$$

The value of σ_{a1} is sensitive to the accuracy of the distortion terms, and the number of stars used to determine the WCS solution. If the PSF is undersampled, σ_{a1} is limited by the pixelation and can be as low as 0.05 pixels. For a given telescope/detector system, σ_{a1} and σ_{a2} are global parameters, and our goal is to determine them for the PS1 system. This allows us then to determine the astrometric uncertainty for a given detection depending on its FWHM and SNR.

We compare the detections from a nightly stack with the detections from a deep stack. The uncertainty σ_Δ in the difference of position between the detections in the nightly and the deep stack depends then on the SNR and FWHM of both, the deep and the nightly stack. However, it can safely be assumed that $\text{SNR}_{\text{deep}} \gg \text{SNR}_{\text{nightly}}$, and also that its FWHM is similar or better. Therefore the σ_{a2} term from the deep stack is negligible, and we can write

$$\sigma_\Delta^2 = \sigma_{a,\text{nightly}}^2 + \sigma_{a,\text{deep}}^2 \tag{A2}$$

$$= 2\sigma_{a1}^2 + \sigma_{a2}^2 \left(\frac{\text{FWHM}_{\text{nightly}}}{\text{SNR}_{\text{nightly}}} \right)^2 + \sigma_{a2}^2 \left(\frac{\text{FWHM}_{\text{deep}}}{\text{SNR}_{\text{deep}}} \right)^2 \tag{A3}$$

$$\approx 2\sigma_{a1}^2 + \sigma_{a2}^2 \left(\frac{\text{FWHM}_{\text{nightly}}}{\text{SNR}_{\text{nightly}}} \right)^2 \tag{A4}$$

Figure A1 shows the pixel position difference ΔX (RA on the sky) and ΔY (Dec. on the sky) between the nightly and deep stacks for the stars in our photometric standard star catalog (T12b) of 100 randomly selected images in the g_{P1} band with a plate scale of 0.2 arcsec per pixel. We have done a similar fit for the other filters as well. The mean and standard deviation of the mean are shown with red symbols in appropriately spaced (FWHM/SNR)^2 bins. We fit a straight line to σ_{Delta}^2 versus (FWHM/SNR)^2 for all filters to determine σ_{a1} and σ_{a2} from the slope and intercept of the fit. The fit is very good, and we find

$$\sigma_{a1,X} = 0.135 \pm 0.010 \text{ pixels} = 27 \pm 2 \text{ mas} \tag{A5}$$
$$\sigma_{a1,Y} = 0.105 \pm 0.015 \text{ pixels} = 21 \pm 3 \text{ mas} \tag{A6}$$
$$\sigma_{a2,X} = 1.379 \pm 0.012 \tag{A7}$$
$$\sigma_{a2,Y} = 1.348 \pm 0.011 \tag{A8}$$

We find no differences in a given direction for the different filters, however we note that σ_{a1} does differ at the 2σ-level between the X and Y direction. This discrepancy might be due to the Koppenhoefer effect, in which the positions of objects are biased in the X-direction by an amount which increases for brighter objects. This effect was present in half of the GPC1 chips from the start of the mission until May 2011, at which point modifications to the camera voltages successfully removed the bias. For the affected chips, the maximum displacement (for objects approaching saturation) is in the range of 0.1 - 0.15 arcseconds (up to ~ 0.6 pixels), depending on the device. Objects with fewer than $\sim$25,000 counts are essentially unaffected. As a result, the generally faint objects of interest in this article are not directly affected. The main effect comes from the astrometric calibration, which uses the brighter stars, and likely accounts for the enhanced astrometric scatter in the X direction (Magnier et al., in prep.).

However, we find that this effect has only an insignificant impact on our photometry (<1 mmag). We find small average differences between the positions measured in the nightly and deep stacked images on the order or 10 mas, and we demonstrate that this also has negligible impact on our forced photometry in §5.3.2. Conservatively, we adopt

$$\sigma_{a1} = 0.2 \tag{A9}$$
$$\sigma_{a2} = 1.5 \tag{A10}$$

when we use Equation A1 to determine the astrometric uncertainty in a given detections, e.g. when we cluster detections into obects.
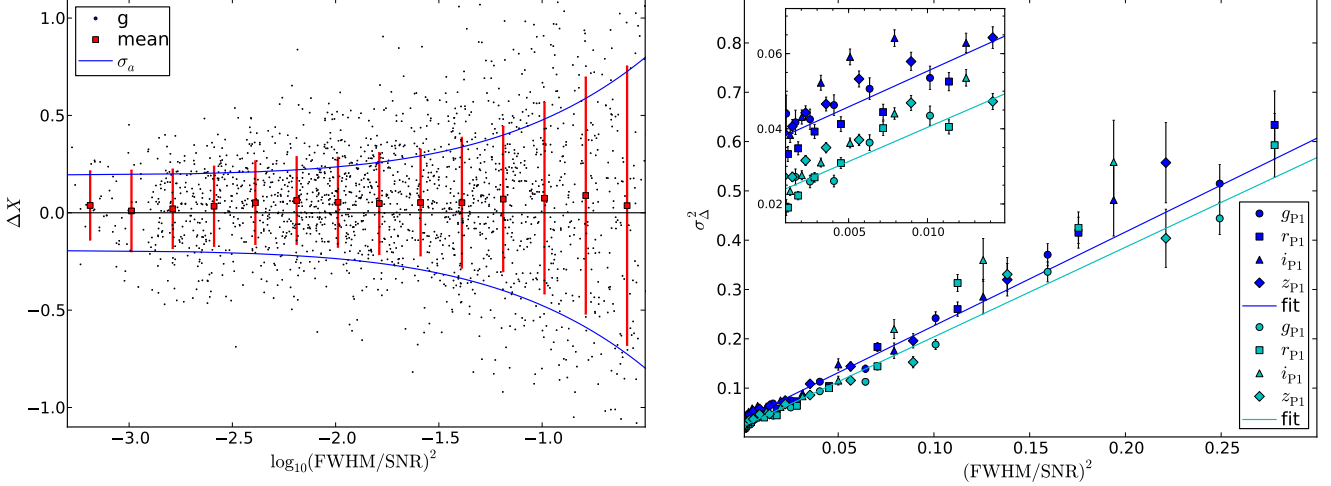
Figure A1. *Left panel:* The position difference ΔX in pixels of nightly and deep stacks for stars from 100 randomly selected g_{P1} band images (black dots) versus $\log_{10}(\mathrm{FWHM/SNR})^2$. The red circles and its error bars indicate the average ΔX in appropriate $(\mathrm{FWHM/SNR})^2$ bins and its standard deviation $\sigma_{\Delta X}$, respectively. The blue line is the fitted $\sigma_{\Delta X}$ from the fit shown in the right panel. *Right panel:* The measured variance $\sigma^2_{\Delta X}$ and $\sigma^2_{\Delta Y}$ in blue and cyan symbols, respectively, for all 4 bands versus $(\mathrm{FWHM/SNR})^2$. The straight line fits are shown with the solid lines. The inset shows that for very small $(\mathrm{FWHM/SNR})^2$, there is a significant difference in X- and Y-direction.

A.1. *SN centroids*

Accurate WCS is necessary, but not sufficient to ensure unbiased forced photometry: difference image artifacts from poor host-galaxy subtraction or other background sources, can introduce additional systematic biases. We found that that a value of $\sigma_{a1} = 0.2$ adequately takes into account these additional biases. For a given SN, we use all detections to re-determine the centroid, calculating the average, weighted by the astrometric errors determined using Equation A1.

B. PSF MODELING

For identifying transients with *photpipe*, we use a customized version of *DoPHOT*, which is quick, robust, and produces adequate photometry. However, Pan-STARRS1 has a PSF with structure that cannot accurately fit with such an analytic model. This may cause systematic biases in the photometry between faint and bright stars of up to 1%. The left of Fig. B1 shows an example of the difference $\Delta g = g_{\mathrm{PS1,DoPHOT}} - g_{\mathrm{PS1,DAOPHOT}}$ between *DoPHOT* and *DAOPHOT* photometry. There is a clear trend from bright to faint magnitudes. *DAOPHOT* fits an empirical correction in addition to the Gaussian model, which significantly better fits the PSF in the image.

The right side of Fig. B1 shows the *DAOPHOT* flux (black symbols) and PSF fit (red line) for $r = 17.5$ and $r = 20.8$ example stars in the upper left and right panel, respectively. In the lower panels, the residual between the flux and the PSF model (black symbols), normalized by the uncertainty, is shown for 10 randomly selected stars in the magnitude bins $17.5 < r < 18.5$ and $20.5 < r < 21.5$. The red circles indicate the average normalized residual Δf_{norm} for appropriate radial bins, and the error bars indicate its standard deviation. The standard deviation is ~ 1 for large radii, but increases to values on the order of up to 1.7 for radii closer to the core. This indicates that some of the PSF structure is still not perfectly fitted for. Most important though, there is no significant bias toward higher or lower fit values for any distance to the core for both the faint and bright stars. We therefore use *DAOPHOT* photometry for all the analysis in *transphot*.

C. EMPIRICAL ADJUSTMENT OF UNCERTAINTIES

The propagated uncertainties are underestimates, as they do not account for the pixel-pixel covariance introduced by warping, sub-sampling, stacking, and convolution of the images. In order to empirically determine by how much the uncertainties are underestimated, we measure the flux f_r and its uncertainty σ_r at random positions in a given difference image in exactly the same way we measure the SN flux. We calculate the weighted mean $\bar{f}_r$ of these flux measurements. In order to guard against reduction and image artifacts, we apply a 3σ cut to the normalized flux distribution $(f_r - \bar{f}_r)/(s_r \sigma_r)$, rather than cutting on the underestimated errors, σ_r, for the following reason: let's assume that all uncertainties are underestimated by the same factor s_r. If we nominally apply a N-sigma cut using these underestimated uncertainties, we effectively apply an N/s_r-cut, e.g. for a nominal 3-sigma cut and $s_r = 1.5$, the real cut-off is at 2-sigma. In order to avoid this, we determine the normalized flux distribution $(f_r - \bar{f}_r)/\sigma_r$, which has a standard deviation of s_r. The true 3-sigma outliers can then be identified and removed by doing an 3-sigma cut on the normalized flux distribution. Note that the standard deviation s_r is equivalent to the square-root of the chi-square distribution

$$s_r = \sqrt{\chi^2_r} = \frac{1}{N-2} \sum_{N} \left(\frac{f_r - \bar{f}_r}{\sigma_r} \right)^2 \tag{C1}$$
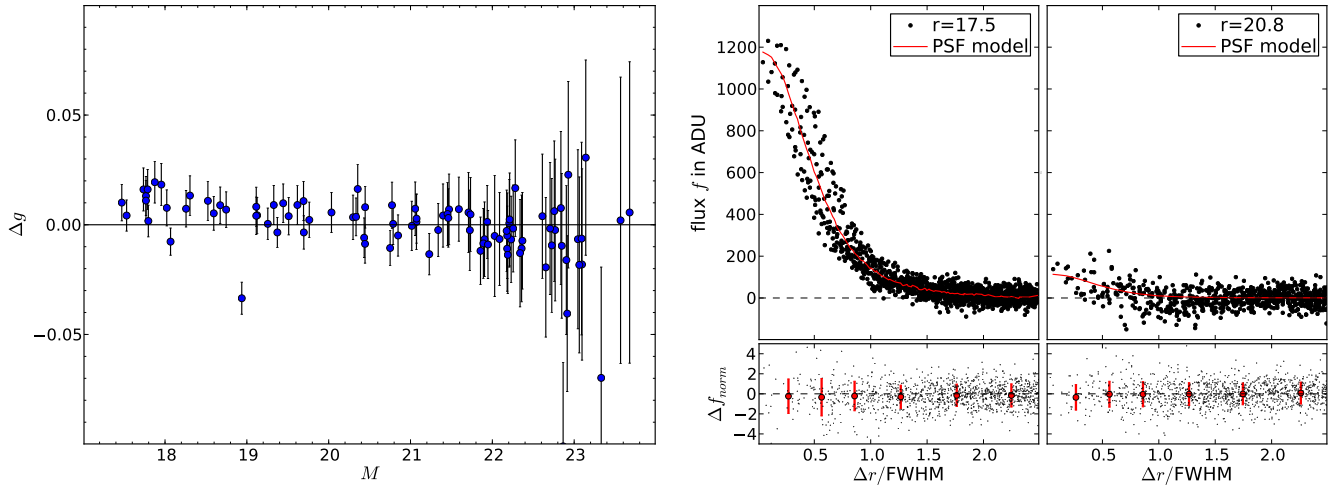
Figure B1. *Left:* Difference in g_{P1} band magnitudes between *DoPHOT* and *DAOPHOT* photometry. *Right:* *DAOPHOT* PSF for an r=17.5 and r=20.8 magnitude star. The red line shows the PSF model used, and the black dots the observed flux. The x-axis is the distance to the centroid position, normalized by the FWHM. The lower panels show the difference between the measured flux and the model normalized by the uncertainty Δf_{norm} for a subset of values randomly chosen from 10 stars. The red circles indicate the average Δf_{norm} for appropriate radial bins, and the error bars indicate the standard deviation.

We multiply all uncertainties by the factor s_r in order to empirically correct the uncertainties. We find that it is imperative to employ this robust way of determining s_r for the method to work correctly. The fact that the reduced chi-square of the baseline flux of the SN light curves peaks at 1.0 validates our method (see §5.3.4).

In addition, for a given difference image, $\bar{f}_r$ is an estimate of the bias in the flux measurements. The values of $\bar{f}_r$ are in general very small, much smaller than the typical uncertainties. Nevertheless, we adjust all fluxes by this value.

D. CORRECTION OF SYSTEMATIC MAGNITUDE BIASES DUE TO CENTROIDING ERRORS

We determine the position of a given SN as the weighted mean of all its detections. This SN centroid (RA_0, DEC_0) has a non-negligable astrometric uncertainty $\sigma_{SN,cent}$, which introduces a bias in our recovered photometry and must be corrected. The recovered position of a detection can be different from the SN centroid for the following reasons:

1. Poisson noise, in particular positive noise peaks, in the background sky.

2. Poisson noise in the SN flux

3. Difference image artifacts

4. The centroid accuracy of (RA_0, DEC_0).

5. Accuracy of the WCS for a given image.

The first three items in the list above introduce a Malmquist bias for regular photometry since the freedom in position will bias the fitted PSF to be centered toward the positive noise peaks. This effect is stronger for detections with low SNR. However, using forced photometry eliminates this bias (see also § 5.3.2 and Figure 5). What is not corrected for is if the position used for forced photometry of the SN is offset from the true position of the SN, either because the uncertainty in SN centroid or due to inaccuracies of the WCS for the given image. In this section, our goal is to characterize how the photometric bias depends on the astrometric offset, so that we can estimate the expectation value of the photometric bias for a given centroid accuracy and correct for it.

For our analysis, we use detections of PS1-10axx, a SN Ia at $z = 0.027$ with a good selection of detections with both high and low SNR. As described in § 5.2, the position (RA_0, DEC_0) was determined by calculating the 3σ clipped weighted mean of all detections. With forced photometry, (RA_0, DEC_0) is translated into (X_0, Y_0) for a given image, and the center of the PSF is forced to be at (X_0, Y_0). We investigate how the photometry depends on the centroid position by measuring the photometry at position $(X, Y) = (X + \Delta X, Y + \Delta Y)$. We define the change in photometry as

$$\Delta m(\Delta X, \Delta Y) = m(X_0 + \Delta X, Y_0 + \Delta Y) - m(X_0, Y_0). \tag{D1}$$

For simplicity, we concentrate on one dimension (ΔX), and later on apply it to two dimensions. In the right panel of Figure D1, we show $\Delta m(\Delta X)$ for detections of PS1-10axx high SNR. Without noise, $\Delta m(\Delta X)$ would be a parabola with a minimum at $\Delta X = 0$, but due to a combination of the reasons listed above, the parabola is shifted. We fit these parabolas with

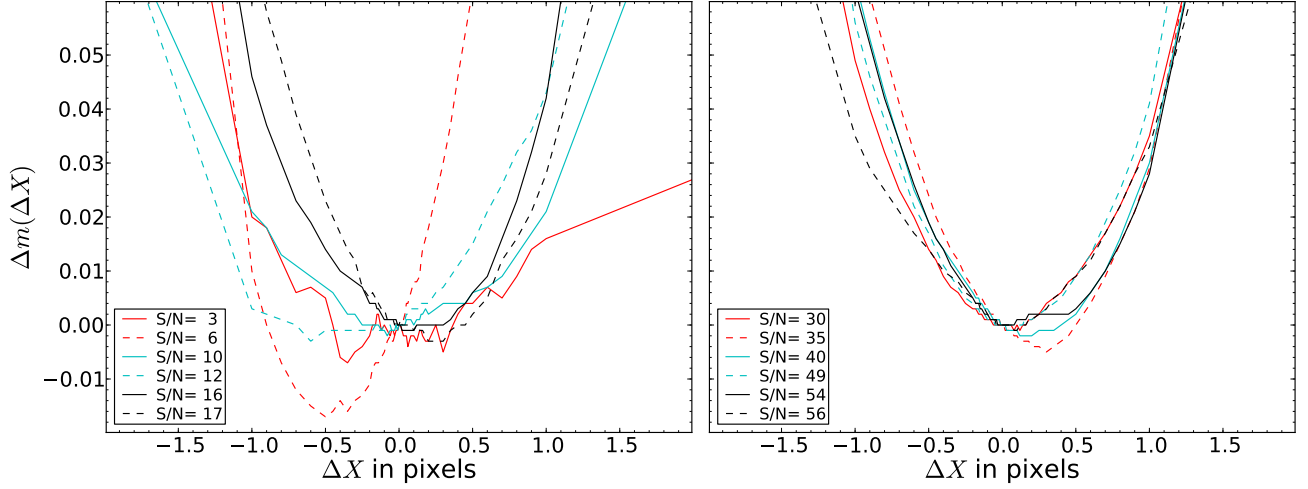$$\Delta m(\Delta X) = h(\Delta X - \Delta X_{min})^2 + \Delta m_{min} \tag{D2}$$

Figure D1. *Left:* The difference in forced photometry $\Delta m(\Delta X, \Delta Y) = m(X_0 + \Delta X, Y_0 + \Delta Y) - m(X_0, Y_0)$ between (X_0, Y_0) and $X_0 + \Delta X, Y_0 + \Delta Y$ for low SNR detections of PS1-10axx. *Right:* Same as the left panel, but for high SNR detections of PS1-10axx.
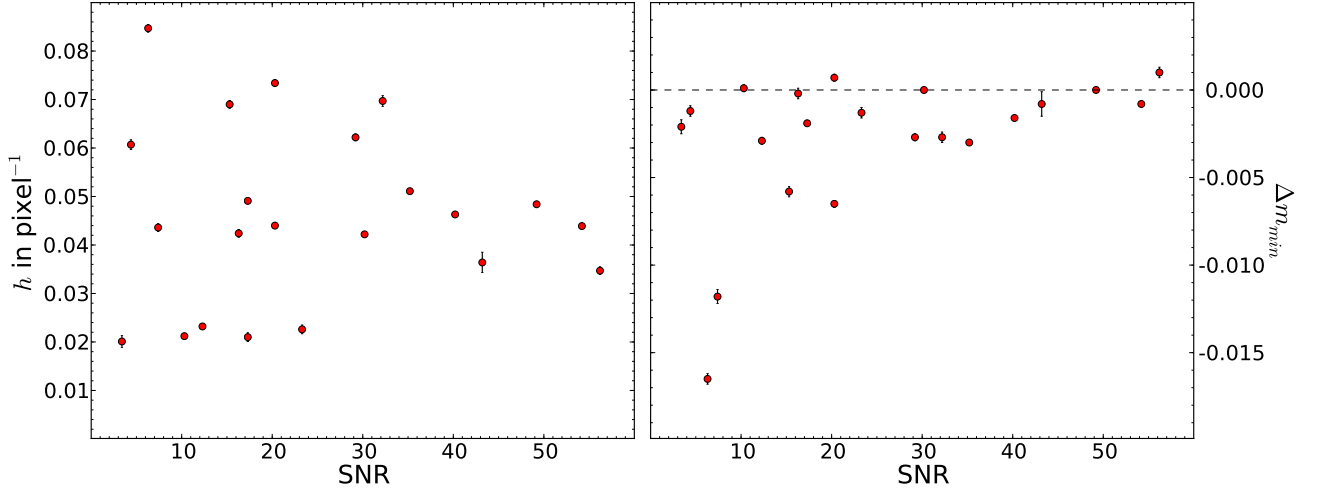

Figure D2. *Left:* Parameter h from Equation D2 derived by fitting $\Delta m(\Delta X)$ with a parabola. *Right:* Parameter $\Delta m_{\min}$ from Equation D2.

where $\Delta X_{\min}, \Delta m_{\min}$ are the coordinates of the mininum of the parabola for a given detection, and h defines the width of the parabola.

If we assume that this shift in the position of the minimum is due to the error in the SN centroid, then the SN centroid used was off by $\Delta X_{\min}$ from the true centroid, and the photometry was biased by $\Delta m_{\min}$. Now we can turn around this argument: If we know h, the width of the parabola, and the centroid accuracy of a given SN centroid $\sigma_{\mathrm{SN,cent},X}$, we can calculate the expectation value of the photometric bias $\Delta m_{\mathrm{SN,cent},X}$ as

$$\Delta m_{\mathrm{SN,cent},X} = \int h t^2 \mathrm{PDF}(\sigma_{\mathrm{SN,cent},X}, t)\, \mathrm{d}t \tag{D3}$$

where $\mathrm{PDF}(\sigma, t)$ is the probability density function with sigma σ, and assuming that h is constant and independent of SNR.

The assumption that the width of the parabola is constant and independent of SNR appears to valid to the first order. For high SNR, the width of the parabola seems to be constant (see right panel of Figure D1). For low SNR detections, however, the width of the parabola show a much larger variation (see left panel of Figure D1). Figure D2 shows the fitted h and $\Delta m_{\min}$ for all detections of PS1-10axx in the left and right panel, respectively. For low SNR, the spread in h significantly increases because of poisson fluctuations in the flux and/or difference image artifacts. We therefore use the h derived only from the SNR>35 detections:

$$h = 0.043 \pm 0.003 \ \mathrm{pixel}^{-2} \tag{D4}$$

with a standard deviation of 0.007. Any effect of the spread in h on $\Delta m_{\mathrm{SN,cent},X}$ cancels out to first order, as long the mean h is independent of SNR.
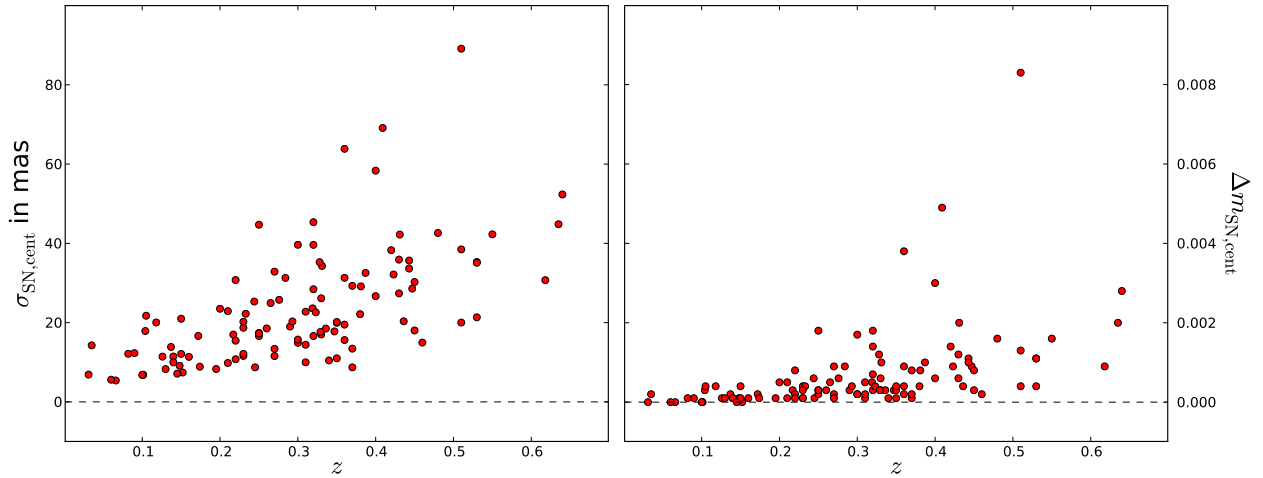
Figure D3. *Left:* The astrometric uncertainty in the SN centroid position determined by averaging the position of all detections versus redshift. The uncertainty in the SN centroid increases with increasing redshift. *Right:* The expectation value of the photometric bias due to the centroid uncertainty calculated with Equation D5.

For a given SN, we estimate the uncertainty in the SN centroid $\sigma_{\mathrm{SN,cent},X}$ and $\sigma_{\mathrm{SN,cent},Y}$ when we calculate the SN position (RA_0, DEC_0) as the weighted mean of all the SN detections. Using the fitted h and Equation D3 we can now calculate the expectaction value of the systematic bias $\Delta m_{\mathrm{SN,cent}}$ in our SN photometry:

$$\Delta m_{\mathrm{SN,cent}} = \Delta m_{\mathrm{SN,cent},X} + \Delta m_{\mathrm{SN,cent},Y} \tag{D5}$$

The left panel of Figure D3 shows $\sigma_{\mathrm{SN,cent}} = \sqrt{\sigma_{\mathrm{SN,cent},X}^2 + \sigma_{\mathrm{SN,cent},X}^2}$ for all SNe versus the redshift, and the right panel shows $\Delta m_{\mathrm{SN,cent}}$. The photometric bias has a systematic trend with redshift on the order of 2mmag, and these corrections are added to our final photometry.